Mesoscopic structural changes and visible light emission during nanosecond infrared laser-induced phase separation of binary liquid mixtures

Doctoral Thesis

Mesoscopic structural changes and visible light emission during nanosecond infrared laser-induced phase separation of binary liquid mixtures

（二液混合系のナノ秒赤外レーザー誘起相分離における メゾスコピック構造変化と可視発光現象）

Shuichi Toyouchi

2014

Table of contents

3-7 Conclusion
References
Chapter 4 Mesoscopic structural changes in laser-induced phase separation - - - - - - - - 43
4-1 Preface
4-2 Comparison of measurement methods
4-3 Nanosecond structure illumination microscopy
4-3-1 Evaluation of nanosecond structured illumination microscopy
4-3-2 Demonstration of observation for laser-induced phase separation
4-3-3 Selection of fluorescent dye
4-4 Early stage of laser-induced phase separation
4-5 A new view of the early stage of spinodal decomposition
4-6 Conclusion
References
Chapter 5 Bubble formation and light emission during laser-induced T-jump - - - - - - - - 63
5-1 Preface
5-2 Observation of bubbles and light emission
5-2-1 Bubbles
5-2-2 Emission spots
5-2-3 Temperature dependent
5-2-4 Composition dependent
5-2-5 Correlation between bubble formation and light emission
5-3 Effects of dissolved gas and addition of salt
5-3-1 Dissolved gas
5-3-2 Addition of salts
5-4 Time-resolved emission spectrum measurements
5-4-1 Emission spectrum
5-4-2 Time decay analysis
5-5 Mechanism of bubble formation and light emission during laser-induced T jump
5-6 Conclusion
References
Chapter 6 Conclusion - - - - - - - -

Chapter 1 Introduction

In our life, there are so many soft materials such as liquid crystals, glass, plastic, expanded polystyrene, paint, milk, forth on beer, and gelatin etc. They are called “soft matter”. The soft matter is essential for enriching our life. Our bodies also consist of soft matter. For example, genetic information is stored in polymers of double helix called DNA, and proteins that play very important functions in our bodies are also categorized to polymers. Furthermore, a biological membrane consists of bilayer of amphiphilic molecules such as phospholipids and glycolipids. These polymers and amphiphilic molecules can be regarded as soft matter. Therefore, knowledge of soft matter leads to fundamental understanding of life.

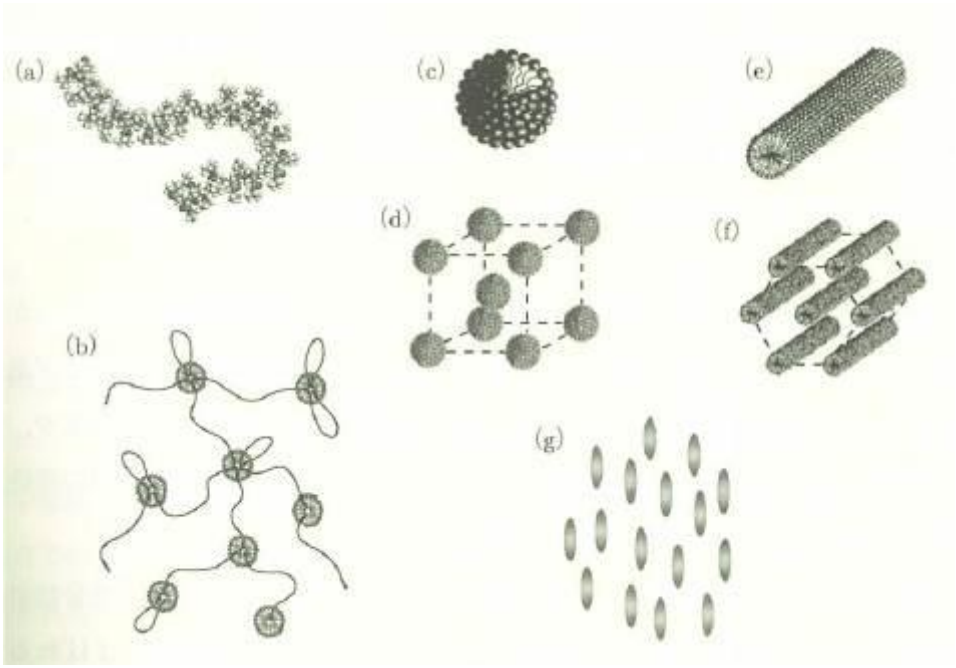

Fig.1-1 Typical systems of soft matter. (a) Water-soluble polymer (polyisopropyl acrylamide). (b) Cross-linked surfactant micelles with both-ends association polymer (telechelic polymer). (c,d) Spherical micelle and the ordering. (e,f) Rod micelle and the ordering. (g) Nematic liquid crystal. Ref.1

Viscoelasticity is a considerable property of soft matter. Viscous materials, like honey, resist shear flow and strain linearly with time when a stress is applied. Elastic materials strain when stretched and quickly return to their original state once the stress is removed. Viscoelastic materials have elements of both of these properties and, as such, exhibit time-dependent strain. This property results from hierarchical structures from atomic- and molecular-level to macroscopic scale. Generally, when a material is placed under an external force, a small structure relaxes to stable state with a short time, whereas a large structure takes a long time to relax. The difference in time scale corresponding to the scale of structure results in the viscoelasticity of the soft matter.

Moreover, the soft matter shows also an interesting phenomenon at a mesoscopic scale. An interaction between each component in soft matter is weaker than in metal or a semiconductor, and atoms and molecules compose an ordered structure with nanometer scale about 1 ~ 1000 nm under a mild constraint condition. Thus, to understand properties of soft matter, it is necessary to obtain knowledge of the hierarchical structure and their response for external force at each level.

As one of the simplest example of soft matter having a hierarchical structure, phase diagram of water/2-butoxyethanol (2BE) mixture is shown in Fig.1-2. 2BE is thought to be the shortest nonionic surfactant in a series of poly(ethylene glycol) monoalkyl ether ($CH_3(CH_2)_{i-1}(OCH_2CH_2)_jOH$, C_iE_j), and can be described as C_4E_1. The molecular structure of 2BE is shown in Fig.1-2 (a). 2BE has a hydrophobic alkyl chain part and a hydrophilic ethylene part. The mixture has its lower critical solution temperature (LCST) at 49.3°C and the critical composition is 0.052 with respect to the 2BE molar fraction χ_{2BE}.[2] The mixture split into two phases from one phase with a temperature rise. This macroscopic phase transition is called phase separation. The phenomenon is an interesting subject from viewpoints of both chemistry and physics, because it involves macroscopic cooperative process which appears as a comprehensive result of microscopic interactions between components.[3,4]

Even in one phase region, it has been reported that water/2BE mixtures show microscopic-mesoscopic-phase transition. In the mixture, 2BE molecules form micellar like aggregates due to the amphiphilic property. D'Angelo *et al.* have reported that critical micellar concentration (CMC) at 25°C is 0.0175 with respect to χ_{2BE} and the temperature dependence on CMC are shown in Fig.1-2 (b) as a dotted line.[5] A study of depolarized light scattering by Micali *et al.* suggested percolation structure which consist of the micellar aggregates.[6] Koga *et al.* have studied on water/2BE mixtures by using a small-angle X-ray scattering technique and thermodynamic analysis.[7] One conclusion from their work is that one phase region in phase diagram can be separated into three regions, I ($\chi_{2BE} < 0.0175$), II ($0.0175 < \chi_{2BE} < 0.46$), and III ($\chi_{2BE} > 0.46$) at 25°C, in which the mixing scheme is qualitatively different from those of others (Fig.1-2 (c)). In the region I, the mixing scheme is consistent with the commonly adopted explanation of iceberg formation or the enhancement of the hydrogen bond network. In the region II, water/2BE mixtures may consist of two kinds of clusters, rich in each component, preparing for phase separation above the LCST. The percolation, which is present in pure H_2O, no longer exists in this region. As the temperature and the composition approach the LCST and the critical composition, these clusters grow in size and become macroscopic in the vicinity of the LCST. In the region III, the clusters of purely 2BE molecules exist and H_2O molecules are adsorbed on the surfaces of such clusters. According to these reports, it has revealed that water/2BE mixture shows very complex hierarchical structures, and there are various phases at microscopic- and mesoscopic-level even in macroscopic one phase region.

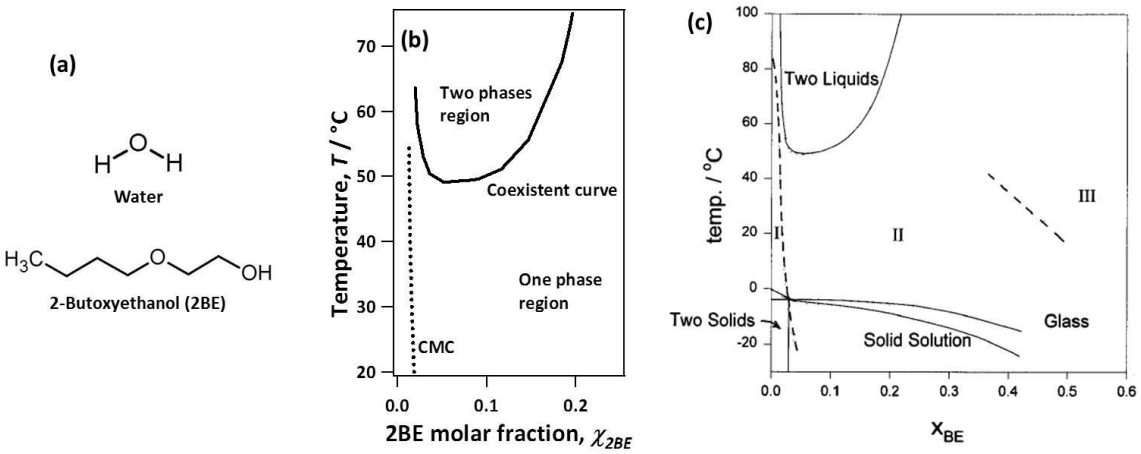

Fig.1-2 (a) Molecular structures of water and 2BE. (b) Phase diagram of water/2BE mixture measured in this study. Dotted line represents CMC. Ref.5 (c) Phase diagram of water/2BE mixture and mixing scheme diagram. Ref.7

Recently, new strategies of chemical reaction control by using the unique solvent environment of binary liquid mixtures at their LCSTs, like water/2BE mixture, have been proposed. There are several recent reports of the critical slowing down of chemical reactions, for example, saponification of ethyl acetate,[8] alkaline fading of crystal violet[9] and phenolphthalein[10] in the vicinity of the LCST. In these methods of chemical reaction control, it is thought that the complex solution structures of sub LCST solutions directly influence the reactions. Since a chemical reaction in a solution generally proceeds by the translational diffusion of solute molecules, it is important to investigate the solute diffusion in order to understand and control the chemical reaction. In the case of chemical reactions in water/2BE mixtures, it is expected that the solute diffusion is affected by the hierarchical structures, especially mesoscopic structure like micellar aggregates. The strength of the influence can depend on the properties of solutes such as solubility and their tendency to aggregate. Thus, there is rising interest in studying the diffusion of solutes in complex mixtures, and several studies have examined anomalous diffusion and phase transition in polymers and polymer containing solutions using pulse-field gradient NMR, dynamic light scattering, and other methods.[11-13]

However, it is still not well understood how such hierarchical structures in water/2BE mixtures affect the diffusion of different solutes, i.e. whether the transient heterogeneities are a bulk feature that applies to any kind of solute or if different solutes can experience different environments. Therefore, in this study, fluorescence correlation spectroscopy (FCS) was employed to investigate solute diffusion at various molar fractions of 2BE in water/2BE mixtures and found marked differences in the diffusion of two different fluorescent dyes. FCS is one of many different methods for high-resolution spatial and temporal analysis of fluorescent dyes at extremely low

concentrations.[14,15] In contrast to other fluorescence techniques, a parameter of primary interest is not the emission intensity itself, but the spontaneous fluctuations of emission intensity caused by minute deviations of the target system from thermal equilibrium, which may arise from diffusion, intersystem crossing, conformational changes or chemical reactions of the fluorescent dye in the media. In general, all physical parameters that lead to fluctuations in emission intensity can be accessed by FCS. It is straightforward to determine local concentrations, intrinsic diffusion coefficients or characteristic rate constants of inter- and intra-molecular reactions of fluorescent dyes at nano-molar concentrations.

The amphiphilic dye ATTO 532 NHS ester (ATTO532), and the more hydrophobic dye N,N'-Bis(2,6-dimethylphenyl)perylene-3,4,9,10-tetracarboxylic diimide (BPDI) were used as solutes, and were investigated the influence of the solvent properties on their diffusion. All measurements were carried out at room temperature far below the LCST (Fig.1-3). As a reference, FCS experiments were also carried out with the hydrophobic dye in water/methanol (MeOH) mixtures, whereby signs of phase separation or complex solution structures were not observed. It is reported here that the diffusion behavior depends on both the properties of the solutes and the solvents, and that the diffusion of the hydrophobic dye in water/2BE unusually slows down even far below the LCST when approaching the critical composition. These results are described in Chapter 4 and discussed from a viewpoint of the interactions between the solute molecules and the transiently formed solution structures.

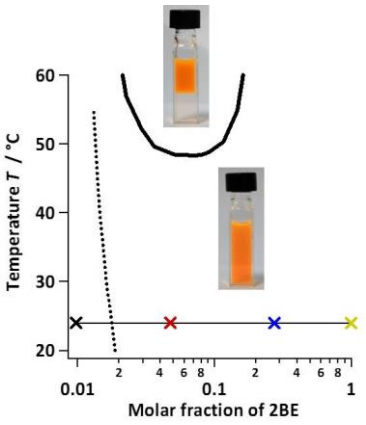

Fig.1-3 (a) Phase diagram of water/2BE mixture. Crosses, and thick solid and dot lines express FCS measurement points, coexistent curve, and critical micelle concentrations at various temperatures (reference 22). Upper and lower pictures are the water/2BE mixture with BPDI 10^{-5} M after and before phase separation, respectively.

Furthermore, the dynamics of phase separation is a quite interesting subject. The dynamics has been studied as one example of phase transition containing ordering process. Two kind of phase separation are known so far; nuclear generation process and spinodal decomposition (SD)

process, like other phase transition phenomena. When a binary mixture is quenched into the metastable region on its phase diagram, the mixture separates into two phases through the nuclear generation. On the other hand, when the mixture is quenched into the unstable region, the mixture separates through SD. The SD process especially has attracted much attention of many researchers. However, in the previous studies on phase separation dynamics, temporal resolution of experimental methods was not so high that the studies focused on only slow response with macroscopic changes.[16-21] For investigation of molecular-level and mesoscopic-level changes, a rapid external force to induce phase separation is necessary with nanoseconds or faster than nanosecond time resolution. In addition, almost all of samples were polymer solutions which show slow response for external force, and very few studies on simpler surfactant solution have been reported. The reason may be that it was difficult to apply rapid external force with nanosecond time-resolution by using a conventional water bath system. Changes of a small structure of soft matter have never been accessible by using a technique with low temporal resolution. Therefore, the behavior of each hierarchical structure and their relevance during phase separation of soft matter has not been well discussed so far. By considering that interactions between components at atomic- and molecular-level result in mesoscopic structures, and the mesoscopic structures induce macroscopic self-organization in soft matter,[22] it is obviously important to understand the behavior of hierarchical structures. Especially how a mesoscopic structure which is a considerable property behaves during phase separation is an interesting research subject.

Phase separation in aqueous solutions can be induced with a near infrared (IR) pulsed laser temperature-jump (T-jump) method.[23-26] The T-jump allows the observation of phase separation dynamics with a deep quench (several K) due to the direct vibrational excitation of water molecules, resulting in a homogeneous temperature rise of the mixture within several nanoseconds.[27,28] The dynamics of laser-induced phase separation (LIPS) involves the relaxation from an unstable non-equilibrium state very far from the equilibrated state. The relaxation occurs on different time scales through processes such as heat diffusion, hydrogen bond dissociation, mass diffusion, the formation of new phases, and macroscopic phase growth. Previous studies have revealed that molecular-level and macroscopic dynamics of LIPS by applying time-resolved (TR) Raman scattering and shadowgraph-imaging to LIPS.[23-25] TR Raman spectra showed that molecular level changes terminated within 1 μs after the T-jump. TR shadowgraph-imaging showed that the domain size $L(t)$ increased during phase separation following the power law $L(t) \sim t^{\alpha}$. However, phase domain growth was observed only after the phase size became larger than several hundreds of nanometers, because of the spatial resolution of a microscope system used. Therefore, there is still a big temporal and spatial gap between early molecular level events and later macroscopic changes, and it is still not possible to discuss the overall hierarchical structure. Mesoscopic structures during phase separation are also interesting as chemical reaction fields. In recent years, some attempts

have been made to apply LIPS in binary liquid mixtures with unique chemical reaction fields for nanomaterial systhesis.[29,30] A UV laser pulse irradiation with a certain delay time after a near IR pulse was employed to synthesize gold nanoparticles in the chemical reaction field. Gold square plates were obtained, and the size and shape distribution of the nanoparticle changed drastically when the delay time was varied from 1 to 10 μs. For understanding of mechanism of chemical reaction control, it is needed to obtain knowledge about changes at the time region 1 to 10 μs. Observation of mesoscopic structural changes in LIPS is important from not only fundamental research side but also application side. In this study, to overcome the diffraction limit and observe mesoscopic structural changes, we attempted to extend the temporal resolutions of measurement methods having super-resolution ability to the nanosecond time scale.

The most important parameter in a discussion of optical microscope performance is a spatial resolution of a microscope. Although several definitions for the spatial resolution are used and discussed, closest distance which two points can be identified is the most general definition. There is a limit of the resolution, and the resolution is approximately half of light wavelength. Many organelles are interacting with each other, and intracellular processes like change of substances occur in the order of sub-resolution, which is described above. Therefore, it was a desire of many researchers in biological fields that a microscope technique which breaks the limit of resolution will be developed. Not only in biological field, also in the field of material science, there is a great demand for the microscope technique due to the convenience of an optical microscope. Along this line, a variety of microscopic techniques such as two-photon excitation fluorescence microscopy or confocal microscopy have been developed, but have not been able to break up the limit of resolution. By Hell *et al.* from German in 2000, stimulated emission depletion microscopy (STED) have been developed with super-resolution beyond the spatial resolution of conventional microscopes[31], and the world of microscopy studies have reached a major turning point. Elsewhere, by Betzig *et al.* in 2006 have developed photo-activated localized microscopy (PALM),[31] and Rust *et al.* in also 2006 have developed stochastic optical reconstruction microscopy (STORM)[32]. Further improvement is added to these techniques, it has a resolution of more than 20 nm at present. It may be able to observe mesoscopic structure of soft matter by using these techniques. However, there is a big drawback to these techniques. That is, it takes very long time to get a super-resolution image. Thus an attempt has to be made to expand the temporal resolution to be nanosecond to obtain super-resolution information of mesoscopic structures in a liquid.

In this study, nanosecond structured illumination microscopy (SIM) was developed to obtain knowledge with high spatial and temporal resolution. SIM is one of super-resolution microscopy (Fig.1-3).[34-36] In the method, spatially structured illumination which is a sum of finite number of components is used as excitation illumination for fluorescent dye. Each component is a single

harmonic wave. Spatial frequency of a sample interferes with frequency of the illumination pattern and is shifted toward high and low frequency. Therefore, a new spatial pattern appears (Fig.1-4). This effect of interference is called Moire effect. Temporal resolution of SIM also is not high enough, because several images (generally 9 ~ 15 images) are necessary to obtain a single super-resolution image. However, it is expected to be possible to detect super-high spatial frequency in a sample with nanosecond temporal resolution when the sample itself has a periodic structure like phase separating mixture. This approach itself is important, and expected as a starting point to further improvements for the purpose of visualization of the solution local structure in the future.

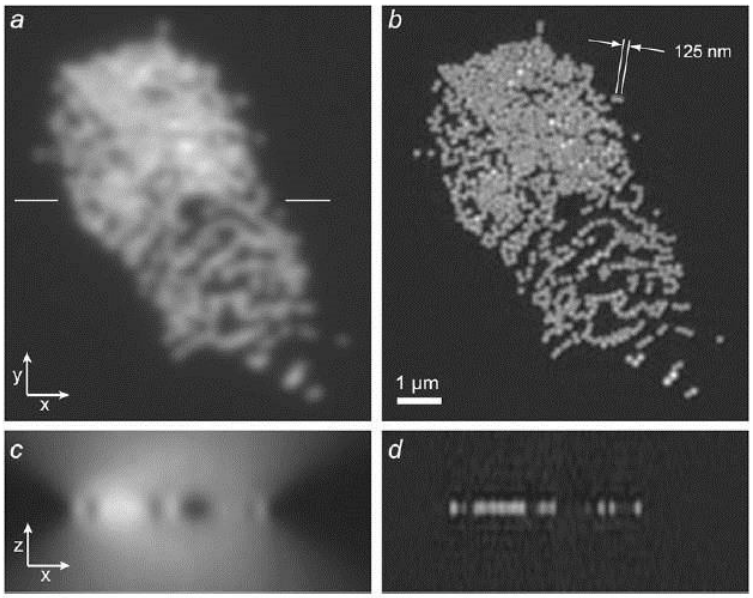

Fig.1-3 A cluster of red-fluorescent microspheres of nominal diameter 0.12 mm, imaged with (a,c) conventional microscopy, and (b,d) structured illumination microscopy. (a,b) Single in-focus x,y sections illustrating the improvement of lateral resolution. (c,d) Single x,z sections, at the y position indicated by horizontal lines in panel a, illustrating removal of out-of-focus blur above and below the plane of focus. Ref.34

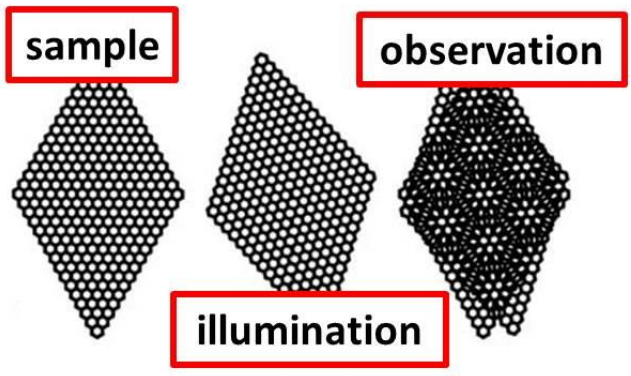

Fig.1-4 Moire effect.

Light scattering technique was also employed for investigation of the dynamics of LIPS. This technique has been frequently employed in studies on phase separation of polymer solutions and micro-emulsion system,[16-18] allows us experiment without an optical microscope's diffraction limit.

Additionally, bubble formation and sonoluminescence[37]-like light emission spots were found at the early stage of LIPS. These phenomena are unique in laser-T-jump experiments. Although there were some reports of observation of bubbles during LIPS,[38,39] to our knowledge, this is the first observation of the light emission. This phenomenon is interesting because vibrational energy can be converted to the generation of electronic excited molecules. The mechanisms of bubble formation and light emission were still unclear. The purposes of this study are characterization and providing knowledge of the bubble formation and the light emission to reveal these mechanisms.

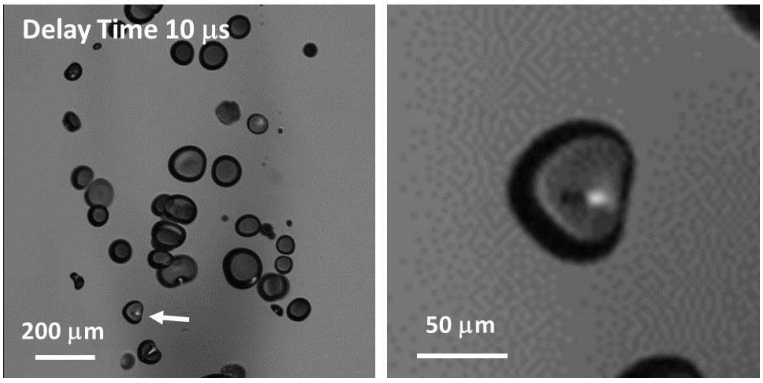

Fig.1-4 Left : A shadowgraph image of bubble formation at delay time 10 μs in water/2BE/KCl. A bright spot was observed inside a bubble pointed with an arrow. Right : Expanded image of the pointed bubble.

This thesis consists of 7 chapters. Contents of each chapter are described below.

In this chapter, backgrounds and purposes of this study are described. In the next chapter, theoretical backgrounds on phase separation and other research topics that are discussed in this study are described. In Chapter 3, details of samples are described. In this study, water/2BE mixture was mainly used as sample solution. Many studies on the mixture have been reported from viewpoint of static solution properties and dynamics of phase separation as mention above. Laser-induced T-jump method was used to accomplish rapid and deep quench into unstable region on phase diagram with nanosecond time-resolution. For investigation on dynamics of LIPS, and accompanying bubble formation and light emission, some imaging and spectroscopic techniques were used. Details of these methods are also described in Chapter 3.

In Chapter 4, experimental results of FCS measurements are shown. An influence of a complex solution structure in water/2BE mixture on solute diffusion is discussed. Next, in the chapter 5,

experimental results in investigation on dynamics of LIPS are shown. Based on our observation and the previous time-resolved Raman scattering studies, a new view of early stage of SD in water/2BE mixture is proposed from a viewpoint of mesoscopic structural changes. In the chapter 6, experimental results of bubble formation and light emission during laser-induced T-jump are shown. According to our observation, one possible mechanism is proposed for these phenomena.

In the chapter 7, results of this study and new viewpoints for laser-induced phase separation are summarized. Furthermore, an outlook for future study on phase separation dynamics is described.

References

[1] F. Tanaka, *Thermodynamics for soft matter science* (in Japanese), Shokabo, **2009**.

[2] F. Mallamace, N. Micali, C. Vasi, G. D'Arrigo, *Il Nuovo, Cimento*, **1992**, *14*, 333.

[3] Y. L. Tang and Y. Q. Ma, *Phys. Rev. E*, **2002**, *65*, 061501.

[4] P. M. Chaikin, T. C. Lubensky, T. Matsubara, *Condensed-matter physics of modern* (in Japanese), Yoshiokashoten, **2000.**

[5] M. D'Angelo, G. Onori, A. Santucci, *Chem. Phys. Lett.*, **1994**, *220*, 59.

[6] N. Micali, S. Trusso, C. Vasi, F. Mallamace, D. Lombardo, G. Onori, A. Santucci, *Phys. Rev. E*, **1995**, *51*, 2349.

[7] Y. Koga, *J. Phys. Chem.*, **1996**, *100*, 5172.

[8] Y. W. Kim, J. K. Baird, *Int. J. Thermophys.*, **2004**, *25*, 1025.

[9] Z. Du, S. Mao, Z. Chen, W. Shen, *J. Phys. Chem. A*, **2013**, *117*, 283.

[10] Z. Du, H. Yin, Z. Hao, P. Zheng, W. Shen, *J. Chem. Phys.*, **2013**, *139*, 224501.

[11] A. Masuda, K. Ushida, H. Koshino, K. Yamashita, T. Kluge, *J. Am. Chem. Soc.*, **2001**, *123*, 11468.

[12] S. Mele, B. W. Ninham, M. Monduzzi, *J. Phys. Chem. B*, **2004**, *108*, 17751.

[13] M. Stepanek, P. Matejicek, J. Humpolickova, K. Prochazka, *Langmuir*, **2005**, *21*, 10783.

[14] D. Magde, E. Elson, W.W. Webb, *Phys. Rev. Lett.*, **1972**, *29*, 705.

[15] C. Gell, D. Brockwell, A. Smith, *Handbook of single molecule fluorescence spectroscopy*, Oxford university press, **2006**.

[16] N. Kuwahara, K. Kubota, M. Sakazume, H. Eda, K. Takiwaki, Phys. Rev. A, 1992, 45, R8324.

[17] K. Kubota, N, Kuwahara, *Phys. Rev. Lett.*, **1992**, *68*, 197.

[18] F. Mallamace, N. Micali, S. Trusso, J. Phys.: Condens. Matter, 1996, 8, A81.

[19] T. Ohta, O. Urakawa, Q. Tran-Cong, *Macromolecules*, **1998**, *31*, 6845.

[20] K. Murata, T. Murata, H. Nakanishi, T. Norisuke, Q. Tran-Cong-Miyata, *Macromolecules*, **2009**, *294*, 163.

[21] S. Tanaka, Y. Kubo, Y. Yokoyama, A. Toda, K. Taguchi, H. Kajioka, *J. Chem. Phys.*, **2011**, *135*, 234503.

[22] T Witten, P. Pincus, S. Koumura, *Structured fluids: Polymers, colloids, surfactants* (in Japanese), Yoshiokashoten, **2010.**

[23] J. Hobley, S. Kajimoto, A. Takamizawa, K. Ohta, Q. Tran-Cong, H. Fukumura, *J. Phys. Chem. B*, **2003**, *107*, 11411.

[24] A. Takamizawa, S. Kajimoto, J. Hobley, H. Fukumura, Q. Tran-Cong, *Phys. Rev. E*, **2003**, *68*, 020501.

[25] J. Hobley, S. Kajimoto, A. Takamizawa, H. Fukumura, *Phys. Rev. E*, **2006**, *73*, 011502.

[26] S. Kajimoto, N. H. Seong, H. Fukumura, D. D. Dlott, *Photochem. Photobiol. Sci.*, **2014**, *13*, 891.

[27] T. G. Dewey, D. H. Turner, *Advances in Molecular Relaxation and Interaction Processes*, **1978**, *13*, 331.

[28] K. Yamamoto, Y. Mizutani, T. Kitagawa, *Appl. Spec.*, **2000**, *54*, 1591.

[29] M. Kasuya, S. Kajimoto, J. Hobley, K. Hatanaka, H. Fukumura, *Jpn. J. Appl. Phys.*, **2006**, *45*, L1016.

[30] S. Kajimoto, D. Shirasawa, N. N. Horimoto, H. Fukumura, *Langmuir*, **2013**, *29*, 5889.

[31] T. A. Klar, S. Jakobs, M. Dyba, A. Egner, W. H. Stefan, *Proc. Natl. Acad. Sci. USA*, **2000**, *97*, 8206.

[32] E. Betzig, G. H. Patterson, R. Sougrat, O. W. Lindwasser, S. Olenych, J. S. Bonifacino, M. W. Davidson, J. Lippincott-Schwartz, H. F. Hess, *Science*, **2006**, *313*, 1642.

[33] M. J. Rust, M. Bates, X. Zhuang, *Nature Methods*, **2006**, *3*, 793.

[34] M. G. L. Gustafsson, L. Shao, P. M. Carlton, C. J. R. Wang, I. N. Golubovskaya, W. Z. Cande, D. A. Agard, J. W. Sedat, *Biophys. J.*, **2008**, *94*, 4957.

[35] M. Beck, M. Aschwanden. A. Stemmer, *J. Microscopy*, **2008**, *232*, 99.

[36] L. Shao, B. Isaac, S. Uzawa, D. A. Agard, J. W. Sedat, M. G. L. Gustafsson, *Biophys. J.*, **2008**, *94*, 4971.

[37] K. Yasui, *Appl. Spec. Rev.*, **2004**, *39*, 399.

[38] A. Takamizawa, Doctoral Thesis, **2005**.

[39] S. Kajimoto, Doctoral Thesis, **2006**.

Chapter 2 Samples and methods

2-1 Introduction

In this chapter, details of samples and methods are described. As a sample solution having the lower critical solution temperature (LCST), water/2-butoxyethanol (2BE) mixtures were mainly used. Furthermore, some reference mixtures were used to compare results of the water/2BE mixtures with the other mixtures for investigation of bubble formation and light emission during laser-induced temperature jump (T-jump).

To investigate the dynamics of laser-induced phase separation (LIPS), bubble formation, and light emission in the mixtures, several experimental methods were employed, for example, time-resolved emission measurements, imaging techniques, nanosecond structured illumination microscopy SIM, and light scattering technique. Fluorescence correlation microscopy was also employed (FCS) to investigate diffusion of solute molecules in water/2BE mixture below the LCST. The principles of these methods and experimental details are described in this chapter.

2-2 Samples

2-2-1 Water/2-butoxyethanol mixtures

2BE is thought to be a nonionic surfactant in a series of poly(ethylene glycol) monoalkyl ether ($CH_3(CH_2)_{i-1}(OCH_2CH_2)_jOH$, C_iE_j), and can be described as C_4E_1. The molecular structure of 2BE is shown in Fig.2-1 (a).[4] 2BE has a hydrophobic alkyl chain part and a hydrophilic ethylene part. It is known that water/2BE mixture splits into two phases from one phase with a temperature rise.[1,2] The mixture has its LCST at 49.3°C and the critical composition is 0.0525 with respect to the 2BE molar fraction χ_{2BE}.[3] The phase diagram of the mixture are shown in Fig.2-1 (b,c).[1,5,6]

2BE was purchased from Wako Pure Chemical Industries Ltd., and used without any purification. 2BE was mixed with water (Millipore, Simplicity UV, 18 MΩ) at various 2BE molar fractions by measuring weight. It is known that the LCST and the critical composition are varied with an impurity.[3] Phase separation temperatures were measured in this study and the measured phase diagram of water/2BE mixture shown in Fig.2-1 (c). The obtained LCST and the critical composition were 49.2°C and 0.052, respectively, indicating that the influence of impurities is not so critical.

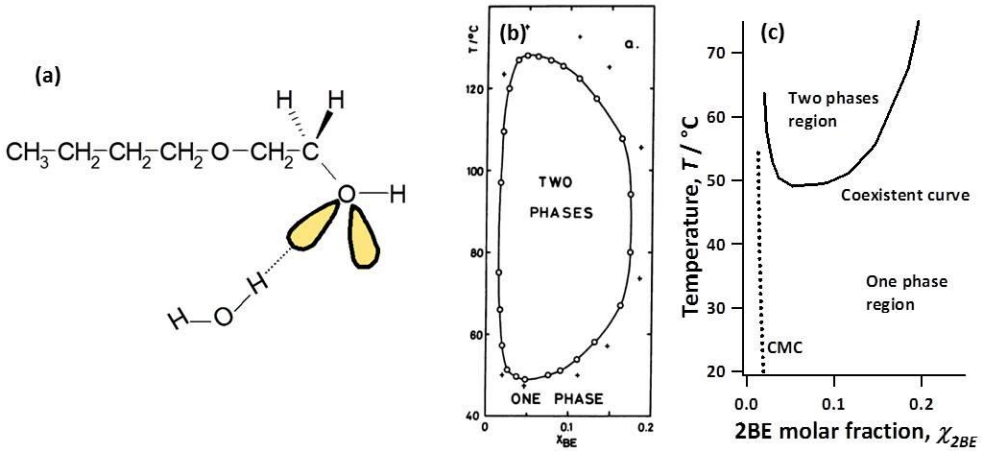

Fig.2-1 (a) Molecular structures of water and 2BE. The hydrogen bond formed between water and 2BE molecules is presented as a dotted line. Ref.4 (b) Phase diagram of water/2BE mixture from Ref.5 (open circles from Ref.1, and crosses from Ref.6). (c) Phase diagram of the mixture measured in this study. A solid line and a dotted line present coexistent curve and CMC of the mixtures, respectively. Ref.9

The addition of salts allows us to lower the LCST of a binary mixture,[5,7,8] and the critical composition also changes. Coexistent curves of water/2BE mixtures with various salt concentrations are shown in Fig.2-2. At χ_{2BE} 0.052 the addition of 0.01 mole fraction KCl reduces phase separation temperature from 49.2°C to25.7°C.

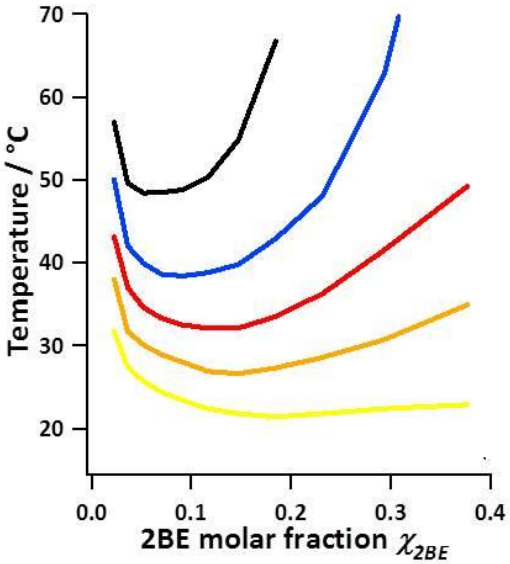

Fig.2-2 Phase diagram of water/2BE mixture with various salt concentrations. Black line : without salt. Blue line : χ_{2BE} 0.0025. Red line : 0.0050. Green line : 0.0075. Yellow line : 0.01.

2-2-2 Reference samples

(a) Water/TEA mixtures

Water/TEA mixture also has its LCST and splits into two phases from one phase with a temperature rise like water/2BE mixture.[2,9] The LCST and the critical composition of the mixture are 18.1°C and TEA molar fraction 0.077, respectively. The molecular structure of TEA and the phase diagram of the mixture are shown in Fig.2-3. TEA was purchased from Wako Pure Chemical Industries Ltd., and used without further purification. The mixture of TEA and water (Millipore, Simplicity UV, 18 MΩ) having the critical composition was prepared by measuring weight. It is expected that the mixture corrodes glasses and impurities may be dissolved into the mixture, due to the high basicity of the mixture. Thus a Teflon flask was used for sample preparation to prevent impurities.

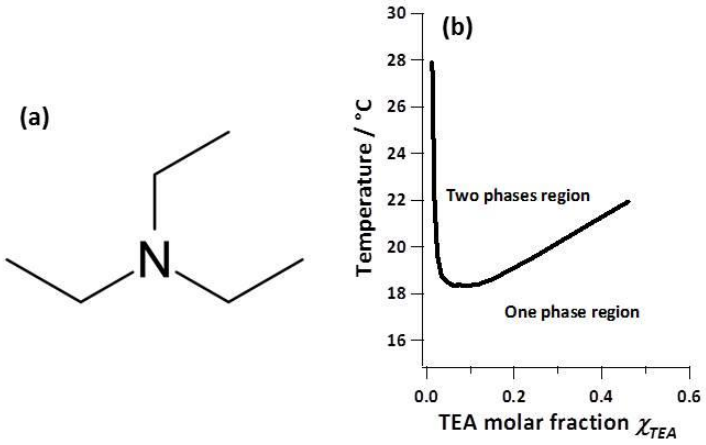

Fig.2-3 (a) Molecular structures of TEA. (b) Phase diagram of water/TEA mixture from Ref.9

(b) Other binary liquid mixtures

For organic aqueous solution, methanol (MeOH), ethanol (EtOH), acetone, and ethylene glycol (EG) were used as organic solvents. MeOH and EtOH are as a mono-alcohol solvent. Acetone is as high volatility solvent. EG is as high viscous and di-alcohol solvent. These organic solvents (spectroscopic grade) were purchased from Sigma-Aldrich Co. LLC. and used without any purification. The organic solvents were mixed with water (Millipore, Simplicity UV, 18 MΩ) at various molar fractions.

(c) Polystyrene Beads

To evaluate the validity of nanosecond SIM, polystyrene Latex beads (Polyscience, Inc., Polybeads Red Microspheres, diameter 1.0 and 3.0 μm) were employed. It is known that Latex beads form a periodic structure on a substrate (Fig.2-4).[10,11] The Latex beads suspension was

2-fold diluted by methanol (Wako Pure Chemical Industries, spectrophotometric grade) and Triton X-100 (Sigma Aldrich, laboratory grade) mixture (volume ratio MeOH : Triton-X = 400 : 1). The diluted solutions are drop cast on cover glass (Matsunami Glass Ind., LTD).

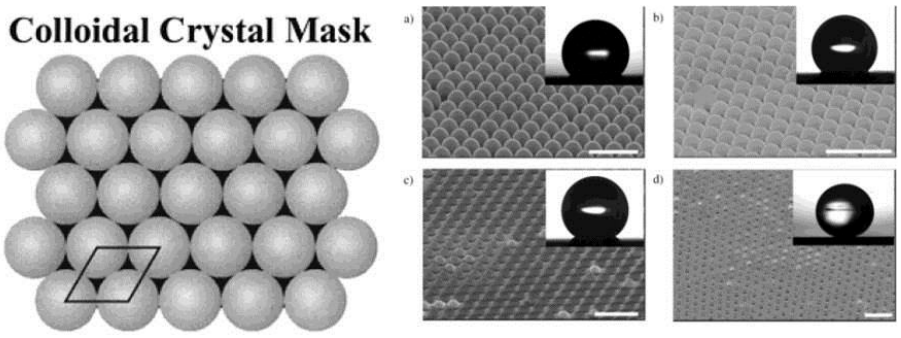

Fig.2-4 Left : schematic image of a periodic structure formed on a substrate. Right : SEM images of the polystyrene beads and the water contact angle measurement on the corresponding modified surfaces (insets). The diameters of polystyrene beads and water contact angles on these surfaces were measured to be (a) 400 nm, 135°, (b) 360 nm, 144°, (c) 330 nm, 152°, and (d) 190 nm, 168°. Bar: 1 μm. Ref.11.

2-2-3 Fluorescent dye

Two fluorescent dyes were used as fluorescent probe for fluorescence-imaging and the dynamical changes of solvent environment during phase separation. One was rhodamine B (RhB, Wako Pure Chemical Industries, Ltd), and the other was N,N'-Bis(2,6-dimethylphenyl)perylen -3,4,9,10-tetracarboxylic diimide (BPDI, Santa Cruz Biotechnology, Inc.). The molecular structures of these dyes are shown in Fig.2-5. Both fluorescent dyes were dissolved in water/2BE mixture having the critical composition, and concentrations of the dyes were 5.0 x 10^{-5} M. RhB is an amphiphilic molecule, while BPDI is highly hydrophobic molecules. The fluorescence dyes have differences in fluorescence efficient between in water- and 2BE-rich phases after phase separation. BPDI in 2BE-rich phase at 55°C showed approximately 50 times higher efficiency than in water-rich phase. And RhB in 2BE-rich phase showed approximately 8 times higher efficiency than in water-rich phase. These differences allow us to visualize 2BE phase during phase separation.

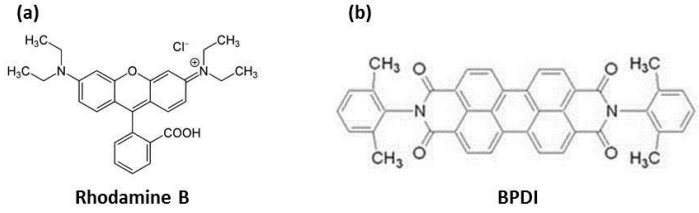

Fig.2-5 Molecular structures of rhodamine B (a) and BPDI (b).

In fluorescence correlation spectroscopy measurements, as fluorescent dyes, two organic compounds having differing solubility in water were used. The first one was BPDI (Sigma Aldrich, dye content > 90 %). The molecular structure of BPDI was already shown in Fig.2-5 (b). This dye is bright (molar extinction coefficient 3.50 x 10^4 at 532 nm, fluorescence quantum yield > 0.97) and highly hydrophobic. The second one was ATTO 532 NHS ester (ATTO 532, ATTO Tec), which is a derivative of rhodamine 6G. The molecular structure of ATTO 532 is shown in Fig.2-6. This dye is also bright (molar extinction coefficient = 1.15 x 10^5 at 532 nm, fluorescence quantum yield > 0.90), but is amphiphilic. These dyes were used without further purification. The fluorescent dyes were dissolved in water/2BE mixtures at various molar fraction of 2BE. The concentrations of the dyes were kept at 10 nM for all molar fractions.

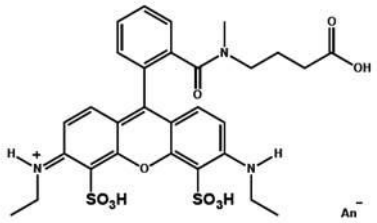

Fig.2-6 Molecular structure of ATTO 532.

2-2-4 Sample cell

Two types of sample cells were employed to change sample thickness. In the first, the sample solutions were circulated in a flow cell with a pump (Fig.2-7). The flow cell was made of quartz and the thickness was 100 μm. A Teflon-sealed pump and tubes were used for flow paths to prevent impurities. The sample temperature was controlled with a temperature controllable water bath. Before experiments, inside of the pump and the tubes were washed by circulating the sample solution. 200 mL of sample solution was used at every experiment. Advantages of this sample configuration is that one can easily freshen sample after each near IR pulse was irradiated and one can control the sample thickness. Disadvantage of this system was temperature graduation along a near IR beam direction. A near IR (1.88 μm) pulse was used to induce a rapid temperature jump and phase separation. The optical absorbance of the mixture with 100 μm thickness at 1.88 μm was 0.47, indicating that the transmittance of the near IR pulse was less than 40% and the magnitude of T jump at back surface was less than half of that at front surface. This type of sample cell was mainly used for investigation of bubble formation and light emission during laser-induced T-jump described in chapter 6.

Fig.2-7 Picture of a flow cell (thickness 100 μm).

In the second sample cell, sample solution was put between two slide glasses (Matsunami Glass Ind., LTD, thickness 1.0 ~ 1.2 mm) without any spacer. The sample thicknesses were estimated to be less than 10 μm. The sample temperature was kept at 24°C by using a temperature controlled brass sample holder (Fig.2-8). Advantage of this sample configuration is that one can minimize the temperature graduation effect and a multiple scattering effect, so that one can obtain a clear image of phase separating mixture. Disadvantage of that was that it is difficult to control sample thickness precisely and to freshen the samples at each near IR pulse irradiation. This type of sample cell was used for investigation of LIPS dynamics described in chapter 5.

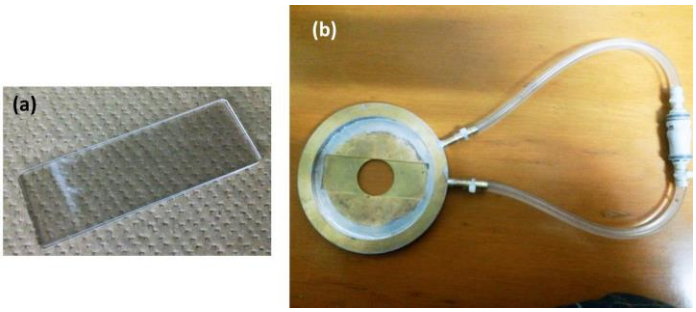

Fig.2-8 Picture of thin sample (a) and a brass sample holder (b).

2-3 Methods

2-3-1 Temperature jump method

To accomplish a rapid temperature rise and investigate phase separation dynamics of a binary mixture after the temperature rise, laser-induced T-jump method was employed.[12] In this method, combination tone of the OH stretching and bending vibration and over tone of water molecule are directly excited by irradiation of a near IR laser pulse (1.88 μm). Absorption spectrum of water in near IR region is shown in Fig.2-9 (a). Absorption coefficient of water at 1.88 μm is 1.19 corresponding to absorbance 0.63 with 100 μm optical path. If the absorbance of solution was too high, the optical

absorption of water took place at only front surface of a sample. On the other hand, if the absorbance of solution was too small, it was difficult to increase a temperature of the sample. At 1.88 μm, the absorbance seems to be easy to handle. When width of the near IR pulse is several nanoseconds, it is expected that T-jump induced by the near IR laser pulse occurs within width of the near IR laser pulse, because the vibrational relaxation into a neighboring molecule in a liquid takes place within picosecond order time scale. Yamamoto et al. have reported that the T-jump occurs within the width (Fig.2-9 b).[13] The T-jump enables us to observe phase separation dynamics with a deep quench (several K) within several nanoseconds.

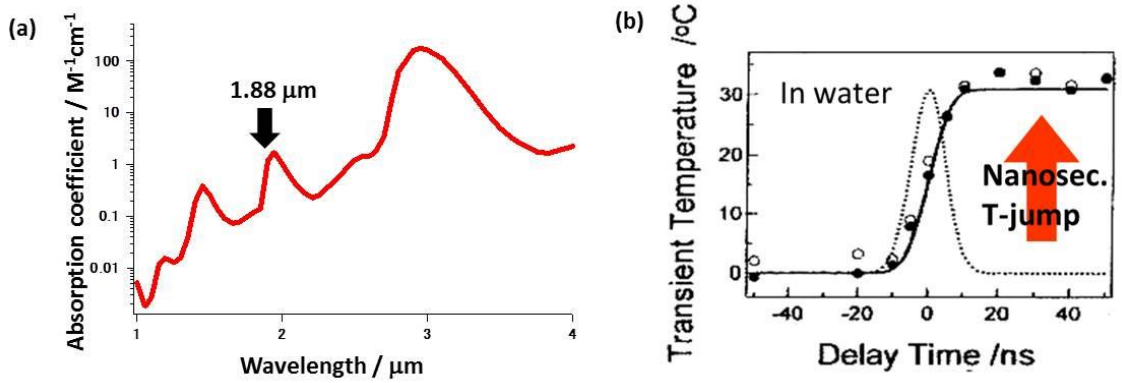

Fig.2-9 (a) Absorption spectrum of water at near IR region. A black arrow points the wavelength 1.88 μm. (b) Magnitude of T jump as a function of delay time. Ref.13

The near IR pulse was obtained by Raman shifting fundamental of a Nd:YAG laser (SpectraPhysics, 1064 nm, 8 ns, 10 Hz) using high pressure H_2 gas.[14,15] A scheme of experimental setup for generating the near IR pulse is shown in Fig.2-10. An intense fundamental pulse is focused into a cylinder which contains high pressure H_2 gas. The cylinder is called Raman shifter. The Raman shift is 4160 cm^{-1} and the wavelength of the obtained near IR pulse is approximately 1.88 μm. The Raman shifted laser pulse is amplified by stimulated Raman scattering photons and becomes to be coherent, when an intensity of the fundamental laser pulse becomes above a certain threshold. This system is known as a Raman laser. It was reported that width of a near IR laser pulse obtained from Raman shifter is almost the same as width of an incident laser pulse.

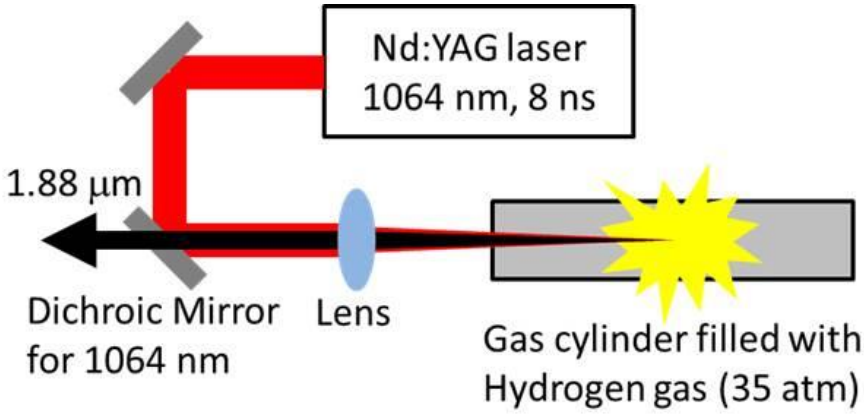

Fig.2-10 Scheme of a Raman shifter.

The magnitude of the T-jump ΔT in a sample solution was estimated by the following equation (3-1).

$$\Delta T = \frac{I(1-10^{-A})}{C_p \rho x} \qquad (3\text{-}1)$$

where, A is an optical absorbance, $A = \varepsilon c x$, ε is a molar absorption coefficient ($mol^{-1}cm^{-1}$), c is a concentration of a sample solution (mol/L), x is optical length (cm), I is an intensity of a pump beam (J/cm^2 · pulse), C_p is a heat capacity at constant pressure (J/g · K), ρ is a density (g/cm^3). Some optical and physical parameters of water and 2BE that used for the calculation of the magnitude of the T-jump in water/2BE mixture at the critical composition are summarized in Table 3-1. Since ε, c, C_p, and ρ of each component in a mixture are different from those of each, it is required to consider the volume ratio of each component (Table 3-2). In the case of water/2BE mixture, the volume fraction of water is 71.52. The optical absorbance for 10 μm of optical path is calculated to be 0.047. When the intensity of the pump beam is 1.0 J/cm^2· pulse, the magnitude at the front surface is calculated at 28.29°C.

Table 3-1 Optical and physical parameters of water and 2BE.

	water	2BE
Concentration, *c* (mol/L)	**55.40**	**7.63**
Molecular weight (g/mol)	**18.02**	**118.17**
Molar absorption coefficient at 1.88 μm, ε ($mol^{-1}cm^{-1}$)	**1.19**	**0.09**
Heat capacity at constant pressure, C_p (J/g · K)	**4.18**	**2.29**
Density, ρ (g · cm^3)	**1.00**	**0.90**
Volume ratio	**71.52**	**28.48**

Table 3-2 Optical and physical parameters of a water/2BE mixture at the critical composition.

Optical absorbance, *A*	$(\varepsilon_{water}c_{water} \times \frac{71.52}{100} + \varepsilon_{2BE}c_{2BE} \times \frac{28.48}{100}) \times x$
Heat capacity at constant pressure, C_p (J/g・K)	$C_{pwater} \times \frac{71.52}{100} + C_{p2BE} \times \frac{28.48}{100}$
Density, ρ (g・cm^3)	$\rho_{water} \times \frac{71.52}{100} + \rho_{p2BE} \times \frac{28.48}{100}$

2-3-2 Spectroscopic studies

(a) Streak camera

Figure 3-11 shows the operating principle of a streak camera.[16] When a fluorescence signal comes into a photocathode, the signal is converted into photoelectrons in proportion to the number of incident photons. The photoelectrons are accelerated and pass between two deflection electrode plates by an accelerating electrode. A high-speed sweep voltage is applied to the deflection plates so that the photoelectrons are swept from top to bottom when they pass through the deflection plates. Then the swept photoelectrons are multiplied with the microchannel plate (MCP), and reconverted into an optical image by a phosphor screen. The optical image captured on the phosphor screen is called the streak image. In the streak image, time is converted into the vertical axis. In addition, if a spectrograph is used in front of a streak camera to obtain a spectrum, the spatial information in the horizontal direction on the streak image can show a spectrum of the fluorescence signal. Therefore, by using the streak camera, one can obtain a time-resolved fluorescence spectrum.

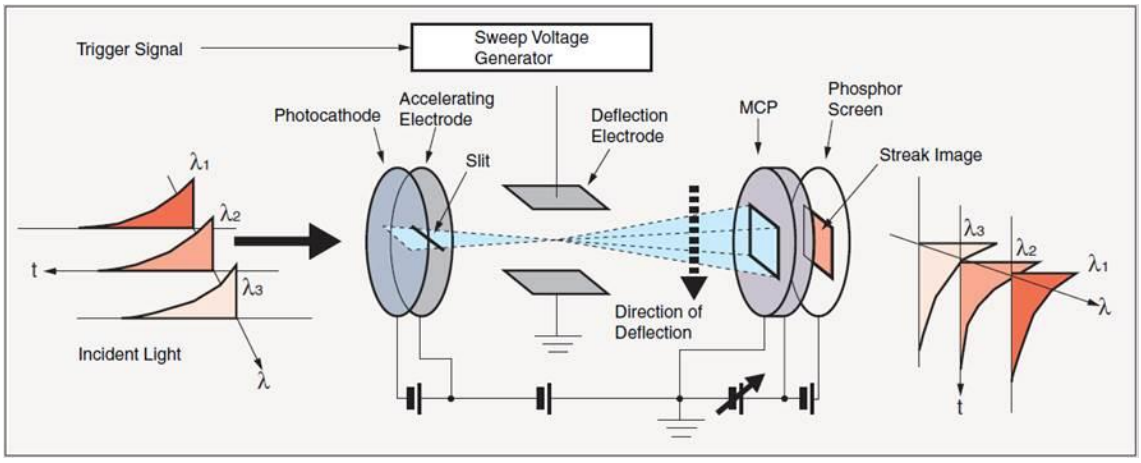

Fig.2-11 Operating principle of the streak camera. Ref.16.

A streak camera (Hamamatsu Photonics, C10627) and a spectrograph (Hamamatsu Photonics, C11119-01, slit size 100 μm) were used. In this experiment, the circulation system and a 100 μm flow cell for sample solutions described above were employed. An optical surface of the flow cell faced to the streak camera, and was irradiated with a near IR pulse with an angle approximately 45° (Fig.2-12). Emission signals induced by the near

IR pulse were collected with two convex lenses (f = 70 mm) made of synthesized quartz to prevent optical absorption with the convex lens. The signal collection system was optimized by detecting fluorescence signals of rhodamine B dissolved in the water/2BE mixtures excited with a green laser pulse (Quantel, Nd:YAG second harmonic 532 nm, 6 ns). The spatial overlap between the green pulse and the near IR pulse was confirmed by checking the transmitted green pulse at a certain delay time after the IR pulse irradiation. When these two pulses spatially overlapped, the shape of transmitted green pulse was clearly modified due to an inhomogeneity induced the near IR pulse irradiation. The integration time for emission spectrum measurements were 2 hours. Background measurements were carried out by masking on the collecting lens.

Fig.2-12 Scheme of experiment setup for time-resolved emission spectrum measurement.

(b) Transient fluorescence measurements

To investigate dynamical changes of solvent environment during LIPS of the water/2BE mixtures, transient fluorescence spectra were measured at various delay times. The measurements were performed with a spectrograph (Princeton Instruments, Acton, SP150, slit size 100 μm) and a cooled charge-coupled device (CCD) camera (iDus, Andor Technology, -50°C, 1024 x 256 pixels^2). The circulation system and a 100 μm flow cell for sample solutions were employed in the measurements. An optical surface of the flow cell faced to the spectrograph, and was irradiated with a near IR pulse with an angle 45°. Fluorescence signals of dye molecules excited by a green pulse laser (Quantel, Nd:YAG second harmonic 532 nm, 6 ns) with a certain delay time after T-jump were collected with two convex lenses (f = 100 mm) made of synthesized quartz to prevent optical absorption with the convex lens. The delay time between the near IR pulse and the green pulse was electrically controlled with a digital delay generator (Stanford Research System DG535).

2-3-3 Fluorescence correlation spectroscopy

(a) Experimental setup

A confocal microscope (Leica TCS SP5 X) was used for recording the fluorescence signals for the FCS analysis. The excitation wavelength was 532 nm, which was selected from a white light laser integrated to the confocal microscope. The repetition rate of the laser was 80 MHz. FWHM of the laser pulses was set at a few hundred picoseconds. The laser beam was focused with a microscope lens (Leica HCX PL APO 63x 1.2 W wRR CS, water immersion) and its power was about 70 μW in front of the sample. The fluorescence signal was collected through the same microscope lens and directed to the detection pathway by an acousto-optic beam splitter. The fluorescence signal was filtered by a bandpass filter (Brightline FF01-582/75-25, Semrock, USA) and then divided by a 50-50 beam splitter for independent detection by two avalanche photo-diodes to allow removal of afterpulsing by cross-correlation.[40] Cross correlation of the fluorescence signal recorded by the different detectors was applied to get an after-pulse-free FCS graph. Single-photons were registered by time-correlated single photon counting (TCSPC) using a Picoharp 300 (Picoquant Germany). The signals obtained were analyzed with the related analysis software for fluorescence lifetime imaging and fluorescence correlation spectroscopy (Symphotime, Picoquant, Germany). Fluorescence signals were recorded over 3 minutes. All FCS measurements were repeated three times and performed at room temperature (24°C) which is below the LCST of water/2BE mixture. The correction collar of the microscope objective was adjusted to a cover glass thickness of 0.15 mm using 8 well chamber systems with glass bottom (Nunc Lab Tek No.1, n = 1.52). The depth in the sample was kept at 50 μm in all FCS measurements by first focusing on the reflection of the glass surface and subsequently lifting the piezo-controlled microscope objective by 50 μm. The concentrations of BPDI and ATTO 532 NHS ester were kept at 10 nmol/L. The LCST and the critical composition of the mixture were not affected by the addition of the two dyes as solutes. Prior measurements for the instrument were calibrated using Rhodamine 6G for comparison with literature values.

(b) Data analysis

The following three models describing the diffusion of single component (eq.3-2), of two components (eq.3-3) and of a single component with anomalous diffusion (eq.3-4) were applied to the data to determine the most suitable model[17, 18]

$$G(\tau) = \frac{1}{\langle N \rangle}\left(1 + \frac{\tau}{t_d}\right)^{-1}\left(1 + \frac{\tau}{\mathrm{k}^2 t_d}\right)^{-\frac{1}{2}}\left(1 + \frac{F}{1-F} exp\left(-\frac{\tau}{t_t}\right)\right) \qquad (3\text{-}2)$$

$$G(\tau) = \frac{1}{\langle N \rangle}\left(Y\left(1+\frac{\tau}{t_{d1}}\right)^{-1}\left(1+\frac{\tau}{\mathrm{k}^2 t_{d1}}\right)^{-\frac{1}{2}} + (1-Y)\left(1+\frac{\tau}{t_{d2}}\right)^{-1}\left(1+\frac{\tau}{\mathrm{k}^2 t_{d2}}\right)^{-\frac{1}{2}}\right)\left(1+\frac{F}{1-F}exp\left(-\frac{\tau}{t_t}\right)\right) \quad (3\text{-}3)$$

$$G(\tau) = \frac{1}{\langle N \rangle}\left(1+\left(\frac{\tau}{t_d}\right)^{\alpha}\right)^{-1}\left(1+\left(\frac{\tau}{t_d}\right)^{\alpha}\frac{1}{k^2}\right)^{-\frac{1}{2}}\left(1+\frac{F}{1-F}exp\left(-\frac{\tau}{t_t}\right)\right) \quad (3\text{-}4)$$

In all equations $\langle N \rangle$ is the average number of molecules in the effective confocal volume, t_d is the diffusion time, k is an aspect ratio of the effective confocal volume, F is the fraction of triplet state and t_t is the triplet lifetime, Y is the fraction of the diffusion component 1, t_{d1} and t_{d2} are the diffusion times of diffusion component 1 and 2, respectively, and α is anomaly factor. The correlation function $G(t)$ of BPDI at a 2BE molar fraction of 0.064 is shown in Fig.2-19. To evaluate the quality of the fit, the residuals of both fitting results with eq. 3-2, 3-3, and 3-4 are plotted in Fig.2-13. The same evaluation was carried out for all experimental conditions. As exemplified for the data in Fig.2-13, significant differences between the residuals of the different models were never found. The same analysis was carried out for all 2BE molar fractions. And then the same trend was observed. According to Occam's razor, all subsequent analysis the data presented here is based on the diffusion model for a single component model (eq.3-2).

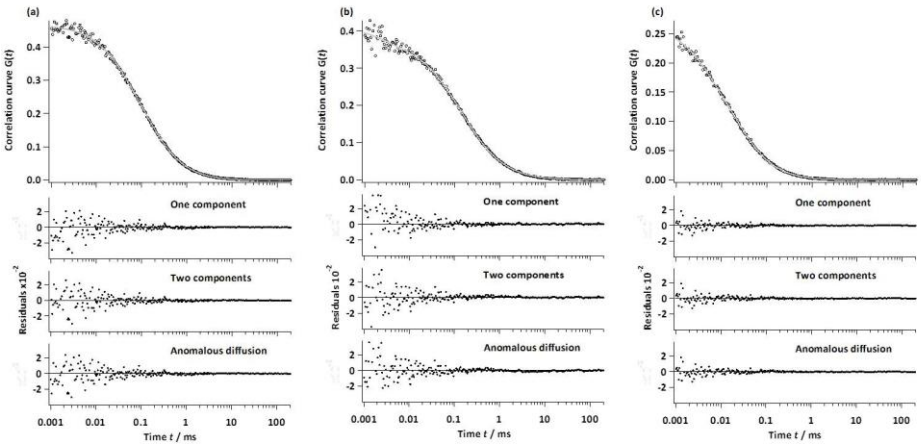

Fig.2-13 Correlation curves along with the fit to the one component diffusion plus triplet model, and the residuals of the fits by using the one component diffusion plus triplet model, the two components diffusion plus triplet model, and the anomalous diffusion plus triplet model. (a) BPDI in water/2BE mixtures at 2BE molar fraction 0.064. (b) ATTO 532 NHS ester in water/2BE mixtures at 2BE molar fraction 0.064. (c) BPDI in water/MeOH mixtures at 2BE molar fraction 0.064.

2-3-4 Imaging techniques

(a) Shadowgraph imaging

Light can go ahead through a medium in which a refractive index is uniform. However, in medium which the refractive index is not homogeneous, light is refracted and reflected, and cannot go ahead. Therefore transmitted light gives us information of the spatial distribution of refractive index in the medium. After phase separation occurs in a sample solution, refractive index of the sample solution becomes inhomogeneous, so that one can observe the macroscopic phase formation and growth by using shadowgraph imaging technique.

The apparatus used for shadowgraph-imaging is shown in Fig.2-14. The shadowgraph-imaging were performed on an inverted microscope system (Nikon, Eclipse Ti-U). A sample solution was irradiated by a near IR pulse with an angle 30° to induce a rapid T-jump and phase separation. Fluorescence from 10^{-4} M RhB MeOH solution excited by a green laser pulse (Quantel, Nd:YAG second harmonic 532 nm, 6 ns) was used as a flash illumination light source. Since fluorescence lifetime of RhB in MeOH is approximately 2.5 ns,[19] the flash light source allows a nanosecond time-resolved imaging. The flash light illuminated a sample solution from the upper side. Transmitted light images were taken with an objective lens and a cooled CCD camera (DV435, Andor Technology, -45°C, 1024 x 1024 pixels^2). As the objective lens, Nikon, 40 X, N.A. 0.6 and Nikon, 10 X, N.A. 0.3 were used for imaging of phase separating medium and bubble formation, respectively. The CCD exposure time was 0.08 s. The CCD acquisition timing and a delay time between the near IR pulse and the flash light were electrically controlled by using a digital delay generator (Stanford Research System DG535).

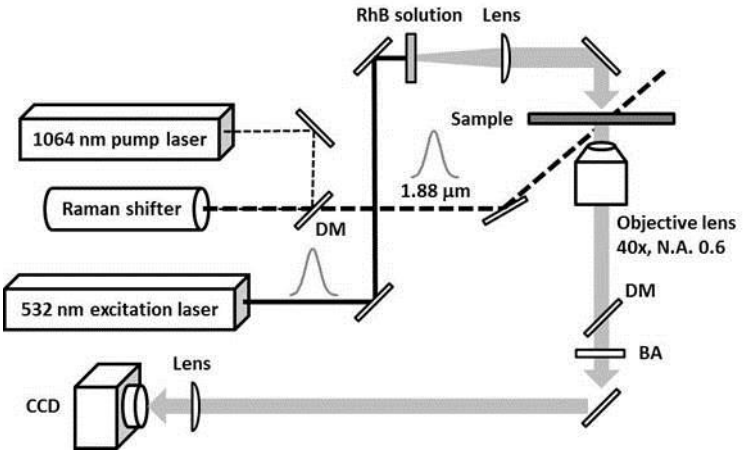

Fig.2-14 Scheme of experiment setup for shadowgraph imaging. DM : dichroic mirror, BA : band pass filter.

All images were analyzed by using MATLAB (Mathworks, Inc.). Processes for determination of phase domain size are explained here. These analysis processes are summarized and shown in Fig.2-15. A dark image was subtracted from the obtained images taken at various delay time after T-jump. The dark image was taken without the near IR pulse and the flash light. To minimize an effect of image edges, a two dimensional (2D) Hann window function was multiplied with the subtracted images. By multiplying the Hann window function, values of images at the edges became zero. The images were then 2D fast Fourier transferred (2D FFT) and the FFT images were averaged with more than 20 images. The 2D FFT images give spatial frequency information of the shadowgraph images. A power spectrum was calculated as a radial distribution of an averaged FFT image with the central point. The analysis processes described above were applied to images taken at delay time 100 ns. At this delay time, it is expected that temperature of the sample solution was already equilibrated and macroscopic phases were still not formed. The power spectrum obtained at the delay time of 100 ns was used as base line. Generally one should use a base line taken at negative delay time. The delay time 100 ns was selected in order to eliminate an influence of the T-jump and extract macroscopic phase growth. The analyzed power spectrum at 100 ns was subtracted from the power spectra at various delay time. A final power spectrum was obtained for each delay time. The MATLAB m-file for the analysis of power spectrum is shown in appendix A.

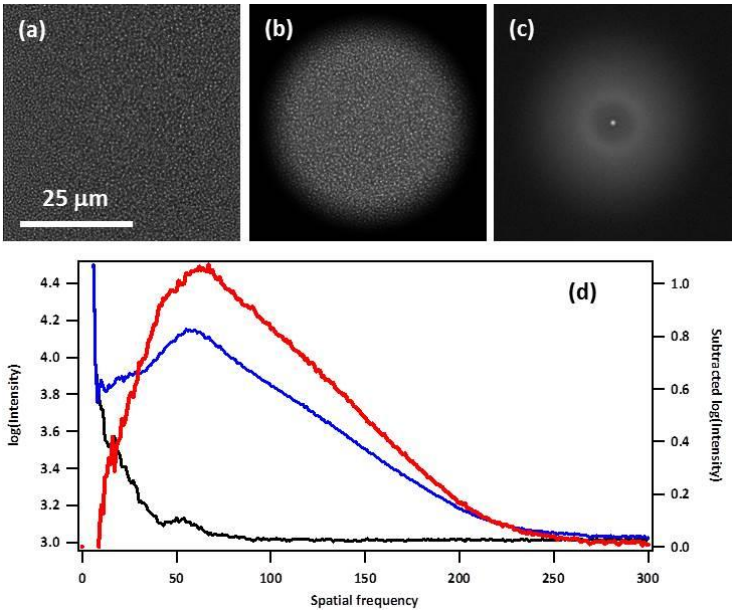

Fig.2-15 Summary of image analysis for obtaining a power spectrum. (a) Raw image taken at delay time 100 µs. (b) Multiplying with a 2D Hann function to minimize edge effect. (c). Averaged 2D FFT image. (d). Power spectra as a radial distribution of an averaged FFT image with the central point. Black and blue lines present power spectra at delay time 100 ns and 100 µs (Left axis). A red line presents a subtracted power spectrum (Right axis).

In the second place, processes for determination of bubble size and counting those numbers are explained here. These analysis processes are summarized and shown in Fig.2-16. If a bubble is captured in a shadowgraph image, the bubble can be observed as a low intensity spot due to a light reflection at liquid-gas interface. As a base image, more than 20 shadowgraph images were taken at delay time of 100 ns after T-jump and averaged. The raw shadowgraph image was subtracted from the averaged base image. After that, the bubble can be observed as a bright spot. The subtracted image was binarized with a certain threshold which depended on experimental condition. The number and size of bright spots were determined by using commands in DIPimage toolbox for MATLAB. A MATLAB m-file for the analysis of bubbles is shown in appendix B.

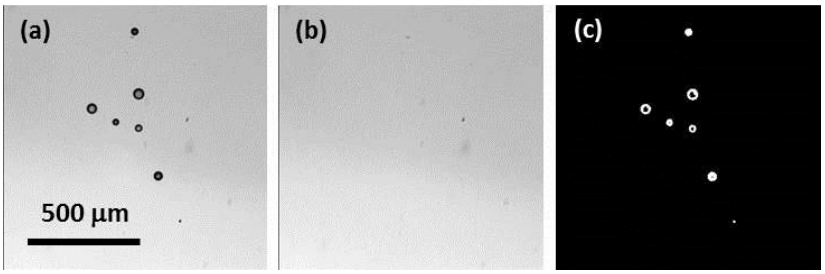

Fig.2-16 Summary of image analysis for obtaining the number and size of bubbles. (a) Raw image. (b) Base image. (c) Subtracted and binarized image of (a).

(b) Visualization of emission

To characterize light emission during LIPS, light emission spots were visualized by using the same experimental setup for shadowgraph-imaging without any illumination. Two CCD cameras were used in the experiments. The first was cooled CCD camera, iKon (Andor Technology, -50°C, 512 x 512 pixels^2). In this case, CCD record time was 10 s, so that this setup does not allow us nanosecond time-resolved measurement. The second was time-gated intensifier CCD (iCCD) camera, iStar (Andor Technology, -30°C, 1024 x 1024 pixels^2). In this case, it is possible to observe the emission spots images with nanosecond time-resolution.

All images were analyzed by using MATLAB (Mathworks, Inc.). These analysis processes are summarized and shown in Fig.2-17. At first, intensity histogram (Fig.2-17 (b)) was made from of a raw image taken without near IR irradiation (Fig.2-17 (a)). Since exposure time was 10 s and so long, some bright spots due to cosmic rays were captured on the raw image (Fig.2-17 (a) pointed with arrows). From the histogram, the maximum value of white noise (Fig.2-17 (b) inset) was determined and defined as a threshold. Then a raw image taken with near IR irradiation (Fig.2-17 (c)) was binarized with the threshold (Fig.2-17 (d)). From the binarized image, the number of bright spots was determined by using commands in DIPimage toolbox for MATLAB. A MATLAB m-file for the analysis of emission spots is shown in appendix C.

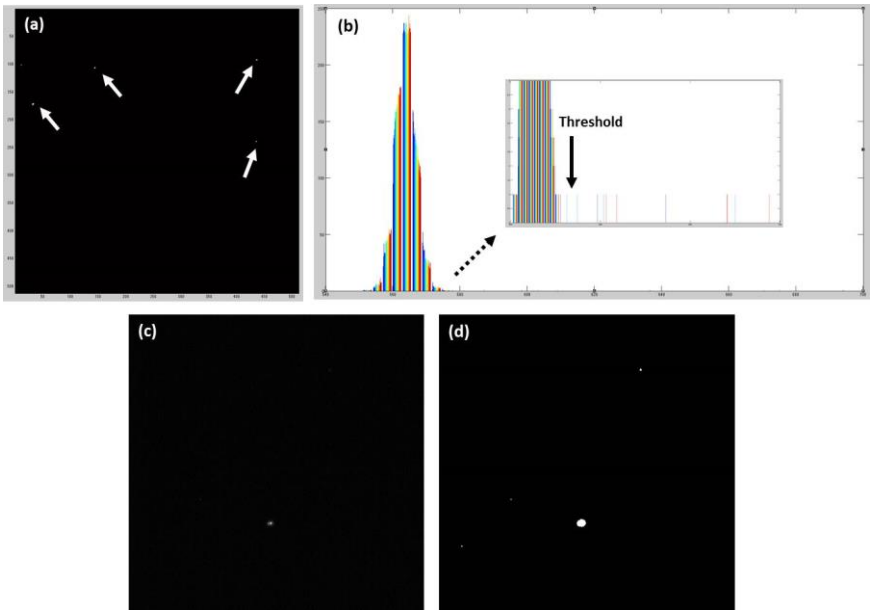

Fig.2-17 Summary of image analysis for obtaining the number of emission spots. (a) Raw image without near IR pulse irradiation. (b) Histogram of the raw image (a). (c) Raw image with near IR pulse irradiation. (d) Binarized image of (a) with a threshold.

2-4 Nanosecond structured illumination microscopy

(a) Concept

The imaging properties of an optical microscope can be described by the point spread function (PSF) or its Fourier transform (FT), the optical transfer function (OTF) [20] as mentioned in Chapter 2. The resolution limit of the microscope is determined by the “support” of the OTF, the region of reciprocal space where the OTF has nonzero values (Fig.2-18). An observed image is a convolution of a sample structure and the PSF in real space and therefore, in reciprocal space, the observed image’s FT is the pointwise product of the sample structure’s FT and the OTF. A microscope can only detect information of within the OTF support, also known as the observable region. The improving the resolution limit is equivalent to enlarging effective OTF support than the normal observable region.

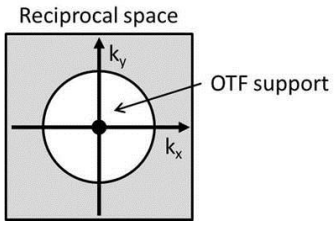

Fig.2-18 Optical transfer function.

In SIM, spatially structured illumination (SI) is used as excitation light source for fluorescent dye. Generally, to obtain a super-resolution image, several images are taken with different phases and orientations of the SI pattern, as described in Chapter 2. From these raw images, several bands of displaced information are separated by solving a simultaneous equation. The displaced bands are then translated to their respective true positions in reciprocal space, and reassembled into a single image with extended spatial frequency bandwidth. The reassembled image contains information out to twice the radius of the normally observable region, and thus, when re-transformed to real space, generates an image with twice the resolution of a conventional microscope.[20,21] The reconstruction procedure is summarized in Fig.2-19. Therefore temporal resolution of the method is not so high.

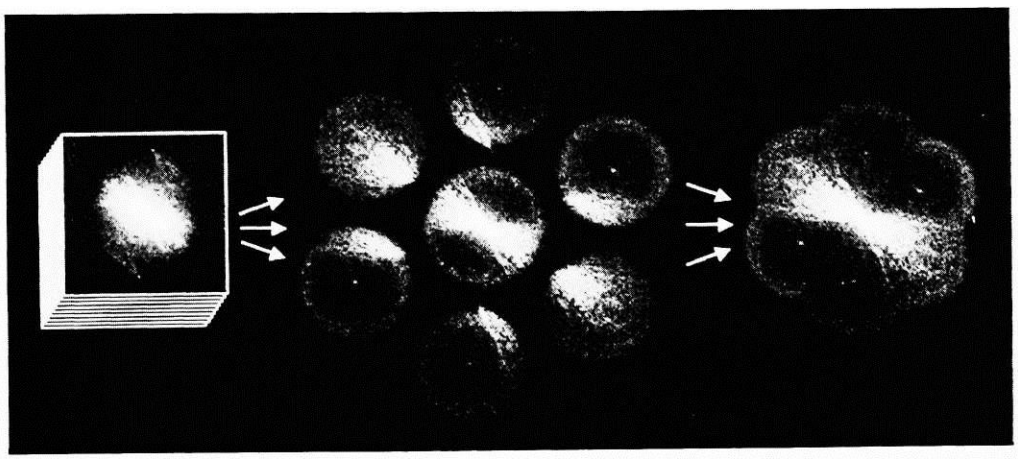

Fig.2-19 Reconstruction procedure shown in reciprocal space. Left : A series of images of the sample are acquired with different phases and orientations of the illumination structure. Center : From these raw images, several bands of displaced information are separated. Right : The displaced bands are then translated to their respective true positions in reciprocal space, and reassembled into a single image with extended spatial frequency bandwidth. Ref.20

However, it is expected that, when a sample itself has a single periodic structure like binary mixture during phase separation, SIM allows us to detect super-high spatial frequency beyond the diffraction limit of a microscope used. In the case, the sample shows a characteristic pattern corresponding to the sample periodicity in reciprocal space. As examples, conceptual image of the phase separating medium is shown in Fig.2-20 Left. In the case, a ring pattern is expected to be observed. When SI is used, frequency shifts are observed due to Moire effect as mentioned in Chapter 1 (Fig.2-20 Right). In the case of a sample having smaller periodicity than the spatial resolution of the microscope, a ring pattern disappears into unsupport region of the OTF.

However, when SI is used, it is expected that the ring pattern shifts into OTF support region due to Moire effect, and a fraction of the ring pattern is observed (Fig.2-21). Since spatial frequency of SI is known, real spatial frequency of the sample can be determined from the shifted ring pattern.

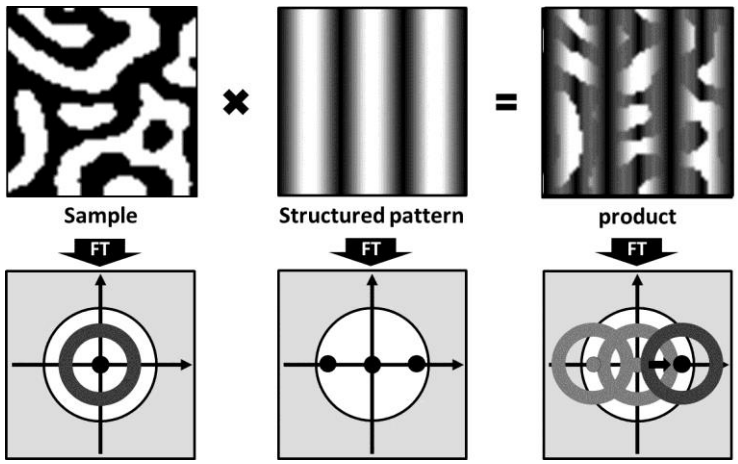

Fig.2-20 Upper and lower images show real space images and reciprocal space images, respectively. Left : phase separating medium. Center : Structured illumination pattern. Right : Observed image.

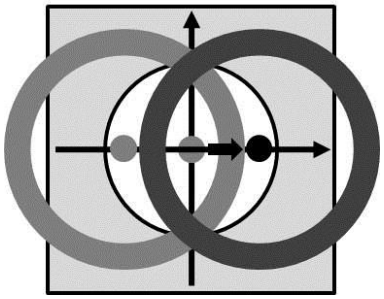

Fig.2-21 Shifted ring pattern with structured illumination.

(b) Experimental setup

The apparatus used for fluorescence-imaging and nanosecond SIM is shown in Fig.2-18. The experiments were performed on an inverted microscope system (Nikon, Eclipse Ti-U). A sample solution was irradiated by a near IR pulse with an angle 30° to induce a rapid T-jump and phase separation. As fluorescent dyes, BPDI and RhB were used as described in section 3-22. A green laser pulse (Quantel, Nd:YAG second harmonic 532 nm, 6 ns) was used as an excitation beam to illuminate the sample on the microscope with a wide-field arrangement by focusing at the back aperture of an objective (Nikon, 40 x, N.A. 0.6). The spatial overlap between the probe beam and the near IR pulse was verified from shadowgraph and fluorescence images. The probe beam diameter at the sample was approximately 200 μm. Fluorescence images were taken with the same

objective lens and a cooled CCD camera (DV435, Andor Technology, -45°C, 1024 x 1024 pixels^2). The CCD exposure time was 0.08 s. The CCD acquisition timing and a delay time between the near IR pulse and the flash light were electrically controlled by using a digital delay generator (Stanford Research System DG535).

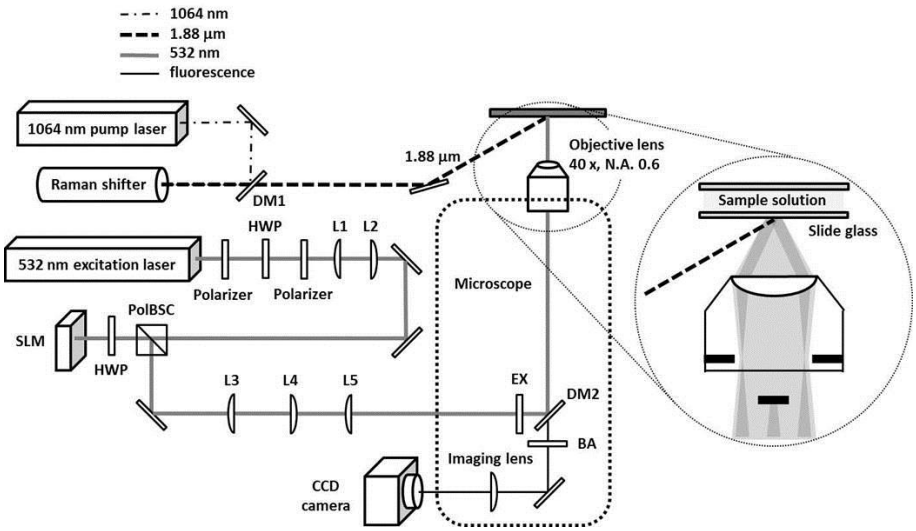

Fig.2-22 Experimental setup for nano-second time-resolved SIM. DM1 = 1064 nm dichroic mirror. HWP = half-wave plate. L = lens, f = 50 mm (L1), f = 120 mm (L2), f = 300 mm (L3), f = 400 mm (L4), f = 300 mm (L5). PolBSC = polarizing beam splitter cube. SLM = spatial light modulator. EX = excitation filter, EX540/25. DM2 = dichroic mirror, DM565. BA = Band pass filter, BA605/55. CCD = charge-coupled device.

The green laser pulse passed through a set of two polarizers and a half-wave plate set for changing the laser polarization to parallel with an optical table and expanded with two convex lenses (L1 and L2 in Fig.2-22). The expanded pulse passed through a polarized beam splitter and a half-wave plate and reflected with a spatial light modulator (SLM, Hamamatsu Photonics, LCOS-SLM X10468). The SLM is a liquid crystal on silicon (LCOS) type spatial modulator. A picture and schematic structure of the SLM is shown in Fig.2-23 (a) and (b).[22] By displaying a bitmap image with 256-level gray scales on the optical surface, it is able to modulate phase of an incident light. To obtain uniform illumination (UI) or structured illumination (SI), a uniform bitmap image or a strip pattern bitmap image were displayed on the SLM, respectively (Fig.2-23 (c) and (d)). In the case of SI, the SLM worked as a grating, and split the green pulse beam into several order diffracted light beams. The first-order diffracted light beams passed three lenses (L3, L4, and L5 in Fig.2-22), and were focused at the back aperture of the objective lens, and then overlapped at the focus plane with each other. As interference pattern between the

first-order diffracted light, SI was obtained (Fig.2-23 (f)). To obtain high quality SI, the position of these three lenses must be correctly aligned along the beam direction. Furthermore, the green pulse can easily damage the objective lens by focusing at the back aperture. Therefore, it was necessary to align experimental setup with much attention.

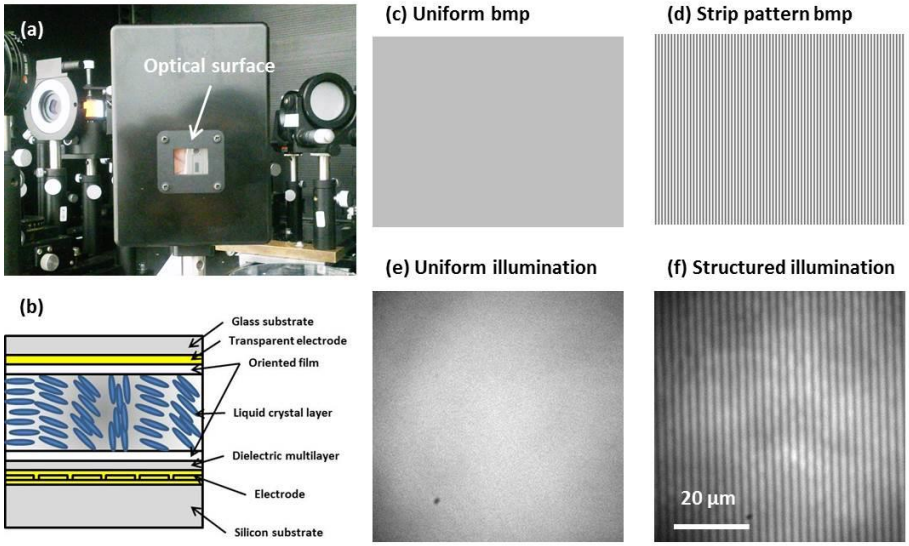

Fig.2-23 (a) Picture of the SLM. (b) Schematic structure of the SLM. (c,d) Bitmap images displayed on the SLM. (e,f) Fluorescence images taken with UI and SI, respectively.

(c) Data analysis

All fluorescence images were analyzed using MATLAB (Mathworks, Inc.). Processes for determination of phase domain size in fluorescence-imaging with UI were the same to the shadowgraph-imaging described in above. In the case of SI experiments, a power spectrum was calculated as a radial distribution with a shifted central point. A MATLAB m-file for the analysis of emission spots is shown in appendix D.

2-3-6 Light scattering technique

A schematic of experimental setup of light scattering is shown in Fig.2-24. The same experimental setup for fluorescence-imaging except detection part was used. The scattered light was projected on a thin sheet of white paper placed above the sample at a specific distance ranging from 28 to 60 mm, and the projected scattering image was captured with a cooled CCD camera (iKon, Andor Technology, -50°C, 512 x 512 pixels^2). The delay time between the near IR pulse and the green pulse was electrically controlled by a digital delay generator (Stanford Research System DG535).

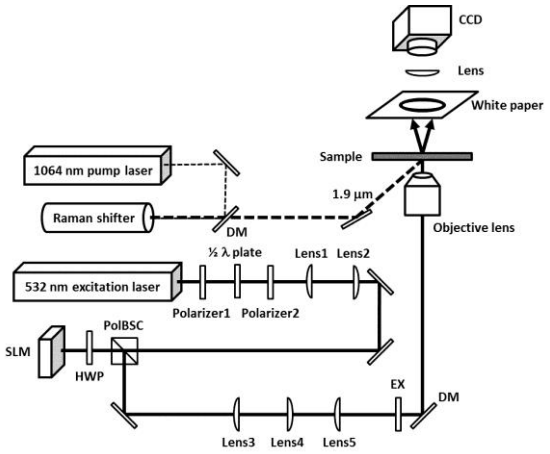

Fig.2-24 Scheme of experiment setup for light scattering.

All scattering images were analyzed using MATLAB (Mathworks, Inc.). At least 20 scattering images at each delay time were averaged. Power spectra were calculated as the radial distribution of the scattering light intensity. Our system covered the wavenumber Q ($Q = (4\pi n/\lambda)\sin(\theta/2)$) range from 0.2 to 13 μm^{-1}, where n, λ, and θ are the sample refractive index, wavelength of the probe beam (532 nm), and scattering angle, respectively. To confirm the correspondence between the power spectrum and size in real space, calibration measurements were performed with 0.5-, 1-, and 3-μm-diameter polystyrene beads (Polyscience, Inc., Polybeads Red Microspheres) that formed periodic structures on a cover glass (Matsunami Glass Ind., LTD, thickness 0.12–0.17 mm). The preparation for the calibration samples was mentioned above.

References

[1] H. L. Cox and L. H. Cretcher, *J. Am. Chem. Soc.*, **1926**, *48*, 451.

[2] A. W. Francis, *Critical Solution Temperatures*, Advances in Chemistry Series 31, American Chemical Society, Washington D.C, **1961**.

[3] F. Mallamace, N. Micali, C. Vasi, G. D'Arrigo, *Il Nuovo Cimento D*, **1992**, *14*, 333.

[4] A. Takamizawa, Doctoral Thesis, **2005**.

[5] N. Ito, T. Fujiyama, Y. Udagawa, *Bull. Chem. Soc. Jpn.*, **1983**, *56*, 379.

[6] G. Poppe, *Bull. Soc. Chem. Belg.*, **1935**, *44*, 640.

[7] V. Balevicius, H. Fuess, *Phys. Chem. Chem. Phys.*, **1999**, *1*, 1507.

[8] A. Takamizawa, S. Kajimoto, J. Hobley, H. Fukumura, Q. Tran-Cong, *Phys. Rev. E*, **2003**, *68*, 020501.

[9] F. Kohler and O. K. Rice, *J. Chem. Phys.*, **1957**, *26*, 1614.

[10] J. C. Hulteen, R. P. Van Duyne, *J. Vac. Sci. Technol. A*, **1995**, *13*, 1553.

[11] J. Y. Shiu, C. W. Kuo, P. Chen, Chung. Y. Mou, *Chem. Mater.*, **2004**, 16, 561.

[12] T. G. Dewey, D. H. Turner, *Advances in Molecular Relaxation and Interaction Processes*, **1978**, *13*, 331.

[13] K. Yamamoto, Y. Mizutani, T. Kitagawa, *Appl. Spec.*, **2000**, *54*, 1591.

[14] R. Yamamoto, T. Ebata, N. Mikami, *J. Chem. Phys.*, **2001**, *114*, 7866.

[15] R. Yamamoto, T. Ebata, N. Mikami, *Eur. Phys. J. D,* **2002**, *20*, 403.

[16] Home page of Hamamatsu Photonics.

[17] O. Krichevsky, G. Bonnet, *Rep.Prog. Phys.*, **2002**, *65*, 251.

[18] D. S. Banks, C. Fradin, *Biophysical J.*, **2005**, *89*, 2960.

[19] K. H. Shim, B. G. Kim, *J. Korean Phys. Soc.*, **2006**, *49*, S647.

[20] M. G. L. Gustafsson, D. A. Agard, J. W. Sedat, *Proceedings of SPIE*, **2000**, *3919*, 141.

[21] M. G. L. Gustafsson, L. Shao, P. M. Carlton, C. J. R. Wang, I. N. Golubovskaya, W. Z. Cande, D. A. Agard, J. W. Sedat, *Biophys. J.*, **2008**, *94*, 4957.

Chapter 3 Solution structure of binary mixture below the LCST

3-1 Preface

For investigation of an influence of complex solution structure on solute diffusion in water/2BE mixture, FCS was employed. The amphiphilic dye ATTO532, and BPDI were used as solutes. All measurements were carried out at room temperature far below the LCST (Fig.3-1). As a reference, FCS experiments were also carried out with the hydrophobic dye in water/MeOH mixtures, whereby signs of phase separation or complex solution structures were not observed in the mixture. In this chapter, details of experimental results are described.

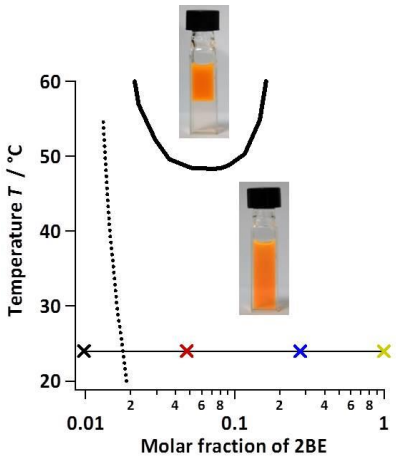

Fig.3-1 Phase diagram of water/2BE mixture. Crosses, and thick solid and dot lines express FCS measurement points, coexistent curve, and critical micelle concentrations at various temperatures. Ref.1 Upper and lower pictures are the water/2BE mixture with BPDI 10-5 M after and before phase separation, respectively.

3-2 Diffusion times

Diffusion of ATTO532 and BPDI mixtures in water/2BE mixtures of varying molar fractions of 2BE were studied by FCS using a standard confocal microscope. The fluorophores were dissolved individually in the water/2BE mixtures and their diffusion times were estimated from the measured fluorescence intensity correlation curves by applying a model consisting of a triplet and a single diffusion component (eq.3-2) as described in chapter 3. FCS measurements were carried out at room temperature, i.e. about 25°C below LCST, for different molar fractions of water/2BE mixtures as exemplified in Fig.3-1 using a calibrated confocal setup.

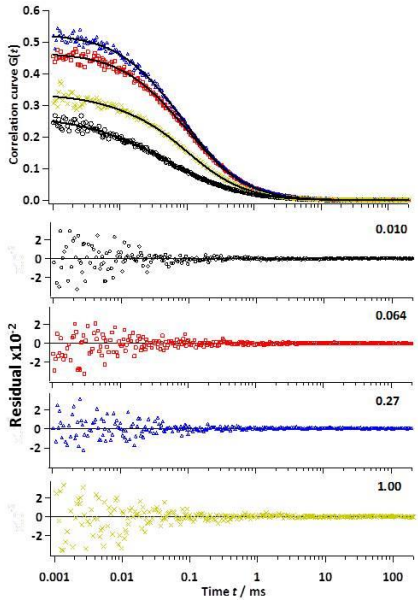

Fig.3-2 Correlation curves of BPDI in water/2BE mixtures. Fitting analyses were carried out with the one component diffusion plus triplet model, and the residuals of these fits express the quality of these fits. Closed circles, red squares, blue triangles, and green crosses express the results with solution having the 2BE molar fraction of 0.010, 0.064, 0.27, and 1.00, respectively.

The diffusion times t_d^i of the different fluorophores *i* obtained at various 2BE molar fractions are plotted in Fig.3-3. They reflect the average time a fluorescent dye stays in the confocal volume. In the experiments with the amphiphilic ATTO532, the diffusion times t_d^{ATTO} (Fig.3-3, open circles) increased with increasing 2BE molar fraction, and showed a local maximum at around 2BE molar fraction 0.30. The increase can be readily explained by a change in viscosity η in accordance with the Stokes-Einstein equation (1)

$$D = \frac{k_B T}{6\pi\eta r_{hyd}} \tag{1}$$

as the diffusion time t_d depends on the diffusion coefficient *D* which is a function of the absolute temperature *T* and the hydrodynamic radius r_{hyd} of the diffusing molecule; k_B is Boltzmann's constant. This expected finding indicates that the viscosity of the mixtures, plotted in Fig.3-4 as closed circles, mainly influence the diffusion of ATTO532. On the other hand, the diffusion times t_d^{BPDI} of BPDI (Fig.3-3, closed circles) show a different trend as compared to ATTO532. For low 2BE molar fractions it initially shows a rapid rise reaching a local maximum at around 0.10, after which it gradually decreases again. Since the macroscopic viscosities of the mixtures were not affected by the addition of two dyes, only the diffusion of the hydrophobic dye is apparently slowed down at around a 2BE molar fraction close to the critical composition 0.052 with respect to 2BE molar fraction, which is irrespective of the macroscopic viscosity.

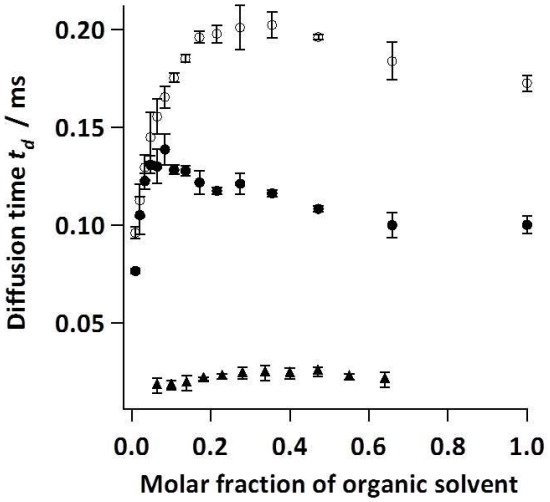

Fig.3-3 Diffusion times of BPDI and ATTO 532 NHS ester in water/2BE mixtures (closed and open circles, respectively) and BPDI in water/MeOH mixtures (closed triangles) obtained from correlation functions as functions of the molar fraction of organic solvents.

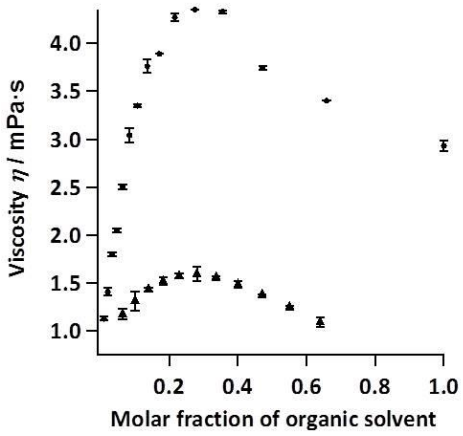

Fig.3-4 Viscosities of water and organic solvent mixtures. Closed circles and triangles express water/2BE mixtures and water/MeOH mixtures, respectively.

3-3 Artifacts for diffusion times

Next, the hydrodynamic radii of the fluorescent probes were determined to learn more about the actual diffusing species. It is noteworthy that for data analyses the well-described artifacts in FCS were also accounted for.[2,3] Since the diffusion time reflects the time the fluorophore stays in the effective confocal volume, first the changes of the effective confocal volume with an increase of the 2BE molar fraction were examined. The average number of molecules ⟨*N*⟩ in the effective

confocal volume V_{eff} was obtained by fitting the respective models to the correlation curves that were determined at various molar fractions of 2BE. Then, the effective confocal volume was calculated from the estimated average number of molecules ⟨*N*⟩, the known dye concentration *c* (10 nM), and Avogadro's number N_A by using equation (2).

$$V_{eff} = \frac{\langle \mathrm{N} \rangle}{\mathrm{c}N_A} \tag{2}$$

The determined effective confocal volumes V_{eff} for BPDI and ATTO 532 are plotted as functions of 2BE molar fraction in Fig.3-5 (a) as closed and open circles, respectively, showing a clear decrease as the 2BE molar fraction increases and correlation with each fluorescent dye. This means that the decrease was not due to fluorescent dye but experimental setup. And this behavior can be explained by a mismatch between the nominal and the real cover slide thickness.[3] Fig.3-5 (b) shows the refractive indices of the mixtures measured with a conventional Abbe refractometer (closed circles) as a function of molar fraction of 2BE. According to the model (Fig.3-6) the cover slide thickness is by ca. 20 µm smaller than the value for which the objective is corrected for. This mismatch is then mostly compensated when measuring in a solvent with refractive index of about 1.39, i.e. a molar fraction of 2BE of ca. 0.2. Clearly, the effective confocal volume shows a strong dependence on the refractive index that must be taken into account in order to furnish reliable data from our FCS experiments.

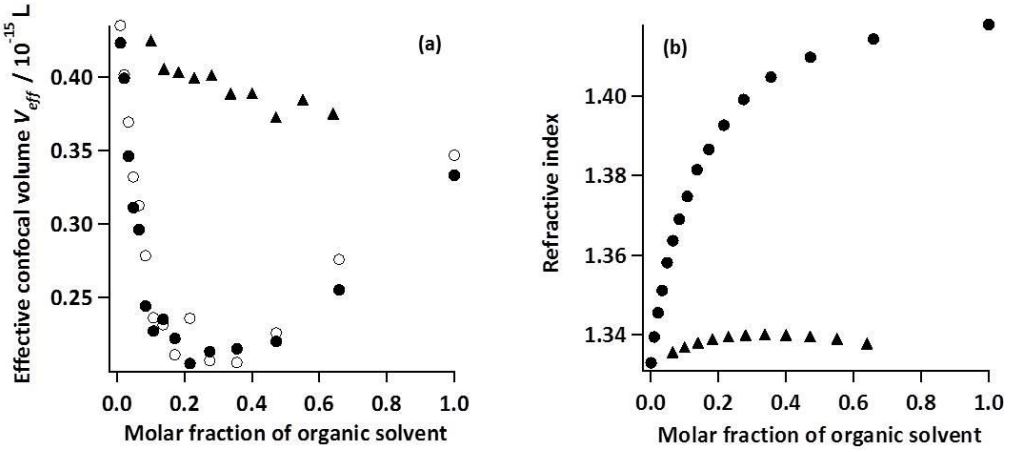

Fig.3-5 (a) Effective confocal volumes of the FCS system. Closed and open circles, and closed triangles express the results of BPDI, ATTO 532 NHS ester in water/2BE mixtures, and BPDI in water/MeOH mixtures, respectively. (b) Refractive indices of water and organic solvent mixtures. Closed circles and triangles express water/2BE mixtures and water/MeOH mixtures, respectively.

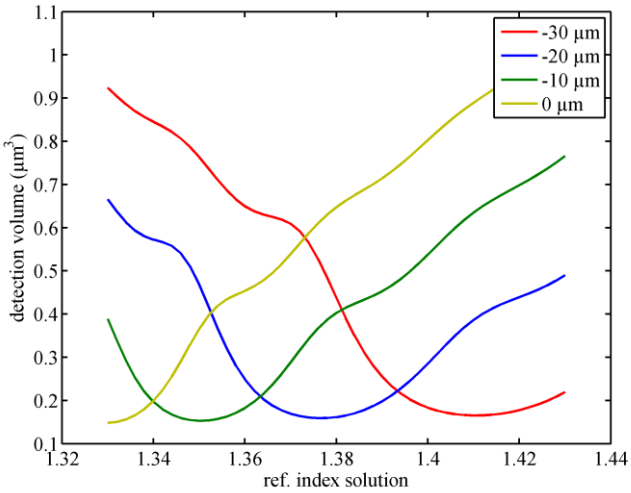

Fig.3-6 Expected focal volume calculated using the wave-optical model described in Ref.3 for a cover-slide thickness mismatch of 0, -10, -20, and -30 µm. In the model, we assumed that the back aperture of the objective was fully overfilled (diffraction-limited focus) by the excitation laser of 532 nm wavelength, and that the fluorescence emission occurs around 570 nm. The size of the confocal pinhole was set to 25 µm diameter.

3-4 Changes of hydrodynamic radius

In order to compensate for the viscosity effects and the changes in the effective confocal volume, the obtained diffusion time t_d was divided by both the viscosity η and the effective confocal volume to the power of two thirds $V_{eff}^{2/3}$. From equation (1) and equation (3), expressing a relationship between t_d and D,

$$t_d = \frac{{r_0}^2}{4D} \tag{3}$$

the diffusion time can thus be represented as

$$t_d \propto \frac{3\pi\eta {V_{eff}}^{\frac{2}{3}}}{2k_B T} r_{hyd} \tag{4}$$

Therefore, the compensated diffusion time t_d' can be represented by

$${t_d}' \propto \frac{3\pi}{2k_B T} r_{hyd} \tag{5}$$

The compensated values t_d' were plotted as functions of 2BE molar fraction in Fig.3-7. Assuming the temperature in equation (5) is constant, t_d' values are directly proportional to the hydrodynamic radii of fluorescent dyes, therefore reflecting its changes due to solvent/solute interactions. Strikingly, the apparent hydrodynamic radius of BPDI still shows a marked peak around a 2BE molar fraction of 0.05 (Fig.3-7 (a), left axis) while the hydrodynamic radius of ATTO532 remains almost constant irrespective of the varying molar fractions of 2BE (Fig.3-7 (b)). Interestingly, the peak

region observed for BPDI clearly overlaps with the coexistence curve of the water/2BE mixture as shown in Fig.3-7 (a) (right axis). At the maximum, the apparent hydrodynamic radius of BPDI nearly doubled.

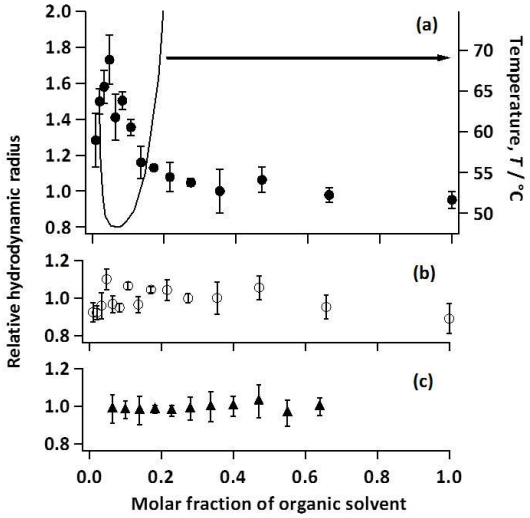

Fig.3-7 Calculated apparent hydrodynamic radii of (a) BPDI and (b) ATTO 532 NHS ester in water/2BE mixtures as functions of molar fraction of 2BE. Coexistent curve of water/2BE mixture was plotted together in (a) as a solid line (right axis). (c) Calculated apparent hydrodynamic radii of BPDI in water/MeOH mixtures as a function of molar fraction of MeOH.

For comparison, and to see if this behavior was specific for the solutes or the solvents, the diffusion times of BPDI in water/MeOH mixtures were measured at various molar fractions of MeOH (Fig.3-3 closed triangle). The solubility of BPDI in MeOH is comparable to the solubility in 2BE. The apparent hydrodynamic radii of BPDI in the water/MeOH mixtures plotted as a function of molar fraction of MeOH in Fig.3-7 (c) were determined as described before. In contrast to the previous experiments, the radii of BPDI in water/MeOH mixtures did not show any dependency on the MeOH molar fraction.

3-5 Interaction between dyes and solution structures

The finding that, in opposition to ATTO532, the diffusion of BPDI is impaired in water/2BE mixtures close to their critical composition, while it remains largely unchanged in water/MeOH mixtures, points towards a specific interaction between the solute and solvent depending on the solvent state. Based on previous experimental findings on transient solvent structure dynamics, this behavior can be explained by interaction between the dye and transient structures occurring in water/2BE mixtures.[4-9] It is intuitive to understand that such reversibly formed dynamic micellar

structures will coexist with the mixed bulk solution and thereby form transient barriers between different regions. Since ATTO532 is amphiphilic, it is conceivable that the dye would be solvated not only by water molecules but almost equally by 2BE molecules; the partitioning of both fluorophores under phase separation conditions (at ~55°C) was measured based their extinction coefficients and found ATTO532 partitions to about 60% into the organic phase. As there are no indication for a second component or for anomalous diffusion, and because the slowed diffusion goes with the viscosity of the solvent, it is assumed that the diffusion of ATTO532 is principally controlled by the bulk properties of the solvent state rather than by interaction with local dynamic states, like transiently formed micellar aggregates. BPDI, on the other hand, is highly hydrophobic; it was found that BDPI partitions to 96% into the lipophilic organic layer. Thus, it is conceivable that these molecules are selectively solvated by 2BE molecules. Such a solvation shell can act as a nucleus for 2BE micellar aggregation and then grow into a solvate shell leading to the increasing hydrodynamic radius observed in our experiments. Notably, the growth of the hydrodynamic radius of BPDI was not observed in the water/MeOH mixtures. Although it is reported that water/MeOH mixtures also have local solution structures, their main species at a MeOH molar fraction $\chi < 0.3$ is a tetrahedral-like water cluster different from micellar aggregates in water/2BE.[10] In this case, the interaction of the hydrophobic BPDI molecules with the water containing solution structures is less pronounced and less dissimilar from bulk solution structures.

3-6 Stabilization of solution structure by fluorescent dye

Moreover, it is probable that transient micellar aggregates are stabilized by BDPI. It is well established that micellar aggregates form and dissolve on the nanosecond time scale.[9] If these short-lived micellar structures impair the diffusion of solutes, both dyes would show a slowed diffusion rate as both partition the organic phase as mentioned before. However, only BDPI shows a marked change in its diffusion (Fig.3-7 (a)) while ATTO532 remains almost unchanged (Fig.3-7 (b)) after correction for changes in viscosity and refractive index. Consequently, BDPI conceivably influences the solvent structure by also stabilizing micellar structures that provide favorable solvent shells for the hydrophobic dye (Fig.3-8). However, it is possible that these lifetimes are still beyond the temporal resolution of FCS since no second component was observed. Similar observations have been reported on frozen structures, which affect solute diffusion.[11,12] Thus it was concluded that the influence of BPDI on micellar aggregates in water/2BE mixtures is due to an increase in their lifetime, which consequently leads to marked effects in translational diffusion properties.

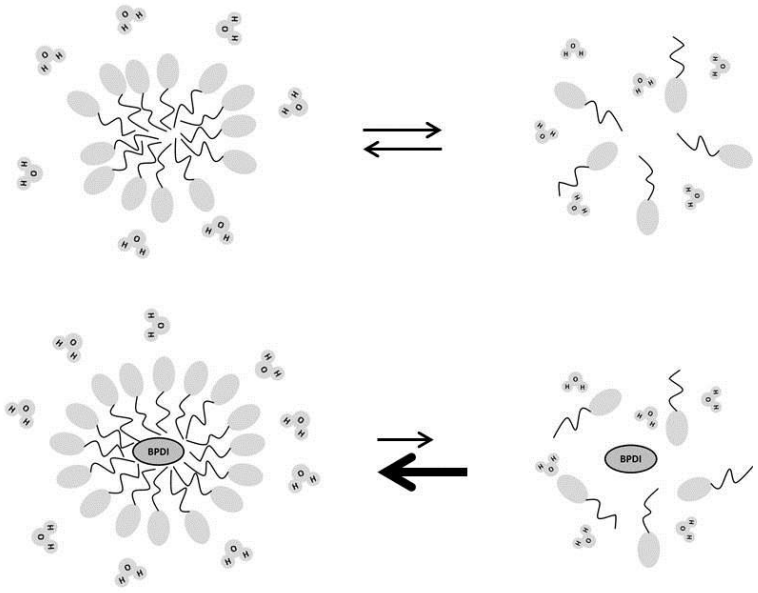

Fig.3-8 A schematic model of micellar aggregate formation and the preferential interaction between the aggregate and BPDI.

Assuming the discussed facilitated formation and stabilization of micellar aggregates by BPDI, the observed changes of the hydrodynamic radius of BPDI (Fig.3-7 (a)) can be interpreted as a change in the size of these aggregates. According to Nillson *et al.*, micellar growth at low surfactant concentrations can be explained by more frequent coalescences with neighboring micellar structures when surfactant concentrations and thus micellar densities increase.[13] On the other hand, shrinkage of the micellar size observed for higher surfactant molar fractions are then explained by more frequent and intense interactions between neighboring micelles as their density increases. At some juncture, micelles will no longer be identifiable because of rapid monomer exchange among them leading to percolation-like structures as observed by Mallamace *et al.* by using depolarized Rayleigh-wing light scattering as mentioned in introduction part (Chapter 1).[14] According to these models, BDPI will then experience less water-like barriers, and finally exhibit free diffusion through a continuous 2BE phase with an apparently smaller hydrodynamic radius. Here, one might suggest that percolation-like structures could lead to restrictive diffusions that would show up as anomalous diffusions. However, these anomalies could not be observed in our data sets, which were consistently fitted to a simple one-component model. This leads us to the conclusion that, even though our experiments were carried out around 25°C below LCST, highly dynamic solvent structures that were likely facilitated by appropriate solute molecules (i.e. the hydrophopic BDPI) were observed. This opposes the widely accepted notion of homogenous solvent mixtures under such conditions.

3-7 Conclusion

In summary, by FCS analysis, non-classical diffusion of the hydrophobic dye, BPDI, in water/2BE mixtures was observed, i.e. the translational diffusion of the dye was unusually slow when the water/2BE mixture was close to its critical composition but still well below its LCST. Although the apparent hydrodynamic radius of the amphiphilic dye ATTO532 remained largely unchanged with 2BE concentration, the apparent radius of BPDI almost doubled close to critical composition. In contrast, radii remained almost unaffected in water/MeOH mixtures. These observations were explained by virtue of the different affinities of the fluorescent dyes for less or more polar solvents and thus by the different interactions with local solution structures that are transiently formed in water/2BE mixtures but not in water/MeOH. Moreover, our data suggest that the presence of the hydrophobic dye BDPI stabilizes otherwise unstable 2BE micellar aggregates by at least ~10^{-4} s. In this perspective, the observed increase in the hydrodynamic radius of BPDI can be explained by a change in the size of micellar aggregates that form around BDPI, which change to bulk solvent shell structures at higher 2BE concentrations. From our experiments, it was concluded that translational diffusion of the solvated-dye depends on both the properties of the solutes and the solvent. Thus, it was found that different solutes can experience different environments even within the same solvent mixtures and even far below LCST.

References

[1] M. D'Angelo, G. Onori, A. Santucci, *Chem. Phys. Lett.*, **1994**, *220*, 59.

[2] J. Enderlein, I. Gregor, D. Patra, J. Fitter, *Curr. Pharm. Biotechnol.*, **2004**, *5*, 155.

[3] J. Enderlein, I. Gregor, D. Patra, T. Dertinger, U. B. Kaupp, *ChemPhysChem*, **2005**, *6*, 2324.

[4] N. Ito, T. Fujiyama, Y. Udagawa, *Bull. Chem. Soc. Jpn.*, **1983**, *56*, 379.

[5] T. Kato, *J. Phys. Chem.*, **1985**, *59*, 5750.

[6] H. Hayashi, Y. Udagawa, *Bull. Chem. Soc. Jpn.*, **1992**, *65*, 600.

[7] G. D'Arrigo, R. Giordano, J. Teixeira, *J. Mol. Struct.*, **1997**, *404*, 319.

[8] T. Telgmann, U. Kaatze, *Langmuir*, **2002**, *18*, 3068.

[9] K. Yoshida, T. Yamaguchi, T. Otomo, M. Nagao, H. Seto, T. Takeda, *J. Mol. Liq.*, **2005**, *119*, 125.

[10] T. Takamuku, T. Yamaguchi, M. Asato, M. Matsumoto, N. Nishi, *Z. Naturforsch*, **2000**, *55 a*, 513.

[11] A. Masuda, K. Ushida, T. Okamoto, *Phys. Rev. E*, **2005**, *72*, 060101.

[12] A. Masuda, K. Ushida, T. Okamoto, *J. Photochem. Photobio. A: Chemistry*, **2006**, *183*, 304.

[13] P. Nilsson, H. Wennerstrom, B. Lindman, *J. Phys. Chem.*, **1983**, *87*, 1377.

[14] F. Mallamace, D. Lombardo, G. Onori, A. Santucci, *Phys. Rev. E*, **1995**, *51*, 2349.

Chapter 4 Mesoscopic structural changes in laser-induced phase separation

4-1 Introduction

In this chapter, results of studies on dynamics of laser-induced phase separation (LIPS) are described. Three methods have been used frequently for investigation of dynamics of phase separation. The first was shadowgraph-imaging, which have been used in our lab.[1-3] The second was fluorescence-imaging. Especially confocal fluorescence microscopy is frequently used for investigation of phase separation in mainly polymer blend system.[4-6] To our best knowledge, the method has never been applied to study in a binary liquid mixture system because the temporal resolution of the method is not so high enough that visualize phases in a solution. The last was a light scattering technique which is also frequently used for investigation of phase separation in not only polymer blend systems but also binary liquid mixtures.[7-10] Despite this, it is not understood well what is observed in shadowgraph-imaging and whether these methods are comparable or not. Therefore, first of all, a comparison with these three experimental methods was carried out. Results of the comparison are described in section 4-2. Secondly, to overcome the diffraction limit of a microscope, an attempt was made to extend the temporal resolutions of structured illumination microscopy (SIM) [11-13] to the nanosecond time scale. As results, considerable potential of nanosecond SIM for the detection of a periodic structure with nanosecond temporal resolution is demonstrated in section 4-3. In this section, characterization study on fluorescent dyes I used in nanosecond SIM is also described. This is important not only from viewpoint of application, but also to understand dynamic changes of solvent environment during LIPS. For earlier delay time region, light scattering was employed to investigate dynamics of LIPS. Results of the study are described in section 4-4. Finally, based on our observations and the previous time-resolved Raman scattering studies, a new view of the early stage of spinodal decomposition (SD) process is proposed in section 4-5.

4-2 Comparison of methods

Fig.4-1 shows obtained images with three methods; shadowgraph-imaging, fluorescence-imaging, and light scattering, at delay time of 100 μs. Water/2-butoxyethanol (2BE) mixture having the critical composition was used. As a sample cell, two slide glasses were used to make sample thickness thin as described in chapter 3. The sample thickness was estimated less than 10 μm. The Initial temperature of the sample solution was kept at 24°C. The intensity of near IR pulse was 1.07 J/pulse•cm^2 corresponding to the magnitude of T-jump 30.3°C and quench depth 5°. Fig.4-1 (a) is a shadowgraph image. In the image, warm-like bright regions and dark regions were observed. Fig.4-1 (b) is a fluorescence image. In the image, continuous bright regions were observed. These regions can be regarded as 2BE-rich phases because the fluorescent dye, BPDI, which I used, is very hydrophobic compound and show large difference of fluorescent efficiency

between water- and 2BE-rich phases. Insets in Fig.4-1 (a) and (b) are FFT image of each image. A ring pattern can be observed in each FFT image, which is the hallmark of the SD process.[7] Fig.4-1 (c) is a scattering image. A ring pattern was also observed in the scattering image.

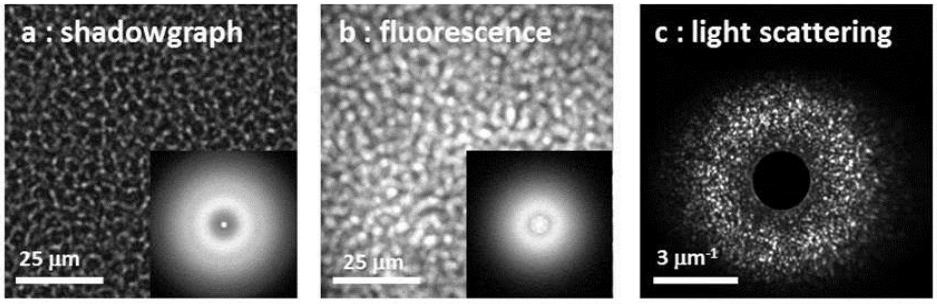

Fig.4-1 Obtained images at delay time of 100 μs with three different methods. (a) Shadowgraph-imaging. Inset is FFT image. (b) Fluorescence-imaging. Inset is FFT image. (c) Light scattering.

A circulation system and a 100 μm thickness flow cell were also used to record these images. Fig.4-2 shows a shadowgraph image and a fluorescence image at delay time of 100 μs. In the case, shadowgraph- and fluorescence-imaging were available and allowed us to obtain the ring pattern in FFT images of these images (see Fig.4-2 insets). But the qualities of these images were not good. Alternatively, a scattering image with a clear ring pattern was not obtained with the 100 μm flow cell. Fig.4-3 shows two pictures of light scattering images. Left is with the 100 μm flow cell and right is with thin sample. This may be due to temperature graduation along the near IR beam direction. As mentioned in Chapter 3, the optical absorbance of the 100-μm-thick mixture at 1.88 μm was 0.47, indicating that the transmittance of the pump pulse was less than 40% and that the magnitude of the T-jump at the back surface was less than half of that at the front surface. Therefore it is conceivable that phase separation with various quenching depth was captured in these images.

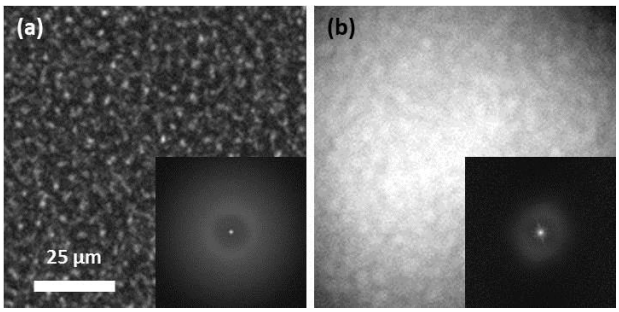

Fig.4-2 Obtained images with 100 μm thickness flow cell at delay time of 100 μs; with shadowgraph-imaging (a) and fluorescence-imaging (b). Insets are FFT images.

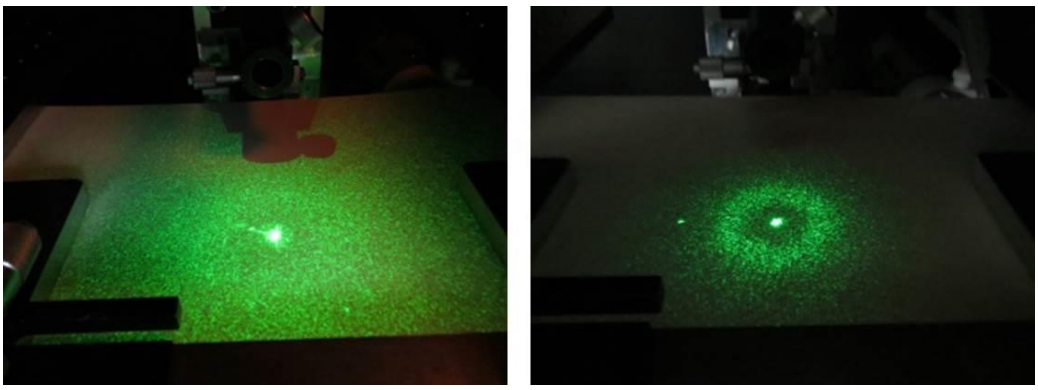

Fig.4-3 Pictures of light scattering. Left : 100 μm thickness flow cell. Right : Thin sample (thickness ~ 10 μm).

Fig.4-4 shows power spectra obtained with these three methods at various delay time. In each power spectrum of fluorescence-imaging and light scattering, only a single peak was observed, indicating that a characteristic length of phase separating media represents the phase domain size at each delay time. Fig.4-4 shows that the peak position shifted toward lower wavenumber with time. Characteristic lengths were determined from the peak positions in these power spectra. By assuming that the sizes of the water-rich and 2BE-rich phases are the same (critical quench), we defined the phase domain size $L(t)$ as half of the characteristic length. The determined domain sizes are plotted as functions of delay time in Fig.4-5. Closed circles and open triangles present results with fluorescence-imaging and light scattering, respectively. The change in $L(t)$ with time followed the power law $L(t) \sim t^{\alpha}$ as predicted by the theoretical model based on scaling concepts in the late stage of SD.[10,14] According to the figure, fluorescence-imaging and light scattering show good agreement with each other; the value of the exponent α was determined as 0.61 and 0.64, respectively. Mallamace *et al.* reported that the late stage of SD in water/2BE mixtures with shallow quenches follows the power law $L(t) \sim t^{1/3}$.[10] This discrepancy can be explained by the temperature dependence of the viscosity of the mixture; at critical composition, viscosity increases rapidly as a temperature approaches the LCST.[15] Thus, for phase separation with a shallow quench, viscosity can be high and the hydrodynamic effect is minor. In this case, the exponent is expected to be small. Alternatively, in the case of a deep quench, it is conceivable that the viscosity is small and the hydrodynamic effect is dominant, resulting in a high exponent value. Using a lattice Boltzmann simulation, Gonzalez-Segredo *et al.* demonstrated that the exponent increases from 0.54 to 0.71 with an increase in the system's Reynolds number.[16]

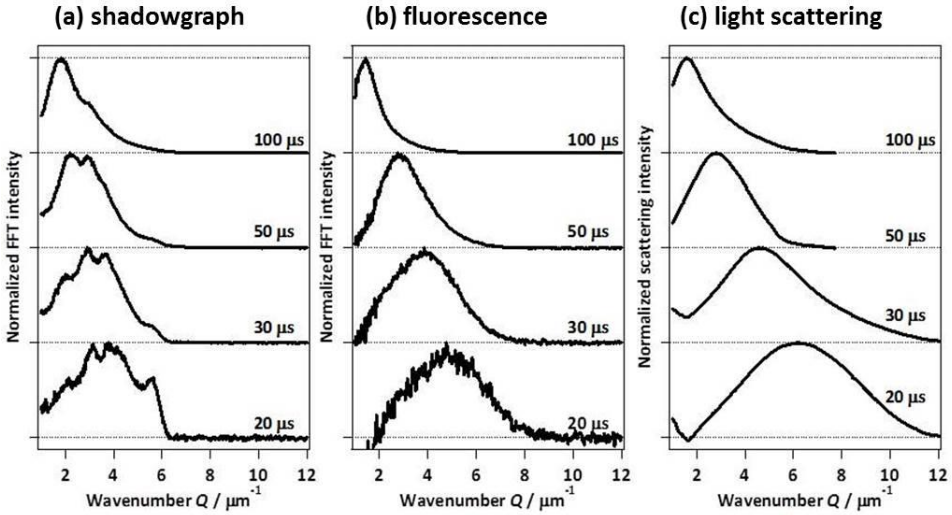

Fig.4-4 Obtained power spectra at various delay times with three different methods. Sample thickness was less than 10 μm. (a) Shadowgraph-imaging. (b) Fluorescence-imaging. (c) Light scattering.

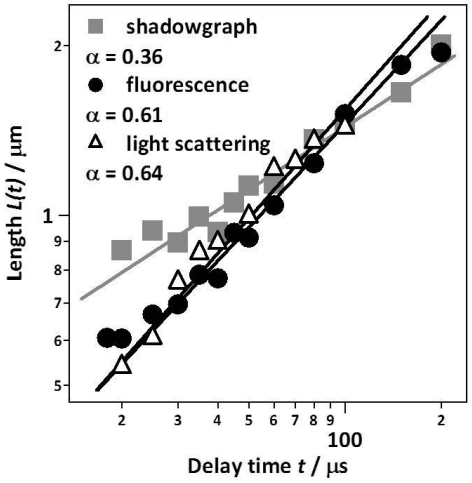

Fig.4-5 Domain size obtained with different methods plotted as a function of delay time. Gray squares, closed circles, and open triangles present results of shadowgraph-, fluorescence-imaging, and light scattering, respectively. Solid lines show fitting curves.

On the other hand, in the power spectra of shadowgraph imaging, several peaks were observed. Note that, when the thickness of sample was large enough, these multiple peak behavior was not observed (see Fig.4-6). Since it is difficult to assign each peak, the characteristic lengths were determined by assumption these peaks as single peak fitting with single Gaussian function. The determined characteristic lengths were plotted in Fig.4-5 (gray squares). Obviously, result of shadowgraph imaging is different from the other methods; the value of the exponent α was

determined as 0.36.

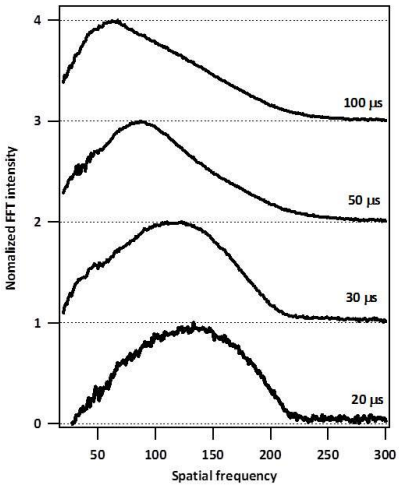

Fig.4-6 Power spectra obtained at various delay times with shadowgraph-imaging. Sample cell is a 100 μm thickness flow cell.

To understand what results in the multiple peaks in power spectra of shadowgraph images, some shadowgraph images at various delay times are shown in Fig.4-7. As mentioned before, worm-like bright region and dark region were observed in these images. At early delay time, the worm-like bright region was predominant. However the dark region grew and became predominant with time. Fig.4-8 shows line profiles of these images. From the line profiles, it was found that width of the worm-like bright region was almost constant at approximately 1 μm. It is conceivable that width of interface between water- and 2BE-rich phases is almost constant and the ratio of interface to volume of two phases decreases with time in the late stage of SD. Therefore, the worm-like bright region can be regarded as the interface. Alternatively the dark region can be regarded as either water- and 2BE-rich phases. Fig.4-9 shows conceptual sketches of shadowgraph- and fluorescence-imaging. Namely, in shadowgraph-imaging, the interface was observed. On the other hand, in fluorescence-imaging, 2BE-rich phase itself is observed.

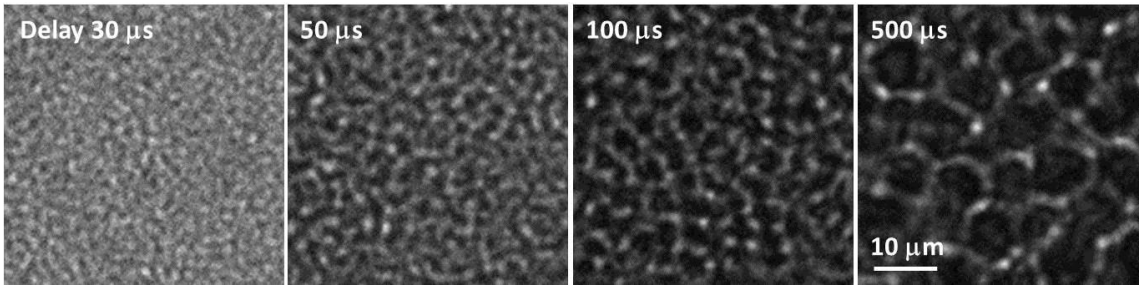

Fig.4-7 Shadowgraph images at various delay time after T-jump.

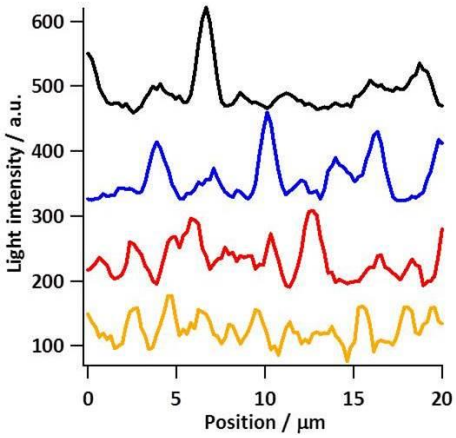

Fig.4-8 Line profiles for shadowgraph images shown in Fig.4-8. Black, blue, red, and green lines present 500, 100, 50, and 30 μs delay time.

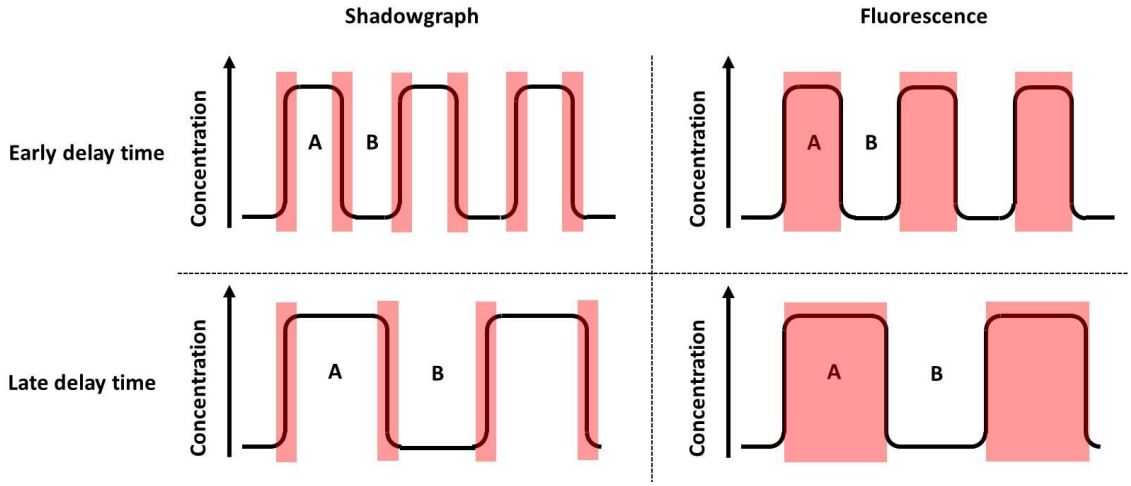

Fig.4-9 Conceptual sketches of shadowgraph- and fluorescence-imaging.

It is conceivable that obtained power spectra contained form factor $F(Q)$ and structure factor $S(Q)$. The $F(Q)$ proceeds from form of phase itself, and the $S(Q)$ proceeds from spatial arrangement of phases. $S(Q)$ for shadowgraph- and fluorescence-imaging should be the same. However $F(Q)$ for these methods are expected to be different from each other, because what are observed in these methods is different as discussed above. Therefore the $F(Q)$ for shadowgraph-imaging reflects form of the interface, and the $F(Q)$ for fluorescence-imaging reflects form of phase itself (Fig.4-10). The difference may lead to the difference in power spectra.

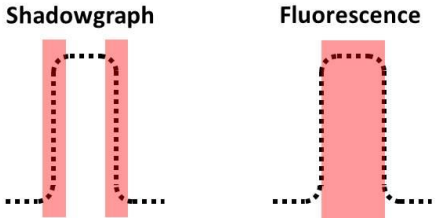

Fig.4-10 Conceptual sketches of Form Factor for shadowgraph- and fluorescence-imaging.

To extract the $S(Q)$ from power spectra of shadowgraph-imaging, multi-peak fitting with several Gaussian functions was applied to them. Fig.4-11 (a) shows an example of the fitting results. Three or four Gaussian functions were needed to fit well. From these Gaussian peaks, domain sizes were determined at each delay times. Only one domain size at each delay time was selected and plotted in Fig.4-11 (b). Selected domain sizes could be fitted with a power law t^{α} well. The determined exponent α was 0.58 and was close to the results of fluorescence-imaging and light scattering. To be honest, it should be note that this multi-peak analysis contains large arbitrariness. It might be possible to extract only structure information, however it seems to be very difficult to analyze.

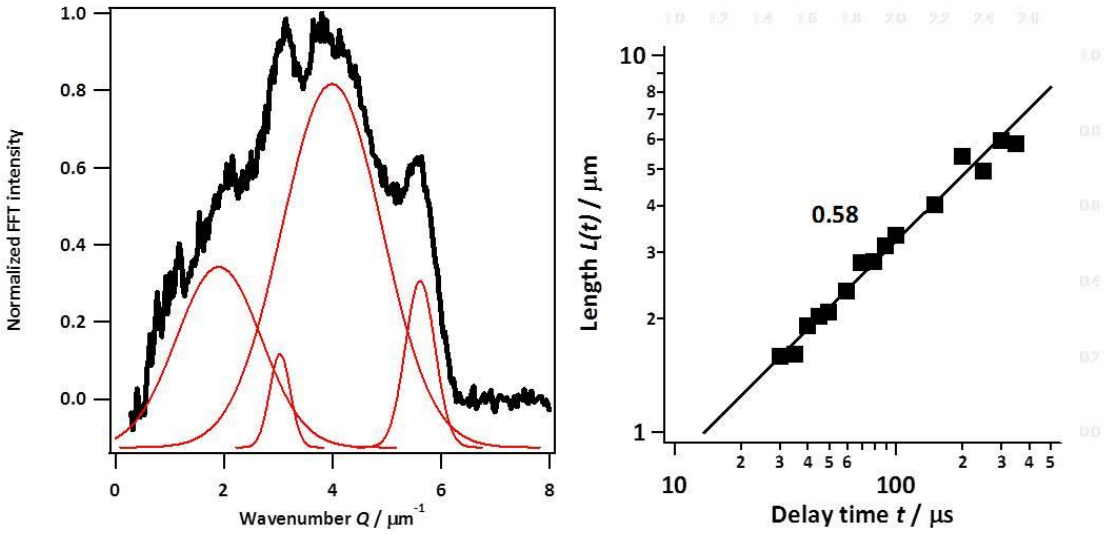

Fig.4-11 (a) Example of multi-peak fitting with several Gaussian functions for a power spectrum of shadowgraph image. (b) Selected domain sizes plotted as a function of delay time.

4-3 Nanosecond structure illumination microscopy

4-3-1 Evaluation

The validity of nanosecond SIM was evaluated by using a periodic structure of Latex beads on cover glass.[17,18] Diameters of the polystyrene beads were 1.00 and 3.11 μm. Fluorescence

images are shown in Fig.4-12 (a-d). In the case of 3.1 μm Latex beads, one can see a hexagonal periodic structure in Fig.4-12 (a). 2D FFT image is shown in Fig.4-12 (e). A white arrow and dotted hexagon are inserted into the 2D FFT image as an eye guide. The image shows a bright center spot and six spots at the corner of the inserted hexagon. The distances of six spots from the center spot correspond to a period of the hexagonal structure captured in Fig.4-12 (a). When the periodic structure is illuminated with structured illumination (SI), the center spot shifted symmetrically toward high frequency and pointed with white arrows. Additionally, the symmetric shift of the six spots was observed. In the case of 1.0 μm Latex beads, a clear periodic structure was not observed (Fig.4-12 (c)), and any specific pattern was also not observed in 2D FFT image (Fig.4-12 (g)) because 1.0 μm is below the diffraction limit of our microscope system. However, when SI was used, one can see the edge of ring patterns which seem to be shifted with SI in 2D FFT image (Fig.4-12 (h)). To emphasize the shifted ring patterns, the 2D FFT image was divided with 2D FFT of uniform illumination (UI) and shown in Fig.4-12 (i). From the divided 2D FFT image, SIM power spectrum was calculated as a radial distribution with central point at shifted center spots, and shown in Fig.4-12 (j). Obviously a peak was observed at Q = 6.5 μm^{-1} corresponding to 1.0 μm. From the results, it is verified that the nano-second SIM technique possesses the super-resolution ability. The spatial resolution of nano second SIM was confirmed to be at worst 1 μm.

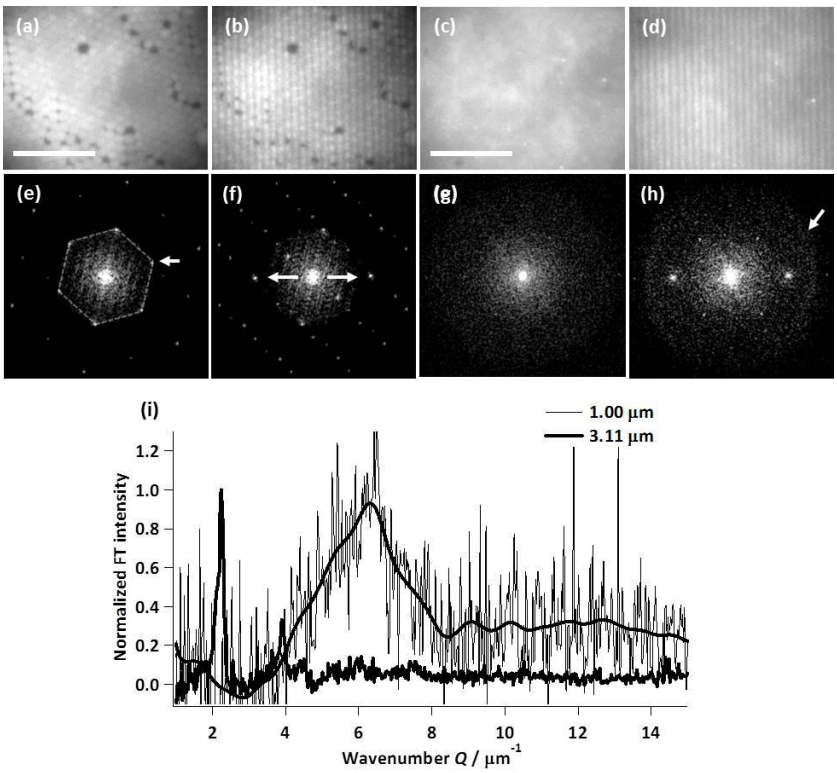

Fig.4-12 (a-d) Fluorescence images with UI (a and c) and SI (b and d). (e-h) 2D FFT images upper images, respectively. (i) SIM power spectra for 1.00 mm (thin line) and 3.11 mm (Thick line).

4-3-2 Demonstration

In Fig.4-13, some fluorescence images taken with UI (upper) and SI (lower) at various delay time are shown. These insets are 2D FFT images of each image. In these 2D FFT images taken with UI, a center spot and a ring pattern corresponding to characteristic lengths of phases were observed. Alternatively, in these 2D FFT images taken with SI, not only the center spot and center ring pattern but also symmetrically shifted spots and ring patterns due to SI were observed.

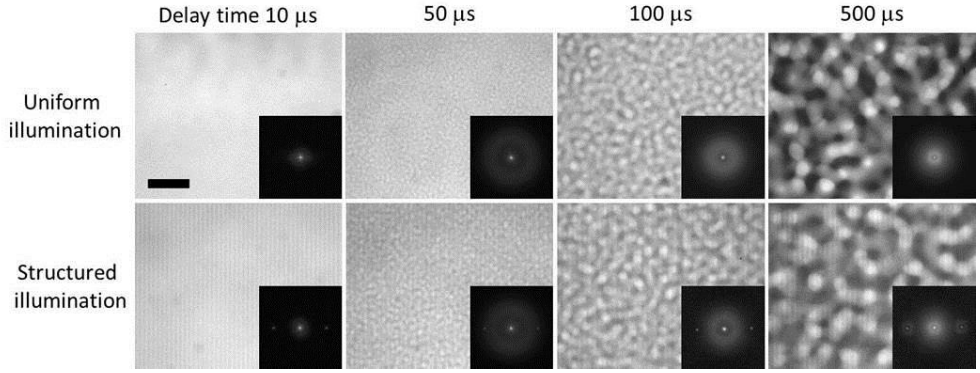

Fig.4-13 Fluorescence images during LIPS at various delay time after T-jump. Upper: uniform illumination. Lower: structured illumination.

The analyzed power spectra taken with UI and SI are shown in Fig.4-14 (a) and (b), respectively. Fine and coarse dashed lines present diffraction limit and SIM limit of our experimental system, respectively. Although there was not significant peak in the spectra obtained with UI at delay times 15 and 16 μs, a peak was obviously observed with SI above the diffractive limit at these delay times. At delay times 18 and 20 μs, a clear peak with UI was observed. Despite this, these positions seemed to be limited below the diffraction limit. It is implied that these power spectra were modified by the OTF of our microscope system. Calculated characteristic lengths from these peak positions are plotted as functions of delay time in Fig.4-15. This figure shows that spatial information below diffraction limit was successfully obtained. The method showed considerable potential for the detection of a periodic structure with nanosecond temporal resolution in a liquid. To be our best knowledge, this is the first time to obtain the super-resolution information of transient phase separating mixtures by using a microscopic technique.

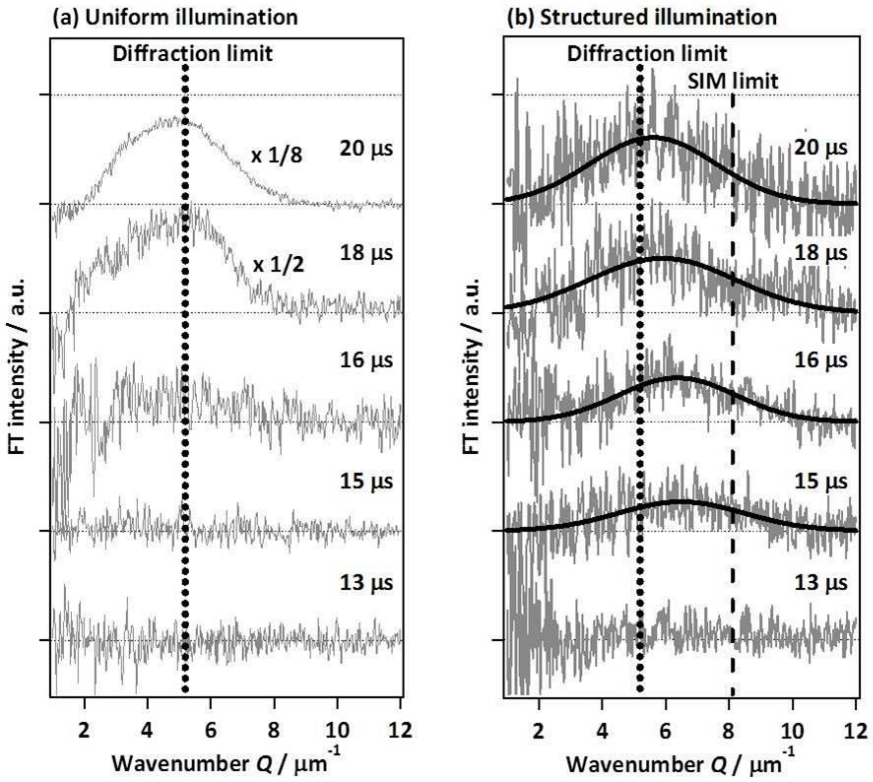

Fig.4-14 Power spectra at various delay time taken with (a) uniform illumination and (b) structured illumination. Fine and coarse dashed lines correspond to diffraction limit and SIM limit of our experimental system. Black solid lines are eye guides for these power spectra.

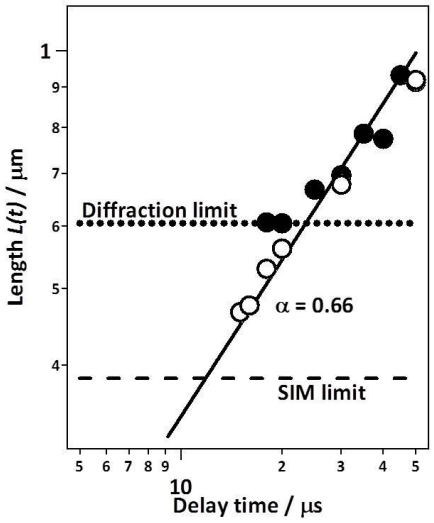

Fig.4-15 Characteristic lengths obtained with UI and SI are plotted as functions of delay time. Closed and open circles express the results of uniform illumination and structured illumination, respectively. Fine and coarse dashed lines correspond to diffraction limit and SIM limit of our experimental system.

4-3-3 Fluorescent dyes

Another fluorescent dye, rhodamine B (RhB), was also used in nanosecond SIM experiments. Although RhB allowed us to obtain high quality fluorescence images of phase separating medium with UI, spatial information below diffraction limit for delay time 15 to 20 μs with SI was not obtained. This result implies that solvent environment around RhB molecules was not equilibrated yet for the time range. To verify this possibility, dynamic changes of solvent environment during LIPS were investigated by measuring transient fluorescence spectra of BPDI and RhB at various delay time after T-jump.

(a) Steady-state fluorescence spectra

As preliminary experiments, steady-state fluorescence spectra of BPDI and RhB were measured at various 2BE molar fractions at room temperature. Some obtained spectra of BPDI are shown in Fig.4-16 (a). A shift of peak position was observed with varying of 2BE molar fraction. Peak positions are plotted as a function of 2BE molar fraction in Fig.4-16 (b). Peak position shows gradual change at low 2BE concentration, and rapid change around 0.0175 with respect to 2BE molar fraction. The rapid change can be explained by formation of micellar aggregates [19,20] as mentioned in Chapter 1. Since BPDI is highly hydrophobic, it is conceivable that BPDI molecules are wrapped with 2BE micellar aggregate above the CMC of water/2BE mixture. The CMC is reported at 0.0175 at 25°C.[19] In addition, peak position shifted gradually toward shorter wavelength. This change can be explained by coalescence of the micellar aggregates with an increase of 2BE molar fraction as mentioned in FCS part (Chapter 3).

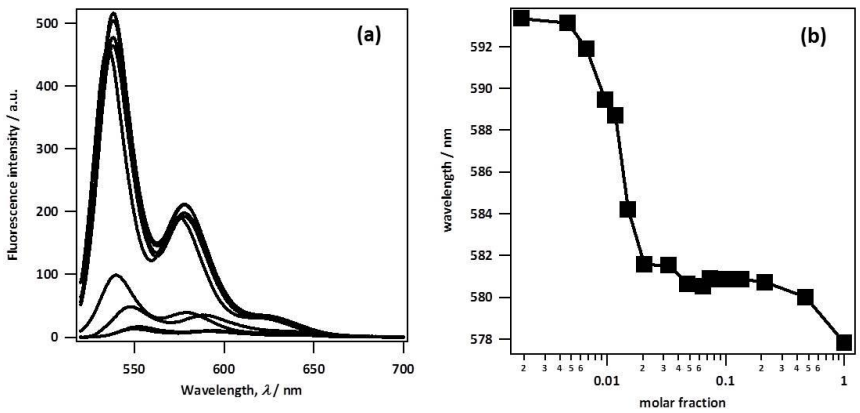

Fig.4-16 (a). Fluorescence spectra of BPDI at various 2BE molar fractions. (b) Peak positions of second peak of BPDI fluorescence plotted as a function of 2BE molar fraction.

Some obtained spectra of RhB are shown in Fig.4-17 (a). A shift of peak position was observed with varying of 2BE molar fraction. Peak positions are plotted as a function of 2BE molar fraction in

Fig.4-17 (b). In this case, change of peak position was more complicate than BPDI. At low concentration of 2BE, peak position shifted toward longer wavelength. Around 2BE molar fraction 0.0175, peak position returned rapidly toward shorter wavelength. And then, peak position shifted toward longer wavelength again. Above 0.2 with respect to 2BE molar fraction, peak position returned gradually toward shorter wavelength again.

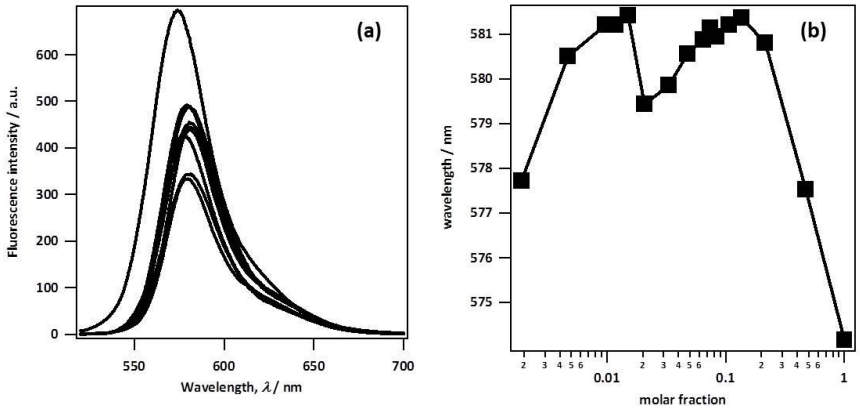

Fig.4-17 (a). Fluorescence spectra of RhB at various 2BE molar fractions. (b) Peak positions of RhB fluorescence plotted as a function of 2BE molar fraction.

(b) Transient fluorescence spectra

Next, results of transient fluorescence spectrum measurements are described here. Fig.4-18 shows transient fluorescence spectra of BPDI (a) and RhB (b) at -1 μs and 1 ms after T-jump. One can see a blue shift of peak position. The peak positions are plotted as functions of delay time after T-jump in Fig.4-18 (c). In the case of BPDI, changes of peak position from 580 nm to 578 nm took place for approximately 1 μs after T-jump. This result looks consistent with results of previous time-resolved (TR) Raman spectrum measurements. TR Raman spectra showed that molecular level changes terminated within 1 μs after the T-jump.[2] According to steady state fluorescence study described above, it is speculated that the change of peak position corresponds to a change of solvation behavior of BPDI. And then the peak position gradually returned to the start point. The return of peak position is may be due to dissolving spatial overlap between a near IR pulse and an excitation green pulse.

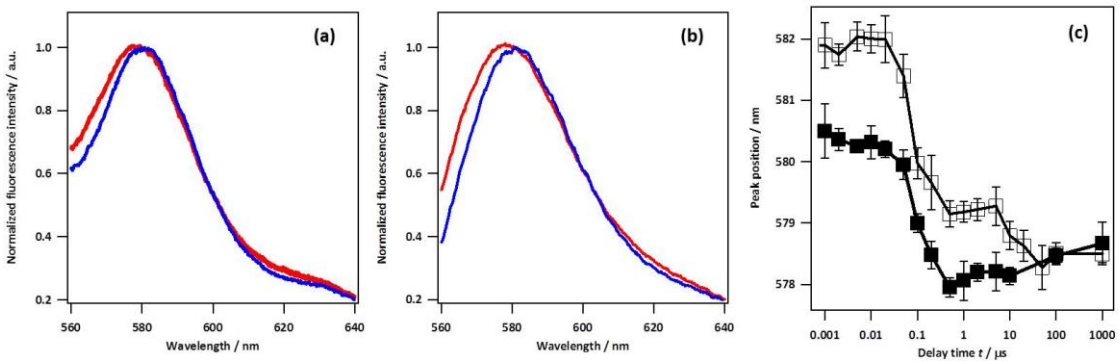

Fig.4-18 (a) Transient fluorescence spectra of BPDI obtained at delay time -1 μs (blue line) and 1 ms (red line). (b) Transient fluorescence spectra of RhB obtained at delay time -1 μs (blue line) and 1 ms (red line). (c) Changes of peak positions of BPDI (closed squares) and RhB (open squares) during LIPS with time.

In the case of RhB, changes of peak position took place for approximately 1 μs like BDPI. However an additional blue shift was observed from 10 μs after T-jump. The change lasted within 50 μs. This second change of peak shift may be due to an effect of interfaces of macroscopic phases. RhB is an ionic compound. From the results, it was found that solvent environment around RhB molecules was not equilibrated yet for 50 μs after T-jump, leading that RhB was not available in nanosecond SIM.

From a study by using FCS (Chapter 4) and the transient fluorescence spectrum measurements, it was found that different solutes can experience different environments even within the same solvent mixtures. Hydrophobic dye showed obvious slow-down of diffusion far below LCST. On the other hand, changes of solvent environment for hydrophobic dye terminated earlier than hydrophilic dye during phase separation. This information is important from viewpoint of application and investigation of dynamics of phase separation.

4-4 Early stage of laser-induced phase separation

For earlier delay time, light scattering was employed to investigate dynamics of LIPS. Some power spectra at early delay time are shown in Fig.4-19. A single peak was observed in each power spectrum, indicating that a characteristic length represents the phase domain size at each delay time. Fig.4-19 shows that the peak position remains at approximately Q = 10 μm^{-1}, corresponding to a characteristic length of 0.63 μm for delay times ranging from 3 to 7 μs.

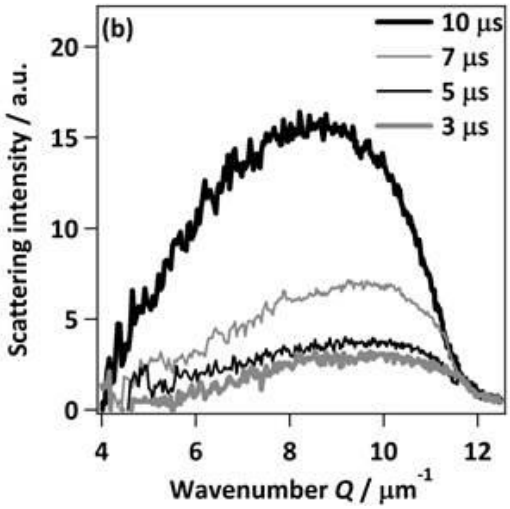

Fig.4-19 Time evolution of the power spectrum during LIPS in the water/2BE mixture; depicting power spectra for a delay time of 3–10 μs.

Fig.4-20 shows the domain size in the mixture as a function of delay time. By assuming that the sizes of the water-rich and 2BE-rich phases are the same (critical quench), the phase domain size $L(t)$ was defined as half of the characteristic length. Two obvious time regions are observed in Fig.4-20. In the later region beyond 10 μs, the change in $L(t)$ with time follows the power law $L(t) \sim t^{\alpha}$, as mentioned in section 6-2. At delay times below 10 μs, the $L(t)$ were almost constant at approximately 300 nm. The light scattering intensity at the wavenumber Q = 10 μm^{-1} is plotted as a function of delay times from 2 to 10 μs in Fig.4-21. The figure clearly shows that the intensity increased exponentially. In the early stage of SD, linearized Cahn–Hilliard theory [21-23] predicts that the domain size remains constant while the scattering intensity increases exponentially with time. Therefore, these results indicate that the early stage of SD in water/2BE lasted for 10 μs. Mallamace *et al.* reported that the early stage of SD in water/2BE mixtures with shallow quench depths follows the linearized Cahn–Hilliard theory.[10] The early stage growth rate and domain size, however, were much faster and smaller, respectively, compared with their experiment because of a difference in the quench depth.

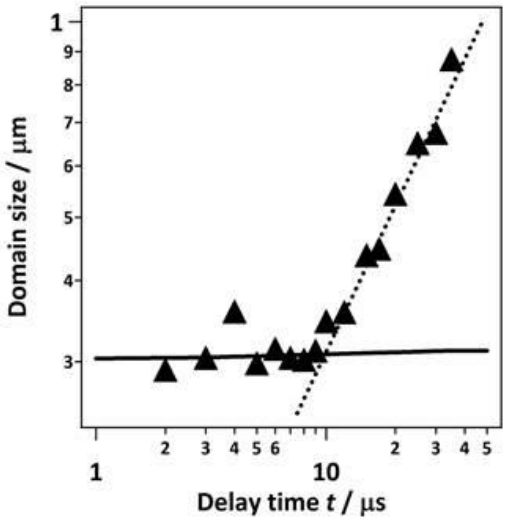

Fig.4-20 Domain sizes plotted as a function of delay time. The solid and dotted lines present fitting curves before and after 10 μs with t^{α}, respectively; the respective exponents are 0.021 and 0.72.

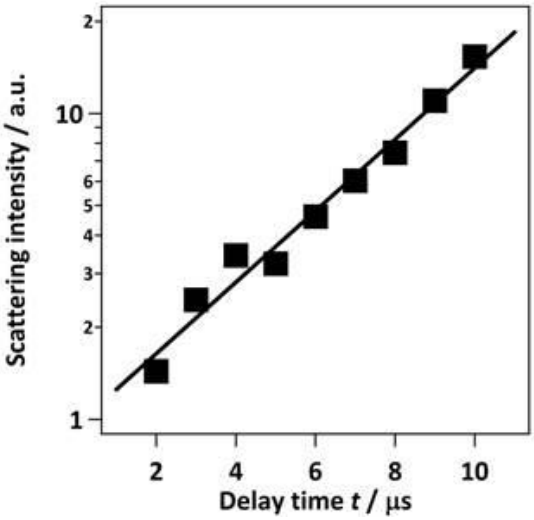

Fig.4-21 Scattering intensity at wavenumber Q = 10 as a function of delay time. The solid line presents a fitting curve with an exponential function.

From the linearized Cahn–Hilliard theory, the domain size at the onset of the late stage of SD in a binary liquid mixture is expected to be inversely proportional to the square root of the quench depth.[2,10,23-25] In previous studies with shallow quenches, quench depths were ~0.05 K, and the domain sizes at the early stage in binary liquid mixtures were reported to be around several μm.[7,9,10]. In our case, quench depth was 5.0 K, which is 100 times deeper than that of previous studies, indicating a 10-fold smaller domain size. The estimated domain size is several hundred

nanometers, which is in good agreement with our observation (300 nm). In addition, the growth rate at the early stage of SD is proportional to square of the quench depth,[2,10] suggesting an overall rate increase of approximately four orders of magnitude. This estimation is also in good agreement with our results, indicating that the linearized Cahn–Hilliard theory is applicable for the early stage of LIPS with a deep quench depth.

The linearized Cahn-Hilliard theory is developed based on symmetric free energy. However, the coexistent curve of water/2BE mixture shows asymmetry. Therefore, when the quench depth becomes higher, it is expected that a deviation from the linearized Cahn-Hilliard theory would be observed due to the asymmetry. For more detail examination of the linearized Cahn-Hilliard theory, a further light scattering experiment with changing of quench depth in LIPS is needed. To accomplish such a further examination, more accurate temperature control and more high stability of the near IR pulse are necessary. These improvements of experimental detail are challenges in future.

4-5 A new view of the early stage of spinodal decomposition

Based on our observations and previous TR Raman scattering, early stage of phase separation in water/2BE mixture is discussed. Note the previous TR Raman spectra show that the molecular level change ends within 1 μs after the T-jump.[2] From the results, it was concluded that early and intermediate stages of SD are also over in 1 μs, since these both should involve composition changes within the phase domains that would lead to spectroscopic change. However, from our observations, it is found that the early stage lasted within 10 μs.

This temporal gap between TR Raman spectra and our observations can be explained by considering molecular-level changes inside a local solution structure in water/2BE mixture. It is well known that 2BE molecules form micellar aggregates in the water/2BE mixture due to 2BE amphiphilic properties as mentioned in Chapter 1. Since it have been reported that critical micelle concentration (CMC) in water/2BE mixtures are 2BE molar fraction 0.0175 at 25°C and 0.0131 at 55°C, it should be considered that the number of 2BE micellar aggregates change with a temperature jump. Moreover It have been also reported that the 2BE micellar aggregates are unstable and show flexible shape due to the short length of 2BE carbon chain compared with a micelle structure formed by other typical surfactants.[20] It is therefore conceivable that a certain water molecule is contained inside the 2BE micellar aggregates, and the composition of the 2BE micellar aggregates change with a temperature jump. That is to say, it is suggested that the previous TR Raman spectra change within delay time 1 μs can be interpreted by the changes in density and composition of the 2BE micellar aggregates (Fig.4-27 A to B). When the changes terminate, water/2BE mixture reaches equilibrium state locally.

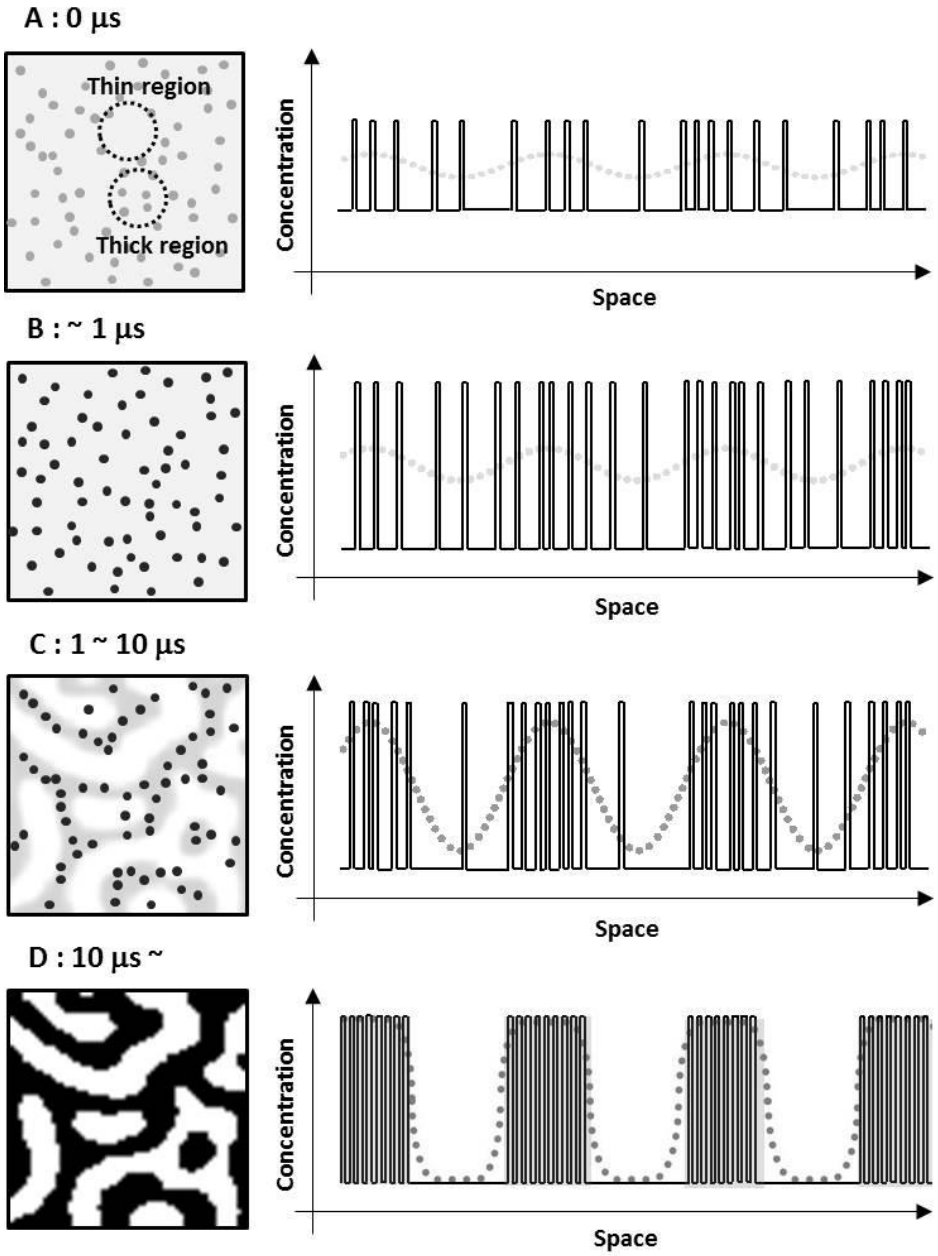

Fig.4-27 conceptual images of early stage of SD in LIPS.

After delay time 1 μs, it was conceivable that density fluctuation of the 2BE micellar aggregate exponentially increased with a time, leading to the increase of light scattering intensity. Many experimental studies revealed that binary liquid mixtures having their LCSTs like water/2BE mixture show large concentration fluctuations even below their LCSTs.[24] Corti *et al.* investigated aqueous solution of n-Dodecyl hexaoxyethylene glycol monoether ($C_{12}E_6$) which is nonionic surfactant having longer chain length than 2BE (C_4E_1) by using dynamic light scattering at below its LCST, and suggested that density fluctuation of micellar aggregate increase with approaching to its

LCST.[25] By applying their discussions of the micelle structure of longer surfactant ($C_{12}E_6$) to water/2BE mixture (water/C_4E_1), it is conceivable that density fluctuation of 2BE micellar aggregates grew for 10 μs, and a new phase formed by coalescence of these micellar aggregates in water/2BE mixture (Fig.4-27 B-D). Although fluctuations of molecular density have been considered in study on phase separation so far, our study strongly indicate that we have to consider fluctuations of mesoscopic structures like 2BE micellar aggregates instead of molecular density. It is already known that there is a hierarchical structure in water/2BE mixture as described in chapter 1. However, this study revealed that the hierarchical structure is important even in dynamics of phase separation.

4-6 Conclusion

Findings of this study are summarized as follows. First of all, a comparison with shadowgraph-, fluorescence-imaging, and light scattering are carried out. Time evolution of phase domain size $L(t)$ determined with these methods showed macroscopic phase growth following power laws $L(t) \sim t^{\alpha}$. From the comparison, it was found that only shadowgraph-imaging showed a difference in the growth rates of phase domain size when the thickness of a sample was thin enough. The nanosecond SIM successfully demonstrated the observation of super-high spatial frequency. The method showed considerable potential for the detection of a periodic structure with nanosecond temporal resolution. In addition, it was found that different solutes could experience different environments even within the same solvent mixtures. Changes of solvent environment for hydrophobic dye terminated earlier than hydrophilic dye during LIPS. For earlier delay time, light scattering was employed to investigate dynamics of LIPS. The light scattering showed that $L(t)$ remained constant at approximately 300 nm until 10 μs after T-jump and the intensity of scattering light increased exponentially with time from 2 to 10 μs. To the best of our knowledge, this is the first report to show mesoscopic structural changes in this time region. In the early stage of spinodal decomposition, linearized Cahn–Hilliard theory predicts that the domain size remains constant while the scattering intensity increases exponentially with time. Therefore, it is clearly indicated that the early stage of LIPS in the water/2BE mixture lasted for 10 μs. Based on the observation and the previous Raman studies, it is indicated that the formation of new phases proceeds by increasing density fluctuation of the mesoscopic structure, that is, 2BE micellar aggregate.

References

[1] J. Hobley, S. Kajimoto, A. Takamizawa, K. Ohta, Q. Tran-Cong, H. Fukumura, *J. Phys. Chem. B*, **2003**, *107*, 11411.

[2] A. Takamizawa, S. Kajimoto, J. Hobley, H. Fukumura, Q. Tran-Cong, *Phys. Rev. E*, **2003**, *68*, 020501.

[3] J. Hobley, S. Kajimoto, A. Takamizawa, H. Fukumura, *Phys. Rev. E*, **2006**, *73*, 011502.

[4] T. Ohta, O. Urakawa, Q. Tran-Cong, *Macromolecules*, **1998**, *31*, 6845.

[5] K. Murata, T. Murata, H. Nakanishi, T. Norisuke, Q. Tran-Cong-Miyata, *Macromolecules*, **2009**, *294*, 163.

[6] S. Tanaka, Y. Kubo, Y. Yokoyama, A. Toda, K. Taguchi, H. Kajioka, *J. Chem. Phys.*, **2011**, *135*, 234503.

[7] J. S. Huang, W. I. Goldburg, A. W. Bjerkaas, Phys. Rev. Lett., 1974, 32, 921.

[8] Y. C. Chou, W. I. Goldburg, *Phys. Rev. A*, **1979**, *20*, 2105.

[9] N. Kuwahara, K. Kubota, M. Sakazume, H. Eda, K. Takiwaki, Phys. Rev. A, 1992, 45, R8324.

[10] F. Mallamace, N. Micali, S. Trusso, J. Phys.: Condens. Matter, 1996, 8, A81.

[11] M. G. L. Gustafsson, L. Shao, P. M. Carlton, C. J. R. Wang, I. N. Golubovskaya, W. Z. Cande, D. A. Agard, J. W. Sedat, *Biophys. J.*, **2008**, *94*, 4957.

[12] M. Beck, M. Aschwanden. A. Stemmer, *J. Microscopy*, **2008**, *232*, 99.

[13] L. Shao, B. Isaac, S. Uzawa, D. A. Agard, J. W. Sedat, M. G. L. Gustafsson, *Biophys. J.*, **2008**, *94*, 4971.

[14] K. Binder, *Phys. Rev. B*, **1977**, *15*, 4425.

[15] A. Zielesny, J. Schmitz, S. Limberg, A. G. Aizpiri, S. Fusenig, D. Woermann, *Int. J. Thermophys.*, **1994**, *15*, 67.

[16] N. Gonzalez-Segredo, M. Nekovee, P. V. Coveney, *Phys. Rev. E*, **2003**, *67*, 046304.

[17] J. C. Hulteen, R. P. Van Duyne, *J. Vac. Sci. Technol. A*, **1995**, *13*, 1553.

[18] J. Y. Shiu, C. W. Kuo, P. Chen, Chung. Y. Mou, *Chem. Mater.*, **2004**, 16, 561.

[19] M. D'Angelo, G. Onori, A. Santucci, *Chem. Phys. Lett.*, **1994**, *220*, 59.

[20] K. Yoshida, T. Yamaguchi, T. Otomo, M. Nagao, H. Seto, T. Takeda, J. Mol. Liq., **2005**, *119*, 125.

[21] J. W. Cahn, J. E. Hilliard, *J. Chem. Phys.*, **1958**, *28*, 258.

[22] J. W. Cahn, *Acta Met.*, **1961**, *9*, 795.

[23] J. W. Cahn, *J. Chem. Phys.*, **1965**, *42*, 93.

[24] N. Ito, T. Fujiyama, Y. Udagawa, *Bull. Chem. Soc. Jpn.*, **1983**, *56*, 379.

[25] M. Corti, V. Deglorglo, *J. Phys. Chem.*, **1981**, *85*, 1442.

Chapter 5 Bubble formation and light emission during laser-induced T-jump

5-1 Introduction

In this chapter, experimental results on bubble formation and light emission during laser-induced T-jump are shown. Although there are previous reports of the bubble formation during laser-induced phase separation,[1,2] to the best our knowledge, it is the first-time observation of light emission. The light emission with a bubble has been regarded as sonoluminescence[3]-like emission. However mechanisms of relevant bubble formation and the light emission were not clear. The purposes of this study are characterization and providing knowledge of the bubble formation and the light emission to reveal these mechanisms. Some imaging and spectroscopic techniques are used. The results are described from section 5-2 to section 5-4, and discussed from a viewpoint of correlation between the phenomena and LIPS. Based on our observations, one possible mechanism is proposed in section 5-5.

5-2 Observation of bubbles and emission spots

5-2-1 Bubble formation, growth, and collapse

Some shadowgraph images of bubbles at various delay time after a T-jump in water/2BE mixture are shown in Fig.5-1. White dotted ellipses in Fig.5-1 represent the near IR irradiation region. The bubbles were observed from 300 ns after T-jump. At early delay time, the shape of observed bubbles seemed to be completely spherical, and bubbles were observed only inside the near IR irradiation region. Positions of observed bubbles gradually spread to the outside of the irradiation region with time. After 1 μs, the shape of some bubbles became gradually distorted, and the positions came back into the irradiation region. From 50 to 100 μs, a crack was observed inside bubbles and bubbles collapsed. Almost all collapse of bubbles was observed around central area of the irradiation spot. After the collapse, the sample solution seemed to be stirred by the impact of collapse, and fragments of collapsed bubbles were observed.

Fig.5-2 shows time-evolution of the number and the averaged diameter of bubbles. Fitting curves with a power law t^{α} also plotted as black and gray lines for within and beyond 1 μs, respectively. In both figures, one can see a clear changing point of the time-evolution at approximately 1 μs. The number of bubbles rapidly increased until 1 μs and reached the maximum at 1 μs. And then, the number of bubbles gradually decreased. The diameter of bubble also grew rapidly until 1 μs, and became to be approximately 50 μm. A growth rate α was determined to be 2.2 from the fitting within 1 μs. After 1 μs, the diameter continued to increase. However, the growth rate became slow, and bubbles grew following the power law $t^{0.33}$. These results suggest that the mechanism of bubble growth changed at approximately 1 μs and the bubbles grow by getting together with multi-bubble by random walk after 1 μs. Diameters of bubbles at early delay time were estimated from the results by extrapolating the power law. The estimated diameter at

delay time 10 ns was approximately 20 nm.

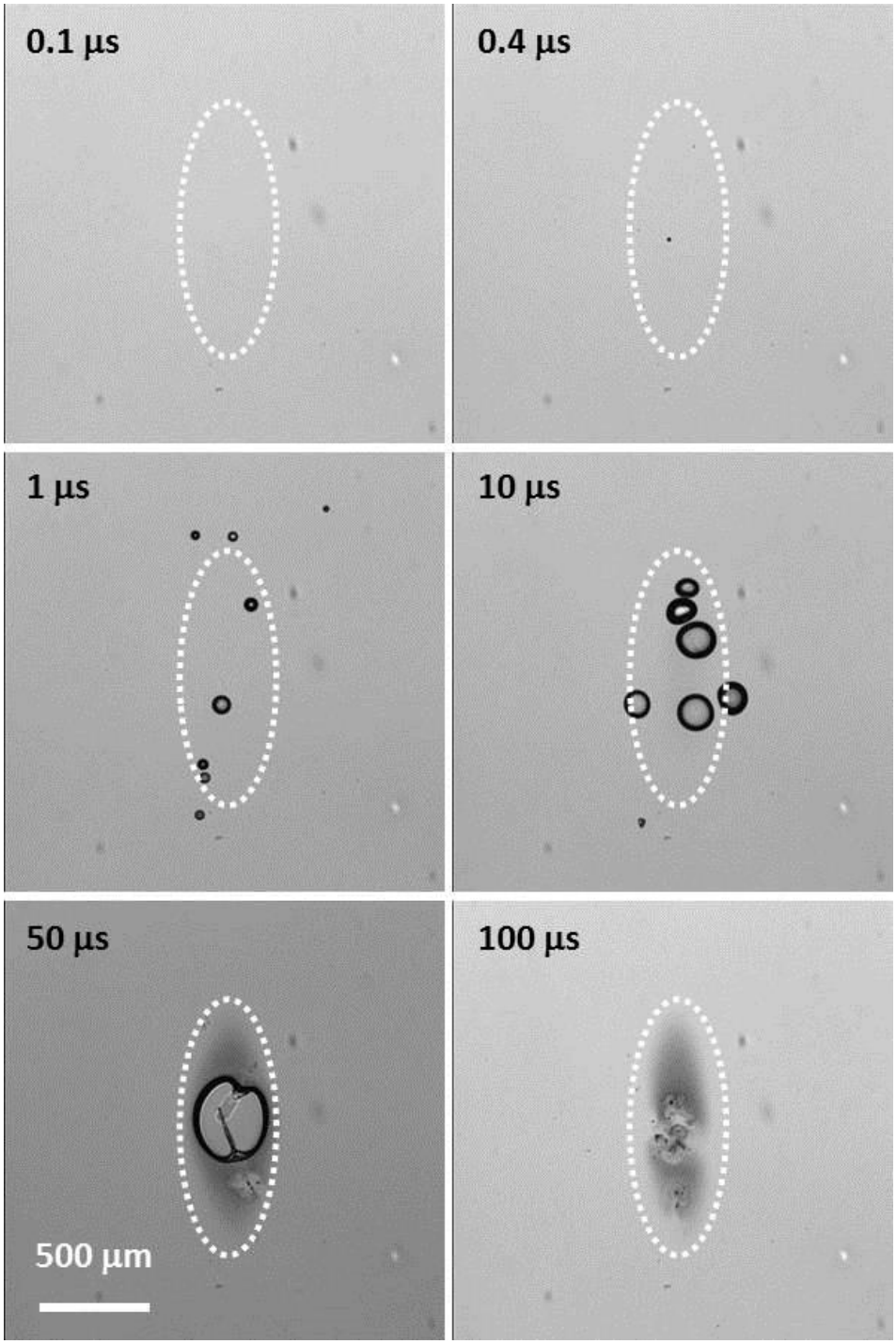

Fig.5-1 Shadowgraph images of bubble formation during LIPS at various delay times after T-jump. White dotted ellipses represent the near IR irradiation region.

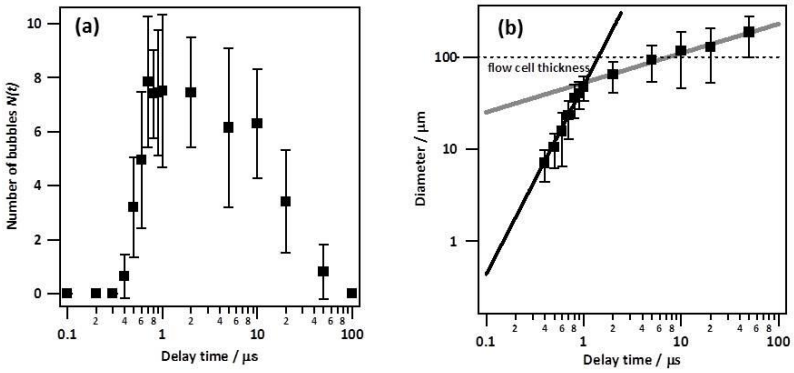

Fig.5-2 (a) Number of bubbles plotted as a function of delay time. (b) Diameter of bubble plotted as a function of delay time. Black and gray lines represent fitting curves with a power law ~ t^{α}. The determined exponents were 2.2 and 0.33 until and after 1 μs, respectively. Dash line presents the flow cell thickness 100 μs.

Since the thickness of the flow cell used here was 100 μm which is comparable with the diameter of bubbles at 1 μs, the growth of bubble seemed to be influenced with the thickness of the flow cell (Fig.5-2 b). To examine the influence of flow cell thickness, I also attempted to record a shadowgraph image using a thicker sample (1 mm). Fig.5-3 shows a comparison between results with 100 μm and 1 mm thickness flow cells. In the case of thicker flow cell, a changing point similar to the thinner cell case was observed. However the growth rate until 1 μs was obviously different and determined exponent from fitting was 1.0. This difference may be due to a defocusing effect on the shadowgraph-imaging. When sample thickness became large enough, it was difficult to optimize focus point of the objective lens, so that obtained bubble images were not clear especially at earlier delay time. Thus the diameter of some small bubbles was overestimated, and the growth rate became smaller.

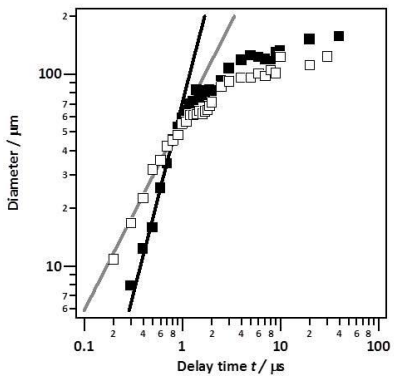

Fig.5-3 Diameters of bubbles plotted as function of delay time. Closed and open squares present the results with 100 μm and 1 mm thickness flow cell, respectively. Black and gray lines represent fitting results with a power law t^{α}, determined α are 2.1 and 1.0, respectively.

5-2-2 Emission spots

An emission spot image at delay time 0 ns taken with the 100 ns time-gated CCD camera is shown in Fig.5-4 (a). The gated time was from 0 to 100 ns. The number of emission spots were counted and plotted in Fig.5-4 (b) at each delay time. The figure clearly shows that almost emission spots were observed within 100 ns after the near IR irradiation. In Fig.5-4 (b), the number of bubbles observed with shadowgraph imaging is also plotted as gray line. It was found that the light emission occurred within several hundreds nanoseconds after T-jump and before the bubble observation. Generally it is known that sonoluminescence is observed when a bubble which forms in a liquid collapses (Fig.5-5).[3] However, according to our observations, it was revealed that the light emission did not result from the collapsing of micrometer size bubbles. As a possibility for a cause of the light emission, collapsing of nano-bubble still remains. The diameter of bubbles at 10 ns was estimated to be 20 nm by extrapolating from the results of shadowgraph-imaging (Fig.5-2 (b)). The possibility is described in section 5-5. Furthermore, in this experiment, gate time was 100 ns. Thus it is impossible to discuss a rise and a decay of the light emission. For investigation of this point, a streak camera was employed. The results are shown in section 5-4.

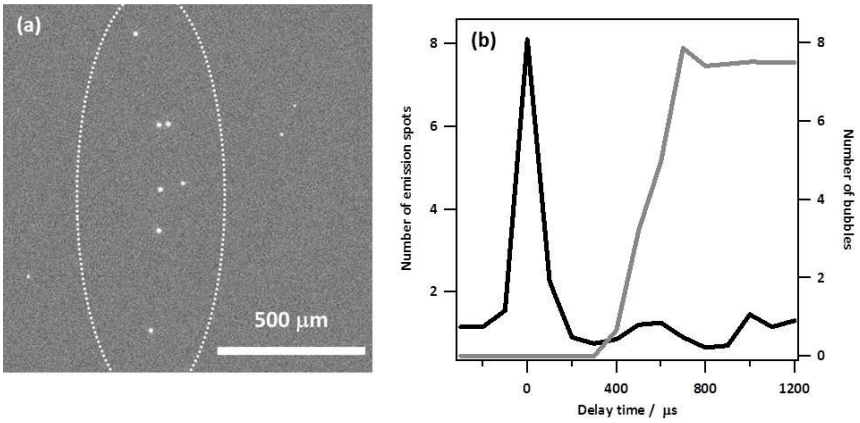

Fig.5-4 (a) Emission spot image take with 100 ns time-gated CCD camera. Delay time was at 0 ns (from 0 to 100 ns). A white dotted ellipse presents the near IR irradiation spot. (b) A black line presents the number of bright spots observed at each delay time (left axis). The number of bubbles observed is also plotted as a function of delay time (gray line, right axis).

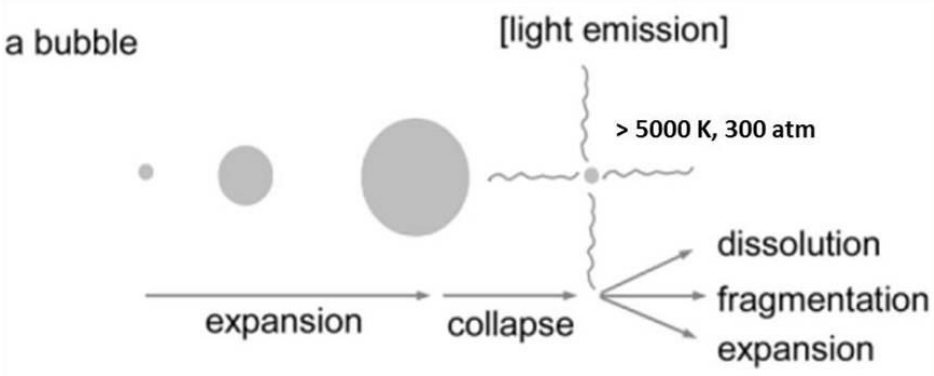

Fig.5-5 Conceptual image of sonoluminescence. Ref.3.

It should be mentioned here that some of emission spots were observed at outside of the near IR irradiation region. The region is represented in Fig.5-4 (a) as a white dotted ellipse. These outside emission spots were observed within approximately 100 μm far from the edge of the near IR irradiation region. This result indicates that the light emission was not induced directly with irradiation of the near IR pulse, and something moved for 100 μm within 100 ns.

5-2-3 Temperature dependence

To examine whether the bubble formation and the light emission result from LIPS, the temperature dependence on the numbers of bubbles and emission spots were measured. In this experiment, water/2BE mixture having the critical composition was used as a sample solution. For comparison, pure water, water/TEA mixture, and water/EG mixture were also used. Water/TEA mixture was prepared at the critical composition (TEA molar fraction 0.077), and water/EG mixture was prepared at 0.052 with respective to molar fraction. An initial temperature of sample solution was controlled from 5 to 45°C, and the intensity of near IR pulses was also varied from 0.15 to 1.9 J/pulse•cm^2 corresponding to the magnitude of T-jump 4.0 ~ 52.7°C for 10 μm depth of front surface. If the phenomena result from LIPS, the numbers of bubbles and/or emission spots are expected to depend on whether phase separation occurs or not.

The final temperatures after T-jump are calculated from the initial temperatures and the magnitudes of T-jump, and the number of bubbles observed with shadowgraph imaging at the delay time of 1 μs and the number of emission spots are plotted in Fig.5-6 as functions of the final temperatures. According to Fig.5-6 (a), only few bubbles were observed when the final temperature was lower than 30°C even though the IR intensity was high. When the final temperature was higher than 30°C bubbles were observed and the numbers increased monotonically with the final temperature. The number of emission spots also shows similar trend to the number of bubbles (Fig.5-6 (b)). Form both figures, one can see a strong correlation between the numbers and final temperature after T-jump, indicating that bubble formation and light emission resulted from LIPS or,

at least, related to LIPS.

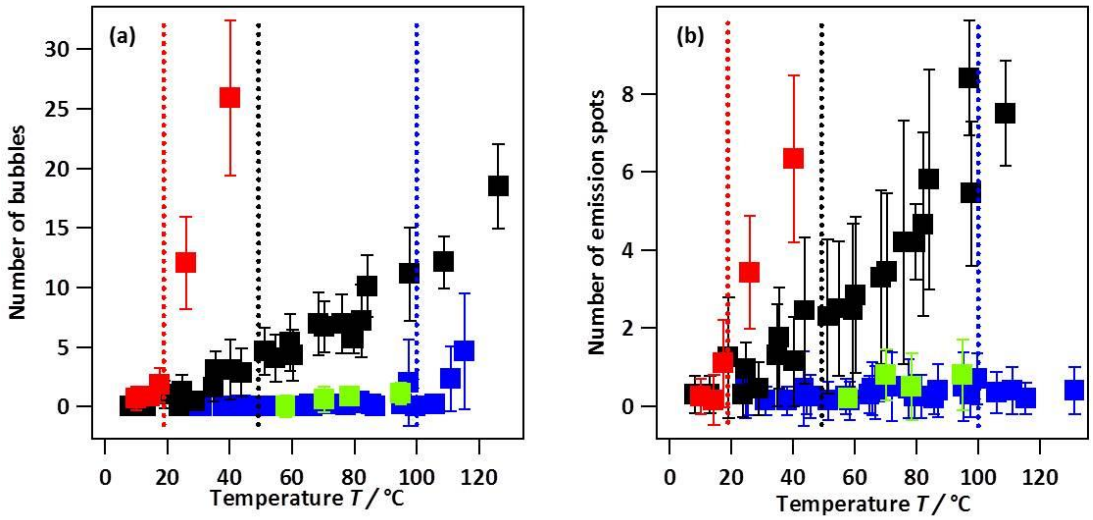

Fig.5-6 Numbers of bubbles observed with shadowgraph imaging at the delay time of 1 μs (a) and emission spots (b) plotted as functions of the final temperature after T-jump. Black, red, blue, and green squares present results of water/2BE mixture, water/TEA mixture, pure water, and water/EG mixture, respectively. Black, and red, and blue dotted lines present the LCST of water/2BE mixture, the LCST of water/TEA mixture, and the boiling point of water, respectively.

For comparison, results of some reference solutions were also plotted in Fig.5-8. Water/TEA mixture also has its LCST at 18.8°C (Fig.5-6 red dotted line). The results of the mixture were represented with red squares. In this case, final temperature dependence on the numbers of bubbles and emission spots shows similar trend to the results of water/2BE mixture. Below the LCST, few bubbles and emission spots were observed. Alternatively above the LCST, bubbles and emission spots were observed and the numbers increased with the final temperature. Blue squares in Fig.5-6 represent the results of pure water. In this case, below the boiling point of water (Fig.5-8 blue dotted line), very few bubbles were observed. On the other hand, above the boiling point many bubbles were observed. A shadowgraph image of the bubbles formed in water is shown in Fig.5-7. A white dotted ellipse in the figure present the near IR irradiation region. These bubbles were observed only inside the near IR irradiation region, and can be due to boiling of water. Even bubbles formed in water, contrary to mixtures with their LCSTs, very few emission spots were observed in water (Fig.5-6 (b)). Green squares represent the results of water/EG mixture, which does not have its critical point and is completely miscible. In this case, very few bubbles and emission spots were observed even at high final temperature. These results of reference experiments also indicated that the bubble formation and the light emission resulted from or related to LIPS.

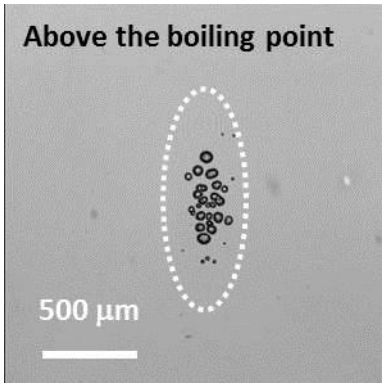

Fig.5-7 Shadowgraph image of bubbles formed in pure water at 1 μs after T-jump. The final temperature was above the boiling point of water.

It should be noted that a clear threshold was not observed at the LCST (49.3°C) of water/2BE mixture. This means that "macroscopic" phase separation was not an essential factor for bubble formation and light emission during T-jump. As mentioned in chapter 1, it is known that micellar aggregates form and large concentration fluctuations exist in water/2BE mixture,[5-10] and it is suggested that water/2BE mixtures is behaving in preparation for phase separation at microscopic- and mesoscopic-level even in one phase region.[11] The observation may be a result from such microscopic- and mesoscopic-level phase separation.

5-2-4 Composition dependent

Fig.5-8 (a) and (b) show the numbers of bubbles observed with shadowgraph-imaging at delay time 1 μs and emission spots as functions of 2BE molar fraction χ, respectively. Initial solution temperatures were kept at 24°C. In this experiment, a difference in the magnitude of T-jumps due to a difference in water composition should be considered because the optical absorption of a mixture at 1.8 depends on the composition. For instance, when I used 1.0 J/pulse•cm^2 of a near IR pulse, the magnitudes of T-jump at 2BE molar fraction of 0.0 and 0.27 were 34 K and 16 K, respectively, and the difference in magnitude of T-jump was 18 K. Therefore I used different near IR pulse intensities for each molar fraction mixture to keep the final temperature the same. Difference in the final temperatures was estimated within 3 K. The average of final temperature was 75.3°C and above the LCST of water/2BE mixture.

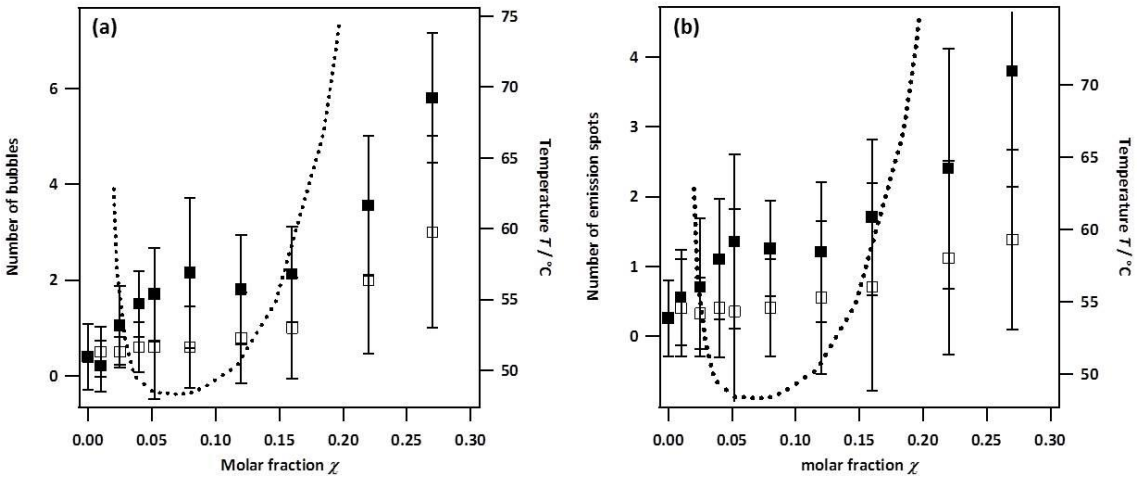

Fig.5-8 Numbers of bubbles (a) and emission spots (b) plotted as functions of organic solvent molar fraction, χ. Closed and open squares present results of water/2BE mixtures and water/EG mixtures, respectively. A Dotted line presents the coexistent curve of water/2BE mixture.

As reference samples, water/EG mixtures were used and the results were also plotted in Fig.5-10. In the case of the water/EG mixture, the number of bubbles increased monotonically with an increase of EG molar fraction. It was found that bubble formation and light emission could be observed in even a miscible binary mixture. In the case of water/2BE mixtures, the number of bubbles also increased with an increase of 2BE molar fraction. However the number of bubbles in the water/2BE mixtures has a local maximum around 0.08 with respect to 2BE molar fraction. In Fig.5-8, the coexistent curve of water/2BE mixture was plotted together. A region where the additional increase was observed clearly overlapped with the coexistent curve. The numbers of emission spots in both mixtures showed similar trend to the number of bubbles. From these results, it was revealed that phase separation was not essential factor but promoted the bubble formation and the light emission.

5-2-5 Correlation between bubble formation and light emission

In Fig.5-9, the numbers of emission spots are plotted as functions of the numbers of bubbles with different mixtures. There is a clear positive correlation between the numbers of bubbles and emission spots in the result of water/2BE mixture (black squares), indicating that these two phenomena were related with each other. Note that light emission occurred within a few hundreds nanoseconds, and was not observed when micrometer size order bubbles collapsed. This indicated that bubble formation resulted from light emission or something happened during laser-induced T-jump resulted in both the bubble formation and the light emission. The number of emission spots in water was almost zero, even when bubbles formed. In the case of water/EG mixture, the results

also showed a clear positive correlation. It was found that organic solvents were an important factor for observation of emission spots.

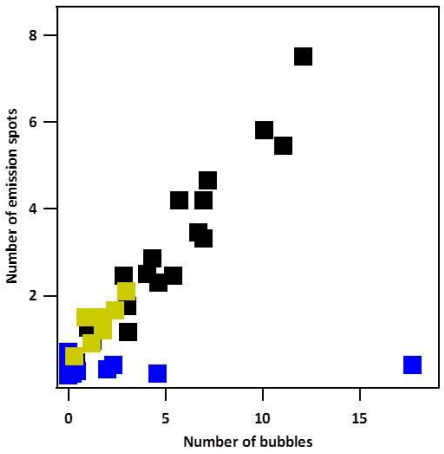

Fig.5-9 Numbers of emission spots plotted as functions of the number of bubble. Black, blue, and green squares present results of water/2BE mixture, pure water, and water/EG mixture, respectively.

5-3 Effects of dissolved gas and addition of salt

5-3-1 Dissolved gas

Effects of dissolved gas in water/2BE mixture were examined to confirm what bubbles consisted of. Three gasses, oxygen, nitrogen and argon, were used for bubbling, and degassing treatment was also carried out. Fig.5-10 shows the number of bubbles at various bubbling conditions. Bubbling treatment with any gas made the number of bubbles large. On the other hand, the degassing treatment made the number of bubbles less. This result suggests that bubbles formed during laser-induced T-jump consist of dissolved gasses.

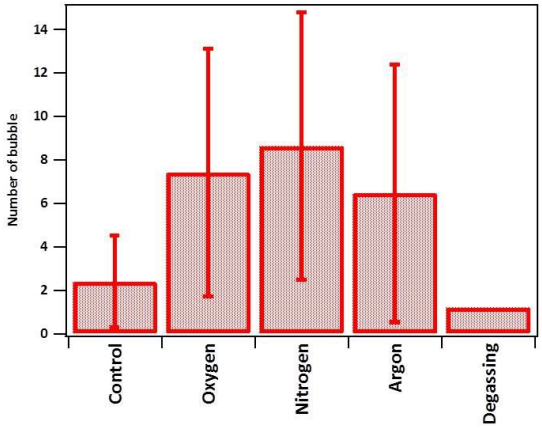

Fig.5-10 Dissolved gas effect on the number of bubbles.

5-3-2 Addition of salt

Since it is known that addition of salts enhances sonoluminescence through stabilizing nucleuses of bubbles,[12] effects of adding salt on bubble formation and light emission during laser-induced T-jump were investigated. In this experiment, the molar ratio of 2BE to water was kept and also final temperatures after T-jump were kept at around 75.3°C. Fig.5-11 (a) shows a shadowgraph image of bubbles in water/2BE mixture with 10^{-3} molar fraction of KCl. In this case, the phase separation temperature of the water/2BE/KCl mixture was reduced to 25.7°C.[13,14] With compared to the results without adding salts (Fig.5-1), the number of bubbles increased dramatically. A similar trend was observed on the number of emission spots. It was found that the adding salts promoted bubble formation and light emission during LIPS. This result can be explained by considering of the stabilizing nucleuses of bubbles and reducing the LCST corresponding to increasing quench depth. Effects of adding salts in pure water, water/EtOH mixture, and water/Acetone mixture were also investigated. Fig.5-11 (b) shows a shadowgraph image of bubbles in pure water with the same concentration of KCl to water/2BE/KCl mixture. Many bubbles were observed also in the image even though the laser intensity was not high enough to induce water boiling. In cases of water/EtOH mixture and water/Acetone mixture, a similar increase of bubbles was observed. The results indicate that stabilizing nucleuses of bubbles was a predominant effect of adding salt. By considering that phase separation promoted bubble formation and light emission phenomena, stabilizing nucleuses of bubbles might occur during LIPS. In addition, with assumption that the light emission in the KCl aqueous solution was the same to the light emission in organic solvent aqueous solutions, the results also indicate that an emission species might not originate in organic solvents. Emission species discussed in next section by measuring emission spectra.

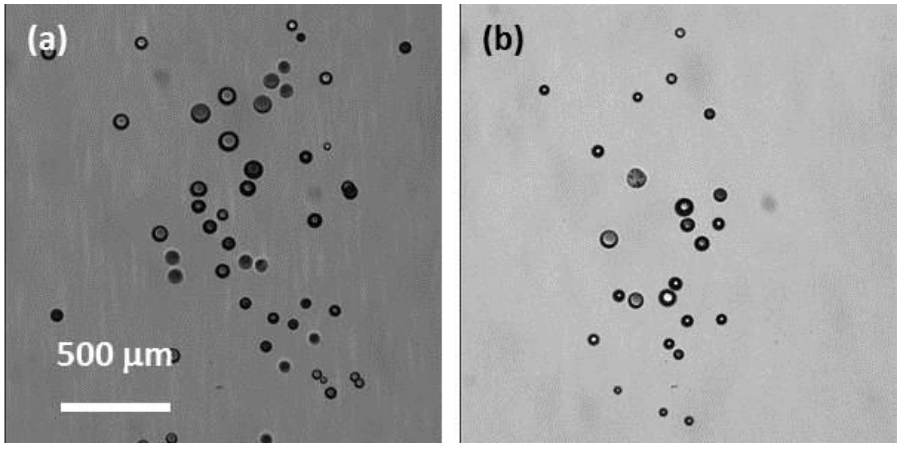

Fig.5-11 Shadowgraph image of bubbles in water/2BE/KCl mixture (a) and KCl aqueous solution (b) with 10^{-3} molar fraction of KCl observed at delay time of 1 μs after T-jump.

5-4 Time-resolved emission spectrum measurements

To identify an emission species of light emission during T-jump, emission spectra were measured by using two detection systems. One was a spectrograph and a time-gated iCCD camera setup. The other was a streak camera, which enables us to measure emission spectra and the emission decays simultaneously.

5-4-1 Emission spectrum

Fig.5-12 (a) shows results of emission spectrum measurement with the second detection system. A broad emission from water/2BE mixture was observed from 400 to 900 nm (black line). In this detection system, light emission spectrum from water also was obtained (blue line). Normalized spectra are also shown in Fig.5-12 (b). These two spectra show almost the same shape, indicating that emission species did not originate in 2BE molecules. The peak position was around 580 nm corresponding to the temperature of ~5000 K which was determined from the peak position with assumption blackbody radiation.

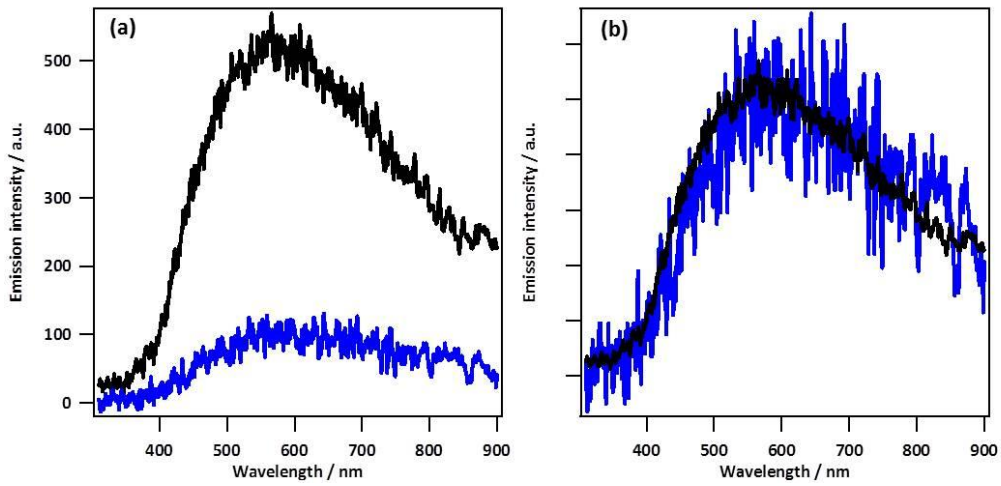

Fig.5-12 (a) Emission spectra of water/2BE mixture (black line) and pure water (blue line). (b) Normalized emission spectra of water/2BE mixture (black line) and pure water (blue line).

Next, Fig.5-13 an observed streak image of emission induced with irradiation of near IR pulse for water/2BE mixture. Emission was clearly observed at around delay time of 20 ns. This result consistent with emission spot images captured with the iCCD camera shown in Fig.5-4. A spectrum obtained by integrating from -10 ns to 900 ns is shown as black line in Fig.5-12 (b). A blackbody radiation-like broad emission was observed from 400 to 800 nm again. In Fig.5-12 (b), an emission spectrum of pure water is also shown as blue line. Intensity of the emission was very weak and almost background level.

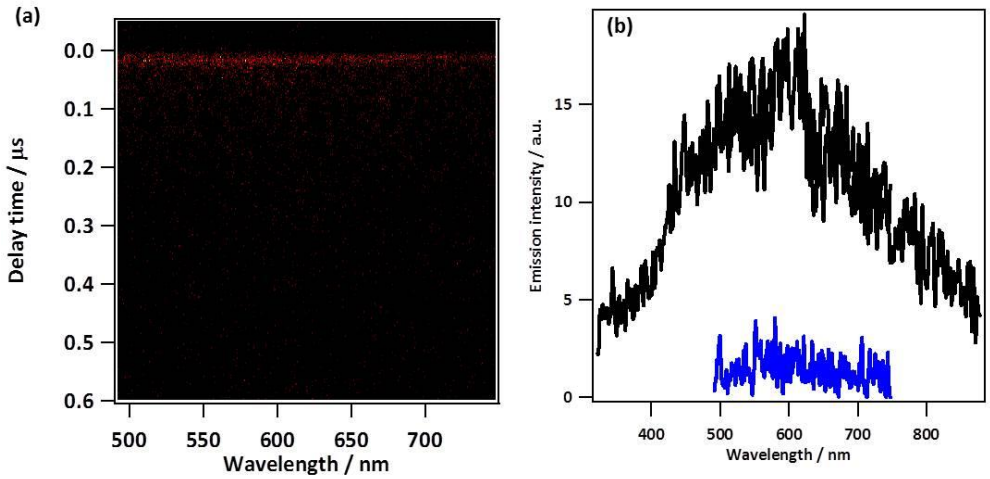

Fig.5-13 (a) a streak image of emission induced by with near-IR pulse irradiation into water/2BE mixture (500 - 700 nm). (b) Integrated emission spectra from -10 ns to 900 ns. Black and blue lines present emission spectra of water/2BE mixture and pure water, respectively.

To check spectral changes with time, the emission spectrum of water/2BE mixture was separated into three time region. Emission spectra obtained by integrating from -50 to 50 ns, from 50 to 250 ns, and from 250 to 650 ns are shown in Fig.5-14. The peak position of these spectra showed a red shift from 565 to 582 nm corresponding to temperature change approximately from 5130 to 4980 K which were determined from the peak position with assumption blackbody radiation.

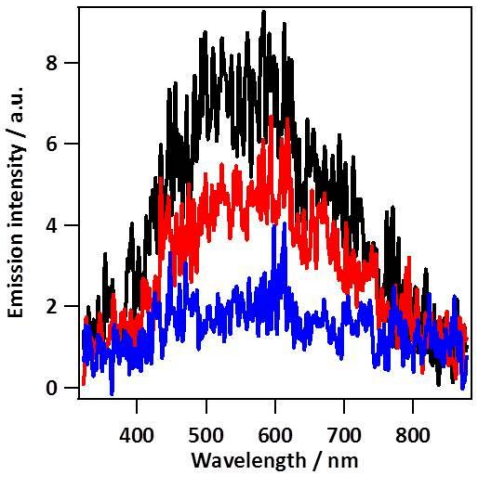

Fig.5-14 Emission spectra of water/2BE mixture. Black, red, and blue lines present emission spectra from -50 to 50 ns, from 50 to 250 ns, and 250 to 650 ns, respectively.

5-4-2 Time decay analysis

A decay curve of the emission intensity obtained with the steak camera from 490 to 750 nm is shown in Fig.5-15 (a). The decay was well fitted with two component exponential decay model. The determined time constants were 12 ns and 114 ns. Early time range from -20 to 60 ns is expanded and shown in Fig.5-15 (b). Red solid and dotted lines represent time profile of near IR pulse and expected temperature rise calculated from the pulse width, respectively. The rise of the light emission clearly delayed, indicating that the emission was not directly induced with irradiation of the near IR pulse. The result is consistent with that some of emission spots were observed at outside of the near IR irradiation region (Fig.5-4 (a)).

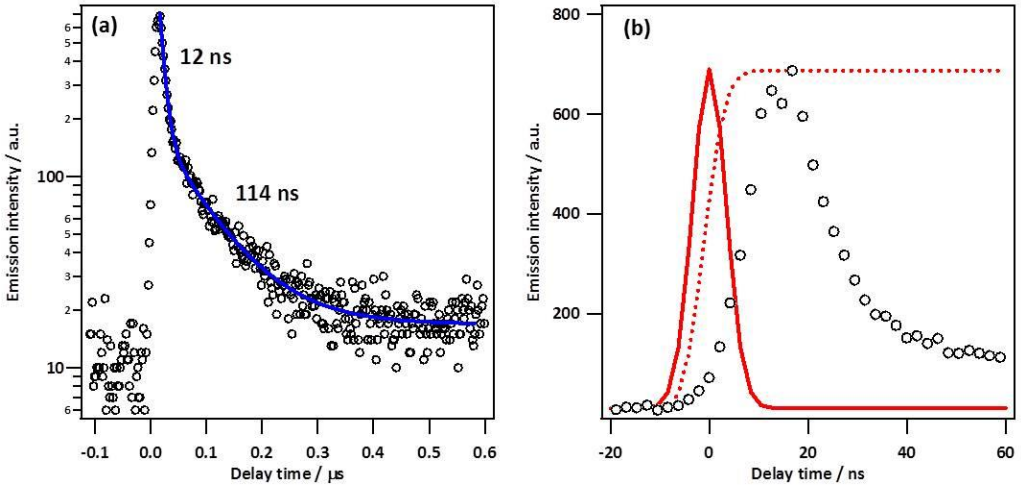

Fig.5-15 (a) Emission decay curve of water/2BE mixture obtained with the streak camera from 490 to 750 nm (open circles) and a fitting curve with two components. (b) Emission decay curve for early time range from -20 to 60 ns. Red solid and dotted lines represent time profile of near IR pulse and expected T-jump, respectively.

5-5 Mechanism of bubble formation and light emission during laser-induced T jump

In this section, mechanisms for bubble formation and light emission during laser-induced T-jump are discussed. At first, main results shown in this chapter are summarized following.

1. The light emission took place within a few hundreds nanoseconds after T-jump, and micrometer size bubbles collapsed after delay time of 50 μs. Therefore, it was found that the light emission did not occur when the micrometer size bubble collapsed, and different from well-known sonoluminescence.
2. The emission was observed even from outside of the near IR irradiation region, indicating that the light emission was not induced directly with irradiation of the near IR pulse, and something moved for 100 μm within a few hundreds nanoseconds.
3. Since the numbers of bubbles and emission spots showed positive correlation with each other,

it was speculated that these phenomena were related.

4. Bubble formation and light emission observed during laser-induced T-jump were not specific phenomena during LIPS and were observed even in pure water and completely miscible mixtures, like water/EtOH and water/EG.
5. The phenomena were observed more frequently when phase separation took place, or a mixing ratio of organic solvent was high. When salts are added into solution, the emission was also observed more frequently.
6. Blackbody radiation-like broad emission was observed after IR pulse irradiation into water/2BE mixture. Similar shape of emission spectrum was observed even in pure water. Therefore, it was suggested that the emission species was not originated in organic solvent, and due to blackbody radiation from high temperature (~ 5000 k).

From these observations, a possible explanation of mechanism of the bubble formation and the light emission is proposed. Since a near IR pulse is absorbed with a solution, gradation of temperature along the near IR pulse direction is generated. When a rapid T-jump of the solution is induced with irradiation of the near IR pulse, the rapid T-jump leads to a rapid volume expansion of the solution. Therefore, graduation of volume expansion is also generated, so that pressure wave is generated. It is conceivable that amplitude of the pressure wave depends on the magnitude of T-jump and the thermal expansion ratio of the solution. Generally, the expansion ratio of an organic solvent is larger than that of water.[15] Volume change is expected to be larger with higher composition of organic solvents. When phase separation occurs, volume change can be also large.[16] These large volume changes can cause an intense pressure wave and therefore high yield of bubbles and emission. The sound speed in water is about 1500 m/s. Thus, the pressure wave can propagate for 150 μm within 100 ns.

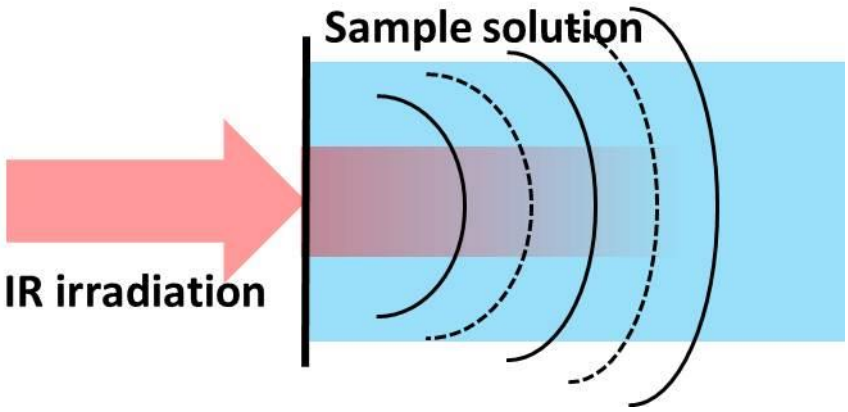

Fig.5-16 Pressure wave generation with irradiation of near IR pulse.

Moreover, some of the observations can be explained by considering nano-bubbles. It has

been reported that nanometer size bubbles exist on solid-liquid interface.[17,18] It is generally thought that nanometer size bubbles cannot exist because difference of pressure ΔP between inside and outside the bubbles become large and the bubbles are unstable as predicted by the Young-Laplace equation,

$$\Delta P = \frac{2\gamma}{r}$$

where, γ is surface tension, r is radius of bubble. However, when a small bubble adsorbs on a solid-liquid interface, an apparent radius becomes large and the bubble becomes stable (Fig.5-17(a)). This type of nano-bubbles is observed after EtOH-water exchange treatment. Another type of nano-bubble has suggested.[19] In the case of organic solvent aqueous solution, the organic solvent molecules adsorb on gas-liquid interface of nano-bubbles, and make surface tension lower, so that nanometer size bubble can exist (Fig.5-17 (b)). When the near IR pulse is irradiated or the pressure wave propagates, nano-bubbles adsorbed on a solid-liquid interface may desorb into the solution and become unstable. The unstable nano-bubbles may break down, so that temperatures inside the bubbles increase through adiabatic compression. The high temperature results in blackbody radiation. Some of the desorbed unstable nano-bubbles are stabilized by lowering surface tension with organic solvent molecules, and act as a nucleus. The nano-bubbles grow to micrometer size, so that are observed. Note that diameter of bubbles at 10 ns was estimated to be 20 nm by extrapolating from shadowgraph-imaging results. This assumption of nano-bubbles is consistent with the estimation.

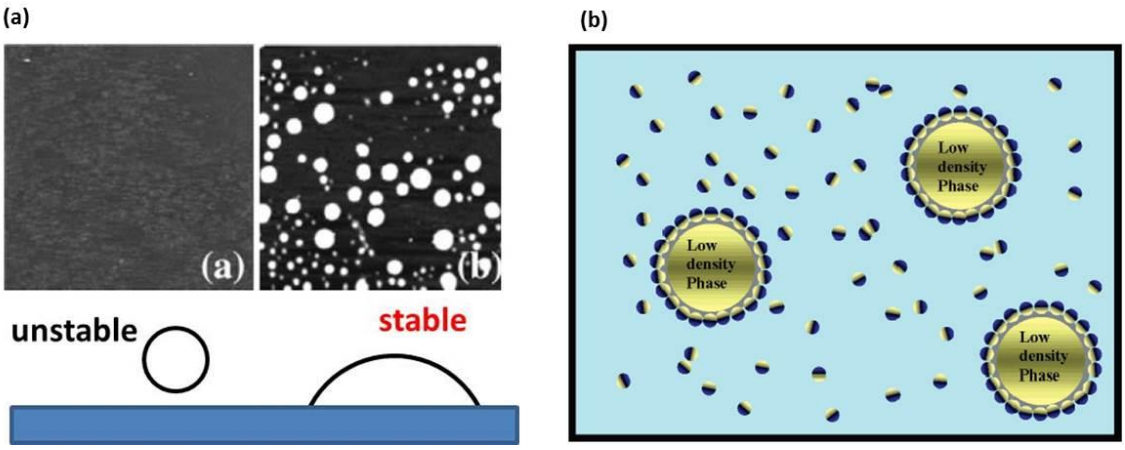

Fig.5-17 Nano-bubbles. (a) On a substrate. Ref.18. (b) In bulk solution. Ref.19.

5-6 Conclusion

In this study, following findings are reported. Bubble formation and light emission were observed during laser-induced T-jump. The phenomena were not specific in phase separation and

could be observed even in water and some complete dissolution mixture. The phenomena were observed more frequently when phase separation took place, a mixing ratio of organic solvent was high, and salts were added in solutions. Since the emission was observed from outside of the near IR pulse spot, it was indicated that the light emission was not induced directly with irradiation of the near IR pule, and something moved for 100 μm within 100 ns. Moreover, the numbers of bubbles and emission spots showed positive correlation with each other. It was therefore speculated that the phenomena were related with each other. The light emission occurred within several hundreds nanoseconds after T-jump, and micrometer size bubbles collapsed after delay time of 50 μs. Therefore, it was found the light emission was different from well-known sonoluminescence. Emission spectra were broad and liked Blackbody radiation. The similar shape of emission spectrum was observed even in pure water, suggesting that the emission species was not originated in organic solvent, and due to blackbody radiation from high temperature (~ 5000 k). From these findings, one possible mechanism of bubble formation and light emission was proposed. In the mechanism, a pressure wave is generated with laser-induced T-jump and makes nano-bubbles desorbed from a solid-liquid interface. When the desorbed unstable bubbles collapse, light emission occurs. Some of the desorbed nano-bubbles are stabilized by lowering surface tension with organic solvent molecules, and act as a nucleus. The nano-bubbles grow to micrometer size, so that are observed.

References

[1] A. Takamizawa, Doctoral Thesis, **2005**.

[2] S. Kajimoto, Doctoral Thesis, **2006**.

[3] K. Yasui, *Appl. Spec. Rev.*, **2004**, *39*, 399.

[4] M. D'Angelo, G. Onori, A. Santucci, *Chem. Phys. Lett.*, **1994**, *220*, 59.

[5] G. D'Arrigo, R. Giordano, J. Teixeira, *J. Mol. Struct.*, **1997**, *404*, 319.

[6] K. Yoshida, T. Yamaguchi, T. Otomo, M. Nagao, H. Seto, T. Takeda, *J. Mol. Liq.*, **2005**, *119*, 125.

[7] T. Arikawa, M. Nagai, K. Tanaka, *Chem. Phys. Lett.*, **2009**, *477*, 95.

[8] N. Ito, T. Fujiyama, Y. Udagawa, *Bull. Chem. Soc. Jpn.*, **1983**, *56*, 379.

[9] H. Hayashi, Y. Udagawa, *Bull. Chem. Soc. Jpn.*, **1992**, *65*, 600.

[10] T. Telgmann, U. Kaatze, *Langmuir*, **2002**, *18*, 3068.

[11] Y. Koga, *J. Phys. Chem.*, **1996**, *100*, 5172.

[12] M. Wall, M. Ashokkumar, R. Tronson, F. Grieser, *Ultrason. Sonochem.*, **1999**, *6*, 7.

[13] V. Balevicius, H. Fuess, *Phys. Chem. Chem. Phys.*, **1999**, *1*, 1507.

[14] A. Takamizawa, S. Kajimoto, J. Hobley, H. Fukumura, Q. Tran-Cong, *Phys. Rev. E*, **2003**, *68*, 020501.

[15] *KAGAKU BINRAN ver.3* (in Japanese).

[16] J. Hobley, S.Gorelik, Y. Kuge, S. Kajimoto, M. Kasuya, K. Hatanaka, H. Fukumura, *Aust. J. Chem.*, **2011**, *64*, 1.

[17] N. Ishida, T. Inoue, M. Miyahara, K. Higashitani, *Langmuir,* **2000**, *16*, 6377.

[18] X. H. Zhang, N. Maeda, V. S. J. Craig, *Langmuir,* **2006**, *22*, 5025.

[19] F. Jin, J. Ye, L. Hong, H. Lam, C. Wu, *J. Phys. Chem. B*, **2007**, *111*, 2255.

Chapter 6 Conclusion

In this study, three main topics were studied. The first was solute diffusion in water/2BE mixtures having complex and transient solution structures. FCS was employed to investigate an influence of the solution structure on amphiphilic and hydrophobic fluorescent dyes far below the LCST. The second was mesoscopic structural changes in laser-induced phase separation in water/2BE mixture. The last was mechanisms of bubble formation and light emission during laser-induced temperature jump in some binary mixture. Our findings are summarized as follows.

In Chapter 3, by FCS analysis, non-classical diffusion of the hydrophobic dye, BPDI, in water/2BE mixtures was observed, i.e. the translational diffusion of the dye unusually slowed down when water/2BE mixture was close to its critical composition but still well below the LCST. Although the apparent hydrodynamic radius of the amphiphilic dye ATTO532 remained largely unchanged with 2BE concentration, the apparent radius of BPDI almost doubled close to critical composition. In contrast, radii remained almost unaffected in water/MeOH mixtures. These observations were explained by virtue of the different affinities of the fluorescent dyes for less or more polar solvents and thus by the different interactions with local solution structures that are transiently formed in water/2BE mixtures but not in water/MeOH. Our data suggest that the presence of the hydrophobic dye BDPI stabilizes otherwise unstable 2BE micellar aggregates by at least ~10^{-4} s. In this perspective, the observed increase in the hydrodynamic radius of BPDI can be explained by a change in the size of micellar aggregates that form around BDPI, which change to bulk solvent shell structures at higher 2BE concentrations. From our experiments, it was concluded that translational diffusion of the solvated-dye depends on both the properties of the solutes and the solvent. Thus, it was found that different solutes can experience different environments even within the same solvent mixtures and even far below LCST.

In Chapter 4, first of all, a comparison with shadowgraph-, fluorescence-imaging, and light scattering are carried out. From the comparison, it was found that only shadowgraph-imaging showed a difference in the growth rates of phase domain size when the thickness of a sample was thin enough. The result may be due to the difference in the Form Factor. Next, the nanosecond SIM was developed and successfully demonstrated the observation of super-high spatial frequency. The method showed considerable potential for the detection of a periodic structure with nanosecond temporal resolution. This work is also expected as a starting point to further improvements for the purpose of visualization of the solution local structure in the future. In addition, from transient fluorescence spectrum measurements, it was found that different solutes could experience different environments during phase separation. Changes of solvent environment for hydrophobic dye, BPDI, terminated earlier than hydrophilic dye, RhB. This result is important to understand not only dynamics of LIPS but also chemical reactions during phase separation like synthesis of gold nanoparticles which is introduced in Chapter 1. For earlier delay time, light scattering was

employed to investigate dynamics of LIPS. The light scattering showed that $L(t)$ remained constant at approximately 300 nm until 10 μs after T-jump and the intensity of scattering light increased exponentially with time from 2 to 10 μs. To the best of our knowledge, this is the first report to show mesoscopic structural changes in this time region. In the early stage of spinodal decomposition, linearized Cahn–Hilliard theory predicts that the domain size remains constant while the scattering intensity increases exponentially with time. Therefore, it is clearly indicated that the early stage of LIPS in the water/2BE mixture lasted for 10 μs. The results also showed that linearized Cahn–Hilliard theory is applicable to the early stage of LIPS with a deep quench depth. It is expected that further elaborate experiments will examine effects of asymmetry of coexistent curve. Based on the observation and the previous Raman studies, it is indicated that the formation of new phases proceeds by increasing density fluctuation of the mesoscopic structure, that is, 2BE micellar aggregate. Although fluctuations of molecular density have been considered in study on phase separation so far, our study strongly indicate that we have to consider fluctuations of mesoscopic structures like 2BE micellar aggregates instead of molecular density. It is already known that there is a hierarchical structure in water/2BE mixture as described in chapter 1. However, this study revealed that the hierarchical structure is important even in dynamics of phase separation.

In Chapter 5, mechanisms of bubble formation and light emission during laser-induced T-jump were discussed. It was found that the phenomena were not specific in phase separation and could be observed even in water and some complete dissolution mixture. The phenomena were observed more frequently when phase separation took place, a mixing ratio of organic solvent was high, and salts were added in solutions. Moreover, the numbers of bubbles and emission spots showed positive correlation with each other. It was therefore speculated that the phenomena were related with each other. The light emission occurred within several hundreds nanoseconds after T-jump, and micrometer size bubbles collapsed after delay time of 50 μs. Therefore, it was found the light emission was different from well-known sonoluminescence. Since the emission was observed from outside of the near IR irradiation region and the rise of the light emission delayed around 15 ns, it was indicated that the light emission was not induced directly with irradiation of the near IR pulse. Emission spectra were broad and liked Blackbody radiation. The similar shape of emission spectrum was observed even in pure water, suggesting that the emission species was not originated in organic solvent, and due to blackbody radiation from high temperature (~ 5000 k). From these findings, one possible mechanism of bubble formation and light emission was proposed. In the mechanism, a pressure wave is generated with laser-induced T-jump and makes nano-bubbles desorbed from a solid-liquid interface. When the desorbed unstable bubbles collapse, light emission occurs. Some of the desorbed nano-bubbles are stabilized by lowering surface tension with organic solvent molecules, and act as a nucleus. The nano-bubbles grow to micrometer size, so that are observed.

Acknowledgements

I would like to sincerely express my gratitude to my mentor, Professor Hiroshi Fukumura, Professor of Organic Physical Chemistry laboratory in Grduate School of Science, Tohoku University. From his kind guidance, I gained not only knowledge and experience in scientific research, but also spiritual inspiration and encouragement. I am also very thankful to Professor Dirk-Peter Herten as my supervisor, Heidelberg University, for his great support.

I deeply appreciate Assistant Professor Shinji Kajimoto's great help and encouragement. His extremely careful attitude impresses and influences me a lot. I also wish to say thanks to Associate Professor Yutaka Shibata and former Assistant Professor Noriko Horimoto, for their sustained help and support. I am grateful to my phase separation group members, Mr. Daisuke Shirasawa, Ms. Ayaka Mori, Mr. Kenta Kitabatake and so on, for their kind help and discussion. I also wish to thank all lab members, Ms. Chio Ishida, Mr. Yasuhiko Fujita and Mr. Hikaru Sotome so on. Because of you, I enjoyed a quite happy time. Last but not the least, I am really grateful to my family and friends, who are supporting me all the time. Even though I am separated from you, I could always feel you just beside me and encouraging me.

Shuichi Toyouchi

August. 2014

Appendix A. M-file for calculation of power spectrum

```
%% M-file for calculation of power spectrum
clear;
ImageSize=512;
DataCutNum=10;
BGNum=20;
Num=20;
Xpos=256;
Ypos=257;
NumRI=zeros(1,4);
NumRI(1)=round(((1-(ImageSize/2+1))^2+(1-(ImageSize/2+1))^2)^(1/2))+1;
NumRI(2)=round(((1-(ImageSize/2+1))^2+(ImageSize-(ImageSize/2+1))^2)^(1/2))+1;
NumRI(3)=round(((ImageSize-(ImageSize/2+1))^2+(1-(ImageSize/2+1))^2)^(1/2))+1;
NumRI(4)=round(((ImageSize-(ImageSize/2+1))^2+(ImageSize-(ImageSize/2+1))^2)^(1/2))+1;
NumRI=max(NumRI);
SF=0:(NumRI-1);

%% mask 作成用 m-file
ImageCenterX=257;
ImageCenterY=257;
MaskSize=150;
MaskEdgeSize=100;
Mask=ones(ImageSize);
for x=1:ImageSize;
      for y=1:ImageSize;
            if ((x-ImageCenterX)^2+(y-ImageCenterY)^2)^(0.5)<MaskSize;
                  Mask(x,y)=1;
            Elseif                        ((x-ImageCenterX)^2+(y-ImageCenterY)^2)^(0.5)>=MaskSize          &&
((x-ImageCenterX)^2+(y-ImageCenterY)^2)^(0.5)<MaskSize+MaskEdgeSize;
    Mask(x,y)=0.5+0.5*cos(2*pi*(((x-ImageCenterX)^2+(y-ImageCenterY)^2)^(0.5)-MaskSize)/(2*MaskEdgeSize));
            else
                  Mask(x,y)=0;
            end
      end
end
```

```
%% バックグラウンド
% バックグラウンド作成
BG1=zeros(1024,1026);
BG=zeros(ImageSize);
for BGii=1:BGNum;
    BG2=strcat('F:¥matlab file¥background¥background for image¥bg_', num2str(BGii), '.asc');
    BG1=double(dlmread(BG2));
    BG1=BG1((Xpos-ImageSize/2+1):(Xpos+ImageSize/2),(Ypos-ImageSize/2+1):(Ypos+ImageSize/2));
    BG=BG+BG1;
end
BG=BG/BGNum;

%% ベース
Base1=zeros(1024,1026);
Base3=zeros(ImageSize);
Base=zeros(ImageSize);
FFTBase=zeros(ImageSize);
RIBase=zeros(1,NumRI);
counter=zeros(1,NumRI);

for Baseii=1:Num;
    Base2=strcat('F:¥matlab file¥image¥b_', num2str(Baseii), '.asc');
    Base1=double(dlmread(Base2));
    Base1=abs(Base1((Xpos-ImageSize/2+1):(Xpos+ImageSize/2),(Ypos-ImageSize/2+1):(Ypos+ImageSize/2))-BG);
    Base1=Base1.*Mask;
    Base=Base+Base1;
    Base3=log10(abs(fftshift(fft2(Base1))));
    %Base3=abs(fftshift(fft2(Base1)));
    FFTBase=FFTBase+Base3;
end

Base=Base/Num;
FFTBase=FFTBase/Num;

for kx = 1:ImageSize
    for ky = 1:ImageSize
```

```
            RIBase(round(((kx-(ImageSize/2+1))^2+(ky-(ImageSize/2+1))^2)^(1/2))+1)                                    =
RIBase(round(((kx-(ImageSize/2+1))^2+(ky-(ImageSize/2+1))^2)^(1/2))+1) + FFTBase(kx,ky);
            counter(round(((kx-(ImageSize/2+1))^2+(ky-(ImageSize/2+1))^2)^(1/2))+1)                                   =
counter(round(((kx-(ImageSize/2+1))^2+(ky-(ImageSize/2+1))^2)^(1/2))+1) + 1;
      end
end

%% イメージ
Image1=zeros(1024,1026);
Image3=zeros(ImageSize);
Image=zeros(ImageSize);
FFTImage=zeros(ImageSize);
normRIImage=zeros(1,NumRI);
RI=zeros(1,NumRI);
SRI=zeros(NumRI,Num);

for Imageii=1:Num;
      Image2=strcat('F:¥matlab file¥image¥a_', num2str(Imageii), '.asc');
      Image1=double(dlmread(Image2));
      Image1=abs(Image1((Xpos-ImageSize/2+1):(Xpos+ImageSize/2),(Ypos-ImageSize/2+1):(Ypos+ImageSize/2))-BG);
      Image1=Image1.*Mask;
      Image3=log10(abs(fftshift(fft2(Image1))));
      %Image3=abs(fftshift(fft2(Image1)));
      FFTImage=FFTImage+Image3;
      counter=zeros(1,NumRI);
      RIImage1=zeros(1,NumRI);
      normRIImage1=zeros(1,NumRI);
      RI1=zeros(1,NumRI);

      for kx = 1:ImageSize
            for ky = 1:ImageSize
                  RIImage1(round(((kx-(ImageSize/2+1))^2+(ky-(ImageSize/2+1))^2)^(1/2))+1)                            =
RIImage1(round(((kx-(ImageSize/2+1))^2+(ky-(ImageSize/2+1))^2)^(1/2))+1) + Image3(kx,ky);
                  counter(round(((kx-(ImageSize/2+1))^2+(ky-(ImageSize/2+1))^2)^(1/2))+1)                           =
counter(round(((kx-(ImageSize/2+1))^2+(ky-(ImageSize/2+1))^2)^(1/2))+1) + 1;
            end
```

```
        end

        RIImage1=RIImage1./counter;
        normRIImage1=RIImage1/RIImage1(1)*RIBase(1);
        normRIImage=normRIImage+normRIImage1;
        RI1=normRIImage1-RIBase;
        eval(['RI_',num2str(Imageii),'=RI1;']);
        RI=RI+RI1;
        SRI(:,Imageii)=RI1;
end

Image=Image1;
FFTImage=FFTImage/Num;
normRIImage=normRIImage/Num;
RI=RI/Num;
RI=RI.';

%%
figure(1);
subplot(2,2,1);imagesc(Base);colormap(gray);
subplot(2,2,2);imagesc(Image);colormap(gray);
subplot(2,2,3);imagesc(FFTBase);colormap(jet);
subplot(2,2,4);imagesc(FFTImage);colormap(jet);
figure(2);hold off;
subplot(1,1,1);plot(SF,RIBase,'b','LineWidth',2);hold on;
subplot(1,1,1);plot(SF,normRIImage,'r','LineWidth',2);
grid on;
hold off;
figure(3);
plot(SF,RI,'r','LineWidth',2);

%% Igor にデータを移すための行列作成
IgorOutput=[SF.', RIBase.', normRIImage.', RI, SRI];
IgorOutput=IgorOutput(1:NumRI-DataCutNum,:);
imwrite(uint8(round((Base-min(Base(:)))./(max(Base(:))-min(Base(:)))*256)),'F:¥matlab file¥image¥data¥Base.tif');
imwrite(uint8(round((Image-min(Image(:)))./(max(Image(:))-min(Image(:)))*256)),'F:¥matlab
```

```
file¥image¥data¥Image.tif');
imwrite(uint8(round((FFTBase-min(FFTBase(:)))./(max(FFTBase(:))-min(FFTBase(:)))*256)),'F:¥matlab
file¥image¥data¥FFTBase.tif');
imwrite(uint8(round((FFTImage-min(FFTImage(:)))./(max(FFTImage(:))-min(FFTImage(:)))*256)),'F:¥matlab
file¥image¥data¥FFTImage.tif');
dlmwrite('F:¥matlab file¥image¥data¥IgorOutput_Phase.asc',IgorOutput);
% End of file
```

Appendix B. M-file for determination of the number and size of bubbles

```
%% 気泡の解析用 m-file
clear;
BaseNumber=20; %ベースライン画像数
ImageNumber=20; %気泡画像数
N=10;%気泡サイズ最少閾値
M=500; %気泡サイズ最大閾値

%% ベースライン用画像の数入力
% ベースライン作成
Base1=zeros(512,514);
Base3=zeros(512);
Base=zeros(512);
for Baseii=1:BaseNumber;
    Base2=strcat('F:¥matlab file¥base¥bubble base¥b_', num2str(Baseii), '.asc');
    Base1=double(dlmread(Base2));
    Base1=Base1(:,2:513);
    Base3=Base3+Base1;
end
Base=Base3/BaseNumber;

figure(1);
imagesc(Base);colormap(gray);axis image;%Base 作成 ベースラインには遅延時間 100n 秒画像を使用

%% 閾値の設定
A=double(dlmread('F:¥matlab file¥bubble¥a_1.asc'));
A=(-1)*(A(:,2:513)-Base);
figure(2);
hist(A,100);
Threshold=input('シグナルの閾値: Threshold = ');

%% 気泡画像の数入力
% 気泡画像解析
BU1=zeros(512,514);
number_bubble=zeros(ImageNumber,1);
CirclePerimeter=zeros(0);
```

```
CenterBubble=zeros(512);
for BUii=1:ImageNumber;
    BU2=strcat('F:¥matlab file¥bubble¥a_', num2str(BUii), '.asc');
    BU3=strcat('F:¥matlab file¥bubble¥data¥bubble_', num2str(BUii), '.tif');
    BU1=double(dlmread(BU2));
    BU1=(-1)*(BU1(:,2:513)-Base)>Threshold;
    figure(3);
    imagesc(BU1);colormap(gray);axis image;
    eval(['bubble_',num2str(BUii),'=BU1;']);
    pause(0.1);
    imwrite(BU1,BU3);
if max(BU1)<1;
    number_bubble(BUii)=0;
    CirclePerimeter=[CirclePerimeter;zeros(0)];
else
    a = BU1;
    msr = measure(a,[],'Perimeter',[],Inf,0,0); % 円周を求める関数(周囲の長さ)
    n1=msr.Perimeter(1,:); % 円周
    n1=n1(:); % 転置行列計算
    n2=numel(n1); % 行列の要素数(気泡数)
    n3=0; % 気泡数の初期化
    msr = measure(a,[],'Center',[],Inf,0,0); % 中心を求める
    n4=msr.Center(1,:); % 中心 X
    n5=msr.Center(2,:); % 中心 Y
    for x=1:n2; % 閾値以外の気泡の除去
        if   N < n1(x) && n1(x) < M;
            n3=n3+1;
            CirclePerimeter=[CirclePerimeter;n1(x)];
            CenterBubble(round(n4(x)),round(n5(x)))=CenterBubble(round(n4(x)),round(n5(x)))+100;
        end
    end
    number_bubble(BUii)=n3;
end
if number_bubble(BUii)<1; % 閾値以内の気泡が無かった場合
    CirclePerimeter=[CirclePerimeter;zeros(0)];
end
```

```
end
figure(4);
imagesc(CenterBubble); axis image; colormap gray;
imwrite(CenterBubble,'F:¥matlab file¥bubble¥data¥CenterBubble.tif')

%% ピクセルからの meter 単位へ変換、直径、面積、体積の計算
Diameter=CirclePerimeter/pi;
Diameter=Diameter*593.22*10^-9;
Volume=4/3*pi*(Diameter/2).^3;
b_bubble=[Diameter,Volume];
WavestatsBubble=zeros(1,7);
WavestatsBubble(1)=mean(number_bubble);
WavestatsBubble(2)=std(number_bubble);
WavestatsBubble(3)=mean(Diameter);
WavestatsBubble(4)=std(Diameter);
WavestatsBubble(5)=mean(Volume);
WavestatsBubble(6)=std(Volume);
WavestatsBubble(7)=WavestatsBubble(1)*WavestatsBubble(5);
WavestatsBubble=WavestatsBubble(:);

%% number_bubble と b_bubble、wavestats の変数エディタ表示
openvar('number_bubble');
openvar('b_bubble');
openvar('WavestatsBubble');
dlmwrite('F:¥matlab file¥bubble¥data¥IgorOutput_bubble_1.asc',number_bubble);
dlmwrite('F:¥matlab file¥bubble¥data¥IgorOutput_bubble_2.asc',b_bubble);
dlmwrite('F:¥matlab file¥bubble¥data¥IgorOutput_bubble_3.asc',WavestatsBubble);
% End of file
```

Appendix C. M-file for counting of the number of emission spots

```
%% 発光解析用　M-file
clear;
BGNumber=1; %気泡発光ベースライン画像数
EMImageNumber=20; %気泡発光画像

%% バックグラウンド作成
BG1=zeros(512,514);
BG3=zeros(512);
BG=zeros(512);
for BGii=2:BGNumber+1;
    BG2=strcat('F:¥matlab file¥background¥background for bubble¥eb_', num2str(BGii), '.asc');
    BG1=double(dlmread(BG2));
    BG1=BG1(:,2:513);
    BG1(1,:)=BG1(2,:);
    BG3=BG3+BG1;
end
BG=BG3/BGNumber;
figure(1);
imagesc(BG);colormap(gray);colorbar;axis image;
% 発光閾値の決定
figure(2);
hist(BG,500);
Threshold=input('発光強度の閾値: Threshold = ');

%% 輝点画像の数入力
% 気泡画像解析
EM1=zeros(512,514);
% 気泡の数とサイズを求める
number_spots=zeros(EMImageNumber,1);
EMTotal=zeros(512);
CenterEmission=zeros(512);
for EMii=1:EMImageNumber;
    EM2=strcat('F:¥matlab file¥emission¥e_', num2str(EMii), '.asc');
    EM3=strcat('F:¥matlab file¥emission¥data¥emission_', num2str(EMii), '.tif');
    EM1=double(dlmread(EM2));
```

```
        EM1=EM1(:,2:513)>Threshold;
        figure(3)
        imagesc(EM1);colormap(gray);axis image;
        eval(['emission_',num2str(EMii),'=EM1;']);
        pause(0.1);
        EMTotal=EMTotal+EM1;
        imwrite(EM1,EM3);
if max(EM1)<1;
        number_spots(EMii)=0;
        %EI=[EI;zeros(0)];
else
        a = EM1;
        msr = measure(a,[],'Size',[],Inf,0,0);
        number_spots(EMii)=numel(msr.ID);
end
end
imwrite(CenterEmission,'F:¥matlab file¥emission¥data¥CenterEmission.tif')
figure(4)
imagesc(EMTotal);colormap(gray);axis image;
figure(5)
imagesc(CenterEmission); colormap(gray); axis image;

%% 輝点の統計数値
WavestatsSpots=zeros(1,2);
WavestatsSpots(1)=mean(number_spots);
WavestatsSpots(2)=std(number_spots);

%% number_spots の変数エディタ表示
openvar('number_spots');
openvar('WavestatsSpots');
dlmwrite('F:¥matlab file¥emission¥data¥IgorOutput_emission_1.asc',number_spots);
dlmwrite('F:¥matlab file¥emission¥data¥IgorOutput_emission_2.asc',WavestatsSpots);
imwrite(uint8(round((EMTotal-min(EMTotal(:))./(max(EMTotal(:))-min(EMTotal(:)))*255)),'F:¥matlab
file¥emission¥data¥emission_total.tif');
imwrite(uint8(EMTotal),'F:¥matlab file¥emission¥data¥emission_total.tif');
```

```
% End of file
```

Appendix D. M-file for nanosecond SIM analysis

```
%% 構造化照明データ解析用 M-file
clear;
ImageSize=1024;
DataCutNum=10;
BGNum=20;
Num=20;
PeakPosition_y=513;
PeakPosition_x=348;
Xpos=512;
Ypos=513;
NumRISIM=zeros(1,4);
NumRISIM(1)=round(((1-PeakPosition_x)^2+(1-PeakPosition_y)^2)^(1/2))+1;
NumRISIM(2)=round(((1-PeakPosition_x)^2+(ImageSize-PeakPosition_y)^2)^(1/2))+1;
NumRISIM(3)=round(((ImageSize-PeakPosition_x)^2+(1-PeakPosition_y)^2)^(1/2))+1;
NumRISIM(4)=round(((ImageSize-PeakPosition_x)^2+(ImageSize-PeakPosition_y)^2)^(1/2))+1;
NumRISIM=max(NumRISIM);
SFRISIM=0:(NumRISIM-1);

%% mask 作成用 m-file
ImageCenterX=480;
ImageCenterY=500;
MaskSize=310;
MaskEdgeSize=200;
Mask=ones(ImageSize);
for x=1:ImageSize;
    for y=1:ImageSize;
        if ((x-ImageCenterX)^2+(y-ImageCenterY)^2)^(0.5)<MaskSize;
            Mask(x,y)=1;
        elseif ((x-ImageCenterX)^2+(y-ImageCenterY)^2)^(0.5)>=MaskSize &&
((x-ImageCenterX)^2+(y-ImageCenterY)^2)^(0.5)<MaskSize+MaskEdgeSize;

Mask(x,y)=0.5+0.5*cos(2*pi*(((x-ImageCenterX)^2+(y-ImageCenterY)^2)^(0.5)-MaskSize)/(2*MaskEdgeSize));
        else
            Mask(x,y)=0;
        end
```

```
    end
end

%% バックグラウンド
% バックグラウンド作成
BG1=zeros(1024,1026);
BG=zeros(ImageSize);
for BGii=1:BGNum;
    BG2=strcat('F:¥matlab file¥background¥background for image¥bg_', num2str(BGii), '.asc');
    BG1=double(dlmread(BG2));
    BG1=BG1((Xpos-ImageSize/2+1):(Xpos+ImageSize/2),(Ypos-ImageSize/2+1):(Ypos+ImageSize/2));
    BG=BG+BG1;
end
BG=BG/BGNum;

%% 均一照明ベースライン
Base1=zeros(1024,1026);
Base3=zeros(ImageSize);
Base=zeros(ImageSize);
FFTBase=zeros(ImageSize);
RIBase=zeros(1,NumRISIM);
counterSIM=zeros(1,NumRISIM);
for Baseii=1:Num;
    Base2=strcat('F:¥matlab file¥image¥b_', num2str(Baseii), '.asc');
    Base1=double(dlmread(Base2));
    Base1=abs(Base1((Xpos-ImageSize/2+1):(Xpos+ImageSize/2),(Ypos-ImageSize/2+1):(Ypos+ImageSize/2))-BG);
    Base1=Base1.*Mask;
    Base=Base+Base1;
    Base3=log10(abs(fftshift(fft2(Base1))));
    %Base3=abs(fftshift(fft2(Base1)));
    FFTBase=FFTBase+Base3;
end
Base=Base/Num;
FFTBase=FFTBase/Num;
for kx=1:ImageSize;
        for ky=1:ImageSize;
```

```
                if ((kx-513)^2+(ky-513)^2)^(0.5)<50;
                RIBase(round(((kx-PeakPosition_x)^2+(ky-PeakPosition_y)^2)^(1/2))+1)                    =
RIBase(round(((kx-PeakPosition_x)^2+(ky-PeakPosition_y)^2)^(1/2))+1) + 0;
                counterSIM(round(((kx-PeakPosition_x)^2+(ky-PeakPosition_y)^2)^(1/2))+1)                =
counterSIM(round(((kx-PeakPosition_x)^2+(ky-PeakPosition_y)^2)^(1/2))+1) + 0;
                %elseif ((kx-647)^2+(ky-517)^2)^(0.5)<25;
                %RIBase(round(((kx-PeakPosition_x)^2+(ky-PeakPosition_y)^2)^(1/2))+1)                   =
RIBase(round(((kx-PeakPosition_x)^2+(ky-PeakPosition_y)^2)^(1/2))+1) + 0;
                %counterSIM(round(((kx-PeakPosition_x)^2+(ky-PeakPosition_y)^2)^(1/2))+1)               =
counterSIM(round(((kx-PeakPosition_x)^2+(ky-PeakPosition_y)^2)^(1/2))+1) + 0;
                %elseif ((kx-379)^2+(ky-511)^2)^(0.5)<10;
                %RIBase(round(((kx-PeakPosition_x)^2+(ky-PeakPosition_y)^2)^(1/2))+1)                   =
RIBase(round(((kx-PeakPosition_x)^2+(ky-PeakPosition_y)^2)^(1/2))+1) + 0;
                %counterSIM(round(((kx-PeakPosition_x)^2+(ky-PeakPosition_y)^2)^(1/2))+1)               =
counterSIM(round(((kx-PeakPosition_x)^2+(ky-PeakPosition_y)^2)^(1/2))+1) + 0;
                %elseif ((kx-647)^2+(ky-515)^2)^(0.5)<10;
                %RIBase(round(((kx-PeakPosition_x)^2+(ky-PeakPosition_y)^2)^(1/2))+1)                   =
RIBase(round(((kx-PeakPosition_x)^2+(ky-PeakPosition_y)^2)^(1/2))+1) + 0;
                %counterSIM(round(((kx-PeakPosition_x)^2+(ky-PeakPosition_y)^2)^(1/2))+1)               =
counterSIM(round(((kx-PeakPosition_x)^2+(ky-PeakPosition_y)^2)^(1/2))+1) + 0;
                else
                RIBase(round(((kx-PeakPosition_x)^2+(ky-PeakPosition_y)^2)^(1/2))+1)                    =
RIBase(round(((kx-PeakPosition_x)^2+(ky-PeakPosition_y)^2)^(1/2))+1) + FFTBase(kx,ky);
                counterSIM(round(((kx-PeakPosition_x)^2+(ky-PeakPosition_y)^2)^(1/2))+1)                =
counterSIM(round(((kx-PeakPosition_x)^2+(ky-PeakPosition_y)^2)^(1/2))+1) + 1;
                end
            end
        end
        RIBase=RIBase./counterSIM;
        mean(RIBase(:,600:760));
        RIBase=RIBase-ans;

%% 構造化照明ベースライン
SIMBase1=zeros(1024,1026);
SIMBase3=zeros(ImageSize);
SIMBase=zeros(ImageSize);
```

```
FFTSIMBase=zeros(ImageSize);
RISIMBase=zeros(1,NumRISIM);
counterSIM=zeros(1,NumRISIM);
for SIMBaseii=1:Num;
    SIMBase2=strcat('F:¥matlab file¥image¥SIMb_', num2str(SIMBaseii), '.asc');
    SIMBase1=double(dlmread(SIMBase2));
SIMBase1=abs(SIMBase1((Xpos-ImageSize/2+1):(Xpos+ImageSize/2),(Ypos-ImageSize/2+1):(Ypos+ImageSize/2))-BG);
    SIMBase1=SIMBase1.*Mask;
    SIMBase=SIMBase+SIMBase1;
    SIMBase3=log10(abs(fftshift(fft2(SIMBase1))));
    %SIMBase3=abs(fftshift(fft2(SIMBase1)));
    FFTSIMBase=FFTSIMBase+SIMBase3;
end
SIMBase=SIMBase/Num;
FFTSIMBase=FFTSIMBase/Num;
for kx=1:ImageSize;
        for ky=1:ImageSize;
            if ((kx-513)^2+(ky-513)^2)^(0.5)<50;
            RISIMBase(round(((kx-PeakPosition_x)^2+(ky-PeakPosition_y)^2)^(1/2))+1)                =
RISIMBase(round(((kx-PeakPosition_x)^2+(ky-PeakPosition_y)^2)^(1/2))+1) + 0;
            counterSIM(round(((kx-PeakPosition_x)^2+(ky-PeakPosition_y)^2)^(1/2))+1)               =
counterSIM(round(((kx-PeakPosition_x)^2+(ky-PeakPosition_y)^2)^(1/2))+1) + 0;
            elseif ((kx-678)^2+(ky-513)^2)^(0.5)<25;
            RISIMBase(round(((kx-PeakPosition_x)^2+(ky-PeakPosition_y)^2)^(1/2))+1)                =
RISIMBase(round(((kx-PeakPosition_x)^2+(ky-PeakPosition_y)^2)^(1/2))+1) + 0;
            counterSIM(round(((kx-PeakPosition_x)^2+(ky-PeakPosition_y)^2)^(1/2))+1)               =
counterSIM(round(((kx-PeakPosition_x)^2+(ky-PeakPosition_y)^2)^(1/2))+1) + 0;
            %elseif ((kx-379)^2+(ky-511)^2)^(0.5)<10;
            %RISIMBase(round(((kx-PeakPosition_x)^2+(ky-PeakPosition_y)^2)^(1/2))+1)               =
RISIMBase(round(((kx-PeakPosition_x)^2+(ky-PeakPosition_y)^2)^(1/2))+1) + 0;
            %counterSIM(round(((kx-PeakPosition_x)^2+(ky-PeakPosition_y)^2)^(1/2))+1)              =
counterSIM(round(((kx-PeakPosition_x)^2+(ky-PeakPosition_y)^2)^(1/2))+1) + 0;
            %elseif ((kx-647)^2+(ky-515)^2)^(0.5)<10;
            %RISIMBase(round(((kx-PeakPosition_x)^2+(ky-PeakPosition_y)^2)^(1/2))+1)               =
RISIMBase(round(((kx-PeakPosition_x)^2+(ky-PeakPosition_y)^2)^(1/2))+1) + 0;
            %counterSIM(round(((kx-PeakPosition_x)^2+(ky-PeakPosition_y)^2)^(1/2))+1)              =
```

```
counterSIM(round(((kx-PeakPosition_x)^2+(ky-PeakPosition_y)^2)^(1/2))+1) + 0;
                else
                RISIMBase(round(((kx-PeakPosition_x)^2+(ky-PeakPosition_y)^2)^(1/2))+1)                =
RISIMBase(round(((kx-PeakPosition_x)^2+(ky-PeakPosition_y)^2)^(1/2))+1) + FFTSIMBase(kx,ky);
                counterSIM(round(((kx-PeakPosition_x)^2+(ky-PeakPosition_y)^2)^(1/2))+1)                =
counterSIM(round(((kx-PeakPosition_x)^2+(ky-PeakPosition_y)^2)^(1/2))+1) + 1;
                end
            end
        end
        RISIMBase=RISIMBase./counterSIM;
        mean(RISIMBase(:,600:760));
        RISIMBase=RISIMBase-ans;

%% ベース規格化
normRISIMBase=zeros(1,NumRISIM);
subRISIMBase=zeros(1,NumRISIM);
normRISIMBase=RISIMBase/mean(RISIMBase(:,100:250))*mean(RIBase(:,100:250));
subRISIMBase=normRISIMBase-RIBase;

%% 均一照明イメージ
Image1=zeros(1024,1026);
Image3=zeros(ImageSize);
Image=zeros(ImageSize);
FFTImage=zeros(ImageSize);
RIImage=zeros(1,NumRISIM);%構造化照明の条件で、第一次ピーク中心での積算
for Imageii=1:Num;
        Image2=strcat('F:¥matlab file¥image¥a_', num2str(Imageii), '.asc');
        Image1=double(dlmread(Image2));
        Image1=abs(Image1((Xpos-ImageSize/2+1):(Xpos+ImageSize/2),(Ypos-ImageSize/2+1):(Ypos+ImageSize/2))-BG);
        Image1=Image1.*Mask;
        Image3=log10(abs(fftshift(fft2(Image1))));
        %Image3=abs(fftshift(fft2(Image1)));
        FFTImage=FFTImage+Image3;
        counterSIM=zeros(1,NumRISIM);
        RIImage1=zeros(1,NumRISIM);
```

```
    for kx=1:ImageSize;
        for ky=1:ImageSize;
            if ((kx-513)^2+(ky-513)^2)^(0.5)<50;
            RIImage1(round(((kx-PeakPosition_x)^2+(ky-PeakPosition_y)^2)^(1/2))+1)                    =
RIImage1(round(((kx-PeakPosition_x)^2+(ky-PeakPosition_y)^2)^(1/2))+1) + 0;
            counterSIM(round(((kx-PeakPosition_x)^2+(ky-PeakPosition_y)^2)^(1/2))+1)                  =
counterSIM(round(((kx-PeakPosition_x)^2+(ky-PeakPosition_y)^2)^(1/2))+1) + 0;
            %elseif ((kx-647)^2+(ky-517)^2)^(0.5)<25;
            %RIImage1(round(((kx-PeakPosition_x)^2+(ky-PeakPosition_y)^2)^(1/2))+1)                   =
RIImage1(round(((kx-PeakPosition_x)^2+(ky-PeakPosition_y)^2)^(1/2))+1) + 0;
            %counterSIM(round(((kx-PeakPosition_x)^2+(ky-PeakPosition_y)^2)^(1/2))+1)                 =
counterSIM(round(((kx-PeakPosition_x)^2+(ky-PeakPosition_y)^2)^(1/2))+1) + 0;
            %elseif ((kx-379)^2+(ky-511)^2)^(0.5)<10;
            %RIImage1(round(((kx-PeakPosition_x)^2+(ky-PeakPosition_y)^2)^(1/2))+1)                   =
RIImage1(round(((kx-PeakPosition_x)^2+(ky-PeakPosition_y)^2)^(1/2))+1) + 0;
            %counterSIM(round(((kx-PeakPosition_x)^2+(ky-PeakPosition_y)^2)^(1/2))+1)                 =
counterSIM(round(((kx-PeakPosition_x)^2+(ky-PeakPosition_y)^2)^(1/2))+1) + 0;
            %elseif ((kx-647)^2+(ky-515)^2)^(0.5)<10;
            %RIImage1(round(((kx-PeakPosition_x)^2+(ky-PeakPosition_y)^2)^(1/2))+1)                   =
RIImage1(round(((kx-PeakPosition_x)^2+(ky-PeakPosition_y)^2)^(1/2))+1) + 0;
            %counterSIM(round(((kx-PeakPosition_x)^2+(ky-PeakPosition_y)^2)^(1/2))+1)                 =
counterSIM(round(((kx-PeakPosition_x)^2+(ky-PeakPosition_y)^2)^(1/2))+1) + 0;
            else
            RIImage1(round(((kx-PeakPosition_x)^2+(ky-PeakPosition_y)^2)^(1/2))+1)                    =
RIImage1(round(((kx-PeakPosition_x)^2+(ky-PeakPosition_y)^2)^(1/2))+1) + Image3(kx,ky);
            counterSIM(round(((kx-PeakPosition_x)^2+(ky-PeakPosition_y)^2)^(1/2))+1)                  =
counterSIM(round(((kx-PeakPosition_x)^2+(ky-PeakPosition_y)^2)^(1/2))+1) + 1;
            end
        end
    end
    RIImage1=RIImage1./counterSIM;
    mean(RIImage1(:,600:760));
    RIImage1=RIImage1-ans;
    eval(['RIImage_',num2str(Imageii),'=RIImage1;']); %各画像での Image での割り算を構造化照明のスポット
周りに積算したもの
    RIImage=RIImage+RIImage1;
```

```
end
Image=Image1;
FFTImage=FFTImage/Num;
RIImage=RIImage/Num;

%% 構造化照明イメージ
SIMImage1=zeros(1024,1026);
SIMImage3=zeros(ImageSize);
SIMImage=zeros(ImageSize);
FFTSIMImage=zeros(ImageSize);
normRISIMImage=zeros(1,NumRISIM);%構造化照明の条件で、第一次ピーク中心での積算
subRISIMImage=zeros(1,NumRISIM);
RI=zeros(1,NumRISIM);
SRI=zeros(NumRISIM,Num);
for SIMImageii=1:Num;
    SIMImage2=strcat('F:¥matlab file¥image¥SIMa_', num2str(SIMImageii), '.asc');
    SIMImage1=double(dlmread(SIMImage2));
SIMImage1=abs(SIMImage1((Xpos-ImageSize/2+1):(Xpos+ImageSize/2),(Ypos-ImageSize/2+1):(Ypos+ImageSize/2))-B
G);
    SIMImage1=SIMImage1.*Mask;
    SIMImage3=log10(abs(fftshift(fft2(SIMImage1))));
    %SIMImage3=abs(fftshift(fft2(SIMImage1)));
    FFTSIMImage=FFTSIMImage+SIMImage3;
    counterSIM=zeros(1,NumRISIM);
    RISIMImage1=zeros(1,NumRISIM);
    normRISIMImage1=zeros(1,NumRISIM);
    subRISIMImage1=zeros(1,NumRISIM);
    RI1=zeros(1,NumRISIM);
    for kx=1:ImageSize;
        for ky=1:ImageSize;
            if ((kx-513)^2+(ky-513)^2)^(0.5)<50;
            RISIMImage1(round(((kx-PeakPosition_x)^2+(ky-PeakPosition_y)^2)^(1/2))+1)                =
RISIMImage1(round(((kx-PeakPosition_x)^2+(ky-PeakPosition_y)^2)^(1/2))+1) + 0;
            counterSIM(round(((kx-PeakPosition_x)^2+(ky-PeakPosition_y)^2)^(1/2))+1)                 =
counterSIM(round(((kx-PeakPosition_x)^2+(ky-PeakPosition_y)^2)^(1/2))+1) + 0;
            elseif ((kx-678)^2+(ky-513)^2)^(0.5)<25;
```

```
                RISIMImage1(round(((kx-PeakPosition_x)^2+(ky-PeakPosition_y)^2)^(1/2))+1)                =
RISIMImage1(round(((kx-PeakPosition_x)^2+(ky-PeakPosition_y)^2)^(1/2))+1) + 0;
                counterSIM(round(((kx-PeakPosition_x)^2+(ky-PeakPosition_y)^2)^(1/2))+1)                =
counterSIM(round(((kx-PeakPosition_x)^2+(ky-PeakPosition_y)^2)^(1/2))+1) + 0;
                %elseif ((kx-379)^2+(ky-511)^2)^(0.5)<10;
                %RISIMImage1(round(((kx-PeakPosition_x)^2+(ky-PeakPosition_y)^2)^(1/2))+1)                =
RISIMImage1(round(((kx-PeakPosition_x)^2+(ky-PeakPosition_y)^2)^(1/2))+1) + 0;
                %counterSIM(round(((kx-PeakPosition_x)^2+(ky-PeakPosition_y)^2)^(1/2))+1)                =
counterSIM(round(((kx-PeakPosition_x)^2+(ky-PeakPosition_y)^2)^(1/2))+1) + 0;
                %elseif ((kx-647)^2+(ky-515)^2)^(0.5)<10;
                %RISIMImage1(round(((kx-PeakPosition_x)^2+(ky-PeakPosition_y)^2)^(1/2))+1)                =
RISIMImage1(round(((kx-PeakPosition_x)^2+(ky-PeakPosition_y)^2)^(1/2))+1) + 0;
                %counterSIM(round(((kx-PeakPosition_x)^2+(ky-PeakPosition_y)^2)^(1/2))+1)                =
counterSIM(round(((kx-PeakPosition_x)^2+(ky-PeakPosition_y)^2)^(1/2))+1) + 0;
                else
                RISIMImage1(round(((kx-PeakPosition_x)^2+(ky-PeakPosition_y)^2)^(1/2))+1)                =
RISIMImage1(round(((kx-PeakPosition_x)^2+(ky-PeakPosition_y)^2)^(1/2))+1) + SIMImage3(kx,ky);
                counterSIM(round(((kx-PeakPosition_x)^2+(ky-PeakPosition_y)^2)^(1/2))+1)                =
counterSIM(round(((kx-PeakPosition_x)^2+(ky-PeakPosition_y)^2)^(1/2))+1) + 1;
                end
            end
        end
        RISIMImage1=RISIMImage1./counterSIM;
        mean(RISIMImage1(:,600:760));
        RISIMImage1=RISIMImage1-ans;
        normRISIMImage1=RISIMImage1/RISIMImage1(1)*normRISIMBase(1);
        normRISIMImage=normRISIMImage+normRISIMImage1;
        subRISIMImage1=normRISIMImage1-RIImage;
        subRISIMImage=subRISIMImage+subRISIMImage1;
        RI1=subRISIMImage1-subRISIMBase;
        eval(['RI_',num2str(SIMImageii),'=RI1;']); %各画像での Image での割り算を構造化照明のスポット周りに積
算したもの
        RI=RI+RI1;
        SRI(:,SIMImageii)=RI1;
end
SIMImage=SIMImage1;
```

```
FFTSIMImage=FFTSIMImage/Num;
normRISIMImage=normRISIMImage/Num;
subRISIMImage=subRISIMImage/Num;
RI=RI/Num;

%%
figure(1);
subplot(2,2,1); imagesc(Base); axis image; colormap gray;
axis([ImageCenterY-255,ImageCenterY+256,ImageCenterX-255,ImageCenterX+256]);
subplot(2,2,2); imagesc(Image); axis image; colormap gray;
axis([ImageCenterY-255,ImageCenterY+256,ImageCenterX-255,ImageCenterX+256]);
subplot(2,2,3); imagesc(SIMBase); axis image; colormap gray;
axis([ImageCenterY-255,ImageCenterY+256,ImageCenterX-255,ImageCenterX+256]);
subplot(2,2,4); imagesc(SIMImage); axis image; colormap gray;
axis([ImageCenterY-255,ImageCenterY+256,ImageCenterX-255,ImageCenterX+256]);
%pause(3);
figure(2);
subplot(2,2,1); imagesc(FFTBase); axis image;
subplot(2,2,2); imagesc(FFTImage); axis image;
subplot(2,2,3); imagesc(FFTSIMBase); axis image;
subplot(2,2,4); imagesc(FFTSIMImage); axis image;
%pause(3);
figure(3); hold off;
plot(SFRISIM,RIBase, 'k', 'LineWidth',2);hold on;
plot(SFRISIM,RIImage, 'b', 'LineWidth',2);
plot(SFRISIM,normRISIMBase, 'g', 'LineWidth',2);
plot(SFRISIM,normRISIMImage, 'r', 'LineWidth',2);
axis([0, 700, -0.01, 1]);
grid on;
hold off;
%pause(3);
figure(4); hold off;
plot(SFRISIM,subRISIMBase, 'b', 'LineWidth',2);hold on;
plot(SFRISIM,subRISIMImage, 'r', 'LineWidth',2);
axis([0, 700, -0.01, 0.1]);
grid on;
```

```
hold off;
figure(5);
plot(SFRISIM,RI, 'r', 'LineWidth',2);
axis([0, 700, -0.01, 0.1]);
grid on;

%% Igor にデータを移すための行列作成
IgorOutput=[SFRISIM.',RIBase.',RIImage.',normRISIMBase.',normRISIMImage.',subRISIMBase.',subRISIMImage.',RI.',S
RI];
IgorOutput=IgorOutput(1:NumRISIM-DataCutNum,:);
imwrite(Mask,'F:¥matlab file¥image¥data¥Mask.tif');
imwrite(uint8(round((Base-min(Base(:)))./(max(Base(:))-min(Base(:)))*256)),'F:¥matlab file¥image¥data¥Base.tif');
imwrite(uint8(round((Image-min(Image(:)))./(max(Image(:))-min(Image(:)))*256)),'F:¥matlab
file¥image¥data¥Image.tif');
imwrite(uint8(round((SIMBase-min(SIMBase(:)))./(max(SIMBase(:))-min(SIMBase(:)))*256)),'F:¥matlab
file¥image¥data¥SIMBase.tif');
imwrite(uint8(round((SIMImage-min(SIMImage(:)))./(max(SIMImage(:))-min(SIMImage(:)))*256)),'F:¥matlab
file¥image¥data¥SIMImage.tif');
imwrite(uint8(round((FFTBase-min(FFTBase(:)))./(max(FFTBase(:))-min(FFTBase(:)))*256)),'F:¥matlab
file¥image¥data¥FFTBase.tif');
imwrite(uint8(round((FFTImage-min(FFTImage(:)))./(max(FFTImage(:))-min(FFTImage(:)))*256)),'F:¥matlab
file¥image¥data¥FFTImage.tif');
imwrite(uint8(round((FFTSIMBase-min(FFTSIMBase(:)))./(max(FFTSIMBase(:))-min(FFTSIMBase(:)))*256)),'F:¥matlab
file¥image¥data¥FFTSIMBase.tif');
imwrite(uint8(round((FFTSIMImage-min(FFTSIMImage(:)))./(max(FFTSIMImage(:))-min(FFTSIMImage(:)))*256)),'F:¥
matlab file¥image¥data¥FFTSIMImage.tif');
dlmwrite('F:¥matlab file¥image¥data¥IgorOutput.asc',IgorOutput);
% End of file
```